الجمهورية الجزائرية الديمقراطية الشعبية

People's Democratic Republic of Algeria

Ministry of Higher Education and Scientific Research

Université Ferhat ABBAS Sétif 1

FERHAT ABBAS UNIVERSITY SETIF 1

FACULTY OF TECHNOLOGY

THESIS

Presented to the Process Engineering Department

For obtaining the diploma of:

DOCTORATE

Domain: Science and Technology

Field: Process Engineering **Option:** Polymer Engineering

By

ZERGUINE Narimene

THEME

Study of functionalization approaches for graphene oxide: towards the development of composite nanofibers for triboelectric energy harvesting

Defended on 17/12/2025, In front of the jury:

BENANIBA Mohamed Tahar	**Professor**	**Ferhat Abbas University Setif 1**	**President**
BOUHELAL Said	**Professor**	**Ferhat Abbas University Setif 1**	**Supervisor**
DAHOUN Abdesselam	**Professor**	**Ecole des Mines de Nancy**	**Co-supervisor**
DOUFNOUNE Rachida	**Professor**	**Ferhat Abbas University Setif 1**	**Examinator**
HAMMA Amel	**M.C.A**	**Med El Bachir El Ibrahimi University BBA**	**Examinator**
HELLATI Abdelhak	**Professor**	**Med El Bachir El Ibrahimi University BBA**	**Examinator**

ACKNOWLEDGEMENTS

My first and last gratitude go to the almighty ALLAH, for giving me the courage, health, guidance, knowledge and granting me His support during the most difficult times.

My second gratitude go to my parents for their unwavering encouragement, love, and understanding during this journey. Their constant support has been a source of motivation and strength.
Especially to my dear father, since I was a little girl, he talked to me about science, his invents and showed me fun experiments, which made me curious and excited to learn more. He truly inspired me with a dream that stayed with me my whole life. He was the first to show me the wonder of discovery, and it is because of his inspiration and belief in me that I walk this path today. This journey began with you Dad, and for that, I am forever grateful.

The work presented in this thesis was carried out within the Emerging Materials Research Unit (U.R.M.E), at Ferhat ABBAS University, Sétif-1 and Polymer laboratory at Bursa Technical University (Turkey).

I would like to express my deepest gratitude to Professor Said BOUHELAL, my research supervisor, for his unwavering support, and constant encouragement thru the course of this thesis. His insightful advice, exceptional patience, and generous availability have been instrumental in shaping both the direction and quality of this work. I am especially thankful for his ability to challenge me to grow academically.

I would like to sincerely thank Pr. Abdesselam DAHOUN for accepting to co-supervise this thesis.

My deepest gratitude goes to Pr. Yasin ALTIN, whose warm reception, encouragement, and mentorship made my academic journey at Bursa Technical University both welcoming and enriching. His invaluable suggestion of an alternative approach was pivotal in saving my thesis. His mentorship, his insight and expertise were instrumental in guiding me toward a successful resolution, from insightful discussions to practical assistance were powerful in overcoming advancing the quality of this work. I cannot thank him enough for their timely advice and support.

Special thanks to Dr. Ömer Faruk Ünsal for working closely with me during this research. his guidance, technical expertise, and consistent support were crucial; from offering valuable insights to providing hands-on help thru critical phases, his contribution has been deeply appreciated.

I would also like to thank Dr. İnal Kaan Duygun for being with me through this journey. His encouragement, readiness to help at every stage and his unwavering support lightened the difficult moments and brought greater joy to the achievements, his contribution has been truly invaluable.

I also want to thank Pr. Kenan Yildirim and Pr. Ayşe Çelik Bedeloğlu for their warm reception and support during my time at Bursa Technical University.

I would like to convey my sincere thanks to all the staff of Bursa Technical University for their kindness, assistance, and dedication, which created a supportive and welcoming academic environment.

I would like to particularly thank all the members of the jury for the honor of evaluating my work. I express my deepest respect and gratitude to each of you, as well as to all the professors who have educated us since the first year.

I extend my thanks to all the members of the Emerging Materials Research Unit; engineers, and technicians for their kindness, commitment and availability during the various phases of this work.

Lastly, I am deeply grateful to my colleague researchers and dear friends: Dr. Nasri Yasmine, Dr. REGUIG Abdelbasset, Dr. REMILA Ibrahim and Dr. BENSALLEM Ilyes whose support, insight, and companionship were invaluable thru this journey. Their encouragement and collaboration made the challenges more manageable and the successes more meaningful.

A big thank you to all those mentioned for standing by me every step of the way.

DEDICATIONS

To my parents who supported me during my studies and never deprived me of their attention, encouragement, and especially their love, their prayers and blessings have been of great help in successfully completing my studies. No dedication could ever be eloquent enough to express what you deserve for all the sacrifices you have continuously made for me since my birth. Nothing in the world is worth the efforts you have put in day and night for my education and well-being. This work is the fruit of your sacrifices that you have made for my education.

To you, Dad , to you, Mom, I dedicate this work.

To my brothers Baha Eddine, Alla Eddine, Azzedine, and my little sister Iness who have supported me.

To my grandmother and especially to my late grandfathers and grandmother, may Allah have mercy on them.

To my uncles and aunts.

To my cousins.

To all my friends and Family.

Finally, I dedicate this work to myself for the perseverance, the late nights and the quiet strength, that made this journey possible.

Narimene ZERGUINE

TABLE OF CONTENTS

Chapter II: Electrospun Nanofibers: From Fundamentals to Functional Applications

Chapter III: Advancements in Triboelectric Nanogenerators: Mechanisms, Materials, and Performance Enhancement

Chapter IV: Experimental Insights into Nanomaterials and Nanofibers Production

Chapter V: Results and Discussion

List of Figures

Chapter I

Chapter II

List of Figures

Chapter III

Chapter IV

List of Figures

Chapter V

List of Tables

Chapter IV

Chapter V

GENERAL INTRODUCTION

General introduction

Carbon-based nanomaterials, including diamond, amorphous carbon, carbon nanotubes (CNTs), and graphene (Gr), have emerged as a class of advanced materials distinguished by their outstanding physicochemical properties. These include high electrical and thermal conductivity, enormous mechanical strength, and distinctive optical characteristics. Owing to this unique combination of properties, their applicability has expanded into a wide range of fields, encompassing electronics, chemical and biological sensing, as well as energy conversion and storage systems [1].

Graphene oxide (GO) can be described as a chemically oxidized form of graphene. In recent years, it has drawn considerable attention within the scientific community, largely because of its combination of high surface area and notable mechanical robustness, which enable its use in a broad spectrum of technological applications [2,3]. Nevertheless, the hydroxyl, carboxyl, and epoxide functionalities distributed across the basal planes and sheet edges of GO are capable of forming extensive hydrogen-bonding networks between adjacent sheets thereby limiting the exfoliation of individual nanosheets and promoting their tendency to agglomerate [4,5]. Thus, to address the aggregation tendency of GO, several approaches have been proposed such as surface grafting, in situ polymerization and decorating with nanoparticles [6].

Organofunctional silanes are molecules that contain two distinct reactive groups bonded to a silicon atom, which allows them to react and bond with inorganic or organic material through covalent interactions [7]. These molecules are widely utilized to modify the surface chemistry of carbon-based nanomaterials, enabling the creation of nanomaterials with improved or entirely new physicochemical properties. The functionalization of GO with organosilanes has been widely investigated, with different silane precursors employed to tailor its surface chemistry. This modification is made possible by the abundance of oxygenated functional groups distributed across both the basal planes and sheet edges of GO, which act as reactive sites for covalent bonding [8]. This method significantly improves the interfacial interactions, facilitates the exfoliation of GO sheets, and enhances their compatibility with diverse matrices when incorporated as reinforcing agents [9–11].

Furthermore, decorating GO' surface with nanoparticles is also an efficient route. A wide range of nanoparticles, such as silica, aluminium oxide, zinc oxide, titanium oxide and zirconium oxide (ZrO_2) have been employed for this purpose [3,12]. Recently, ZrO_2 has gained considerable interest among scientists as a promising material for several structural applications due to their excellent hardness, mechanical strength, chemical and thermal stability [13,14]. The latter

represents highly attractive candidates for anchoring onto the surface of GO. Several investigations have highlighted that the incorporation of carbon-based nanomaterials, particularly GO, into ZrO_2 can induce a synergistic effect, leading to improved functional and structural properties [15–17].

Nanotechnology advancements have led to the invention of nanogenerators; devices capable of converting mechanical energy into electricity based on two effects piezoelectricity and triboelectricity. Since Wang and Song [18] introduced a zinc oxide-nanowire based piezoelectric nanogenerator in 2006, the field of energy harvesting has undergone a significant revolution. In 2012, Wang et al.[19] exploited a polymer-based triboelectric nanogenerator (TENG), based on the combined impact of triboelectrification and electrostatic induction; when two dissimilar materials come into contact and then separate, charge transfer will be occurred [20].

The efficiency of TENGs is strongly influenced by the selection of triboelectric materials, surface morphology, dielectric constant, and device configuration [20]. The tribocharging behavior of materials plays a critical role in the material selection process during the fabrication of TENGs. The performance of a TENG is directly proportional to the difference in tribocharge density between the tribopositive and tribonegative layers. Although early studies aimed to enhance TENG performance by carefully selecting material pairs with large triboelectric differences, the scope of such improvements is inherently limited by the finite availability of suitable materials with strong and opposing triboelectric properties. In response to this limitation, recent research has shifted toward strategies focused on modifying the micro- and nanostructures of tribo-surfaces and tuning their surface charge behaviors. These approaches, which include surface patterning and doping, have gained considerable attention as effective methods to further enhance the triboelectric output beyond what can be achieved by material selection alone. According to previous studies, the use of nanofibers in nanogenerators is a widely adopted technique to increase energy conversion efficiency and enhance the mechanical performance of energy-generating devices; due to their unique properties such as high surface area, tunable mechanical properties, and flexibility, that render them highly suitable for this purpose. There are various techniques for the fabrication of nanofibers, and among them, electrospinning, considered as a simple, versatile, cost-effective, and promising method to produce nanofibers with several specific characteristics. The cost-effective approach allows the combination of polymers, inorganic nanoparticles, metals, ceramics, active agents, and polymers to form multifunctional nanocomposites with additional properties [21].

As a kind of electrospinning material, polyacrylonitrile (PAN) is a popular choice because of good mechanical strength, chemical resistance and thermal stability, also it is widely used in

applications involving sensors and storage devices. Moreover, studies have shown that nanofibrous structures based on PAN can be advantageous for enhancing advanced triboelectric technology [22].

Indeed, doping nanomaterial additives into the contact layer can improve TENG performance by augmenting surface charge density and reducing triboelectric losses. These nanomaterials enhance the dielectric properties of the triboelectric material, thereby improving charge retention; for instance, carbon-based materials or inorganic fillers possessing a high dielectric constant or conductive filler (metal nanoparticles and inorganic nonmetallic materials).

GO has garnered considerable attention from researchers as a triboelectric material due to its capacity to gain electrons, attributed to the oxygen functional groups present on the basal planes and edges of the graphene sheet. The properties of GO, including extensive surface area, and robust charge effect, contribute to the superior performance of GO-based TENGs [23]. Huang et al.[24] developed a TENG based on electrospun polyvinylidene fluoride (PVDF) and poly(3-hydroxybutyrate-co-3-hydroxyvalerate) (PHBV) nanofibers doped with GO. The incorporation of GO sheets was aimed at enhancing the charge storage capability and thereby improving the overall output of the TENG. The well-dispersed GO nanosheets function as charge-trapping centers, providing additional interfacial sites for charge accumulation, which in turn contributes to the improved electrical performance of the device. A study headed by Yar et al.[25] revealed that the performance output voltage can be enhanced using inorganic doped organic materials; the flexible nanofibers PAN-boric acid as a triboelectric contact layer improved significantly the power production performance of PAN. A TENG based on poly (vinylidene fluoride-co-hexafluoropropene)-ZrO_2 nanocomposite was reported by Saikh et al.[26] which demonstrated remarkable output performance, generating 7 V from a simple finger touch. This promising approach offers a scalable solution for powering self-sustained systems by converting small mechanical energy from human activities into electrical energy.

To improve the output of TENGs, chemical modifications could be proposed as well to increase the charge density of friction materials. the amino group has an excellent electron-donating ability, and many studies have been published based on amino modifications. For instance, Zheng et al.[27] demonstrated in their study that enhancing the tribopositive polarity of the cellulose aerogel film through silanization with amino silane can significantly improve the triboelectric performance.

While numerous studies have explored strategies to enhance the performance of TENGs, such as incorporating GO, doping with metal oxide nanoparticles like ZrO_2, or functionalizing surfaces with organosilanes; the combined integration of these approaches within a single

nanofibrous system remains largely unexplored. In particular, the synergistic incorporation of amino-silanized GO decorated with ZrO_2 nanoparticles (SGO-ZrO_2) into electrospun PAN nanofibers has not been fully investigated. This study addresses that gap by developing PAN-based electrospun nanofibers embedded with SGO-ZrO_2, aiming to enhance charge generation and mechanical performance for high-output TENG applications.

This thesis begins with a general introduction and is structured into five chapters, two of which are dedicated exclusively to the experimental work and the results obtained.

The first chapter, presents a comprehensive overview of carbon allotropes, with a particular focus on GO, it outlines the fundamental aspects of GO chemistry and its functionalization strategies, highlighting their importance in expanding the potential of this material for advanced technological applications.

The second chapter, provides a structured introduction of nanofibers, emphasizing electrospinning as a key fabrication method, the factors affecting fiber morphology, strategies for creating nanocomposites, and their applications in energy and environmental fields.

The third chapter, covers triboelectric nanogenerators (TENGs), focusing on their operating principles, and strategies for enhancing performance through material selection, surface engineering, and nanoscale structuring to improve energy harvesting efficiency.

The fourth chapter, outlines the materials and experimental procedures, including the synthesis of GO and SGO-ZrO_2 nanohybrids, their incorporation into PAN matrix, and the fabrication of electrospun nanofibers. It also covers the characterization techniques used to assess the structural and functional properties of the materials.

The fifth chapter, is to present the results and discussion regarding the synthesized nanomaterials and the fabricated nanofibers.

Finally, the thesis concludes with a general conclusion.

Chapter I: Literature Review on Graphene Oxide: Synthesis, Functionalization, and Advanced Modifications

Chapter I: Literature Review on Graphene Oxide: Synthesis, Functionalization, and Advanced Modifications

Table of Content

Chapter I: Literature Review on Graphene Oxide: Synthesis, Functionalization, and Advanced Modifications

Chapter objective

This chapter provides a comprehensive overview on carbon allotropes, with a particular focus on GO, its synthesis, structural properties, and chemical reactivity. Special attention is given to the functionalization strategies of GO, including both covalent and non-covalent modifications, to enhance its performance for various applications. The modification of GO using silane coupling agents is explored as a method to improve interfacial properties, while its decoration with nanoparticles is discussed in the context of nanocomposites, catalysis, and other applications. By detailing these aspects, this chapter aims to provide a fundamental understanding of GO chemistry and its modifications, highlighting their role in expanding the potential of this material for advanced technological applications.

I.1 The evolution of Carbon: From Element to Allotropes

Carbon ranks as the fourth most abundant chemical element in the universe and is widely distributed on earth, it can be found in crust, atmosphere as well as all the living organisms. It is also the sixth element in the periodic table with C as symbol atomic structure, an atomic number of 6 and an electron configuration of $1s^2$ $2s^2$ $2p^2$. Carbon can mostly adapt three kinds of hybridization, called sp, sp^2 and sp^3. Its hybridization state and atomic arrangement can lead to various forms known as allotropes, such as graphite, diamond, fullerene, carbon nanotubes (CNTs) (Figure I.1) [28,29].

In the early 1980s, it was recognized that pure condensed carbon exists in two distinct crystalline forms: diamond and graphite. These forms illustrate the fascinated versatility of carbon ranging from the soft and malleable graphite used in pencils to the hard and brilliant diamonds that embellish valuable jewellery.

Diamond is naturally formed in the earth's mantle under a pressure of 5-6 GPa and temperatures ranging from 1300 to 2000 °C [28], it is a meta-stable allotrope of carbon; the formation of diamond involves the crystallization of liquid carbon through a very long process in which carbon exhibits four covalent bonds with adjacent carbon atoms each is 0.154 nm in length, these bands are arranged in tetrahedral symmetry through sp^3 hybridization, resulting in a three-dimensional crystalline structure (3D) [30].

Graphite is the most abundant natural and stable form of carbon which was discovered more than five centuries ago, with an annual production exceeds 10^6 tones, and as a result it is an inexpensive mineral. The unique physical and mechanical properties of graphite create many opportunities for this form of carbon to be used in a wide range of applications, such as refractories, batteries, lubricants, etc. The unique properties of graphite lie in its atomic

structure, with layers of honeycomb carbon atoms; on a layer plane (graphene) carbon atoms bond together with sp^2 hybridization generating π electrons with high mobility, each band is 0.142 nm in length. The carbon atoms in the basal plane bond covalently whereas the carbon layers in the perpendicular direction are held together by van der Waals interactions, leading to a two-dimensional crystalline structure (2D) [31,32].

In the mid-1980s, H. Kroto, et al.[33] discovered another allotrope of pure carbon. The newly discovered species is identified as the most renowned of the fullerene molecules: C_{60} fullerene; defined by a structure where each carbon atom bonds with three adjacent atoms, creating a network of hexagons combined with pentagons and heptagons, preventing the sheet from being flat and results in a shape similar to a hollow sphere. The new arrangement arises from an intermediate hybridization state between sp^2 and sp^3 that carbon atoms adopt, leading to a material characterized by zero dimensionality (0D). Indeed, the finding of carbon nanotubes was closely related to that of C_{60}. In 1991, S. Iijima et al.[34] identified rigid, elongated structures in the soot generated by electric arc discharge during the production of C_{60}. Electron microscopy examination revealed that these structures were "helical microtubules of graphitic carbon" consisting of 2 to 50 walls, with widths varying from 4 to 30 nm, ensuring the identification of multi-walled carbon nanotubes (MWCNTs) with one dimensional structure (1D). Two years later, in 1993, a group of researchers headed by D-S. Bethune established the possibility of synthesizing single-walled carbon nanotubes (SWCNTs).[35] Until this day the Graphene is the last carbon allotrope to be discovered, it represents the foundation of all other allotropes; a planar monolayer of carbon atoms arranged into a 2D honeycomb lattice with a carbon–carbon bond length of 0.142 nm, with the ability to be transformed into a spherical shape to create fullerenes or rolled into a tube to form carbon nanotubes. In fact, before 2004, Graphene was only theorized and had not been isolated physically. However, Novoselov's research group [36] marked a significant advancement in carbon research by achieving the first successful extraction of a single atomic plane through mechanical graphite exfoliation [37,38]. Numerous studies have established graphene as an extraordinary material due to its remarkable properties. It is incredibly lightweight, with a mass of only 0.77 $mg.m^{-2}$. It has a high intrinsic electrical conductivity, with a charge carrier mobility of up to 200,000 $cm^2.V^{-1}.s^{-1}$; higher than that of copper. Additionally, it has exceptional mechanical strength, with a Young's modulus of 1 TPa and a tensile strength of 130 GPa. In addition, due to its 2D structure, graphene has an impressive surface area of 2630 $m^2.g^{-1}$, which enhances its ability to store electrical energy in capacitors. This unique characteristic could enable batteries to recharge within minutes rather than hours [39,40].

These carbon-based nanomaterials (carbon allotropes) have emerged as highly promising materials owing to their their excellent chemical and physical properties, including high thermal and electrical conductivity, enormous mechanical and optical properties. As a result, their utilization has expanded across diverse fields, including electronics, biosensing and chemical sensing, as well as energy conversion and storage technologies. [1].

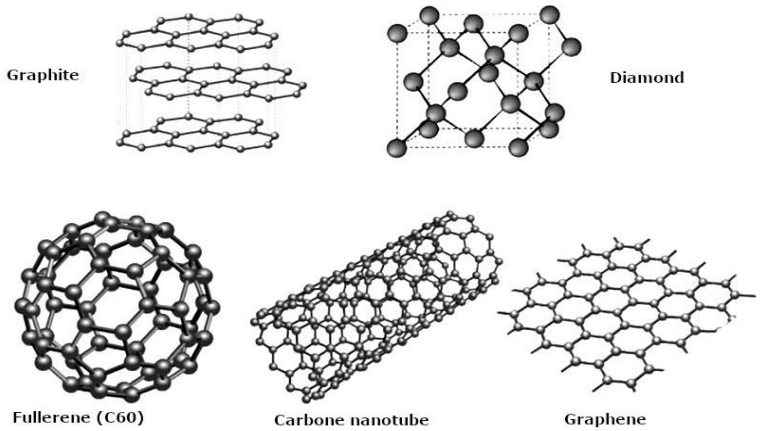

Figure I.1: carbon allotropes [41].

I.2 Graphene oxide (GO)

GO is widely studied across various fields such as materials science, chemistry, physics, biology, medicine, and nanotechnology. As a carbon-based nanostructure it has attracted significant interest as an innovative nanomaterial.

GO is considered as an oxidative state of graphene. Typically, it is a 2D material made of sp^2 and sp^3 hybridized carbon atoms arranged in a hexagonal honeycomb structure with variety of oxygenated functions (i.e. epoxides, alcohols and carboxylic acids) present on its surface (Figure I.2). It was discovered first in 1859 by Brodie [42], long before graphene, although its properties have only recently started to be fully exploited. Following Brodie's finding, Staudenmaier [43] and Hummers [44] developed additional methods for synthesizing GO [45]. All these methods involve oxidizing graphite to several level will be discussed as well in details in the next section.

Figure I.2: Structure of graphene oxide [46].

I.2.1 Main synthesis procedures of graphene oxide (GO)

GO is mainly synthesized through an oxidative process applied to graphite; the later made of carbon atoms arranged in a hexagonal honeycomb structure, where each atom is bonded to three adjacent atoms. It has a lamellar structure, with layers separated by a distance of 0.34 nm and interrelated with van der Walls interactions, enabling the intercalation of various ions and molecules [31] (Figure I.3).

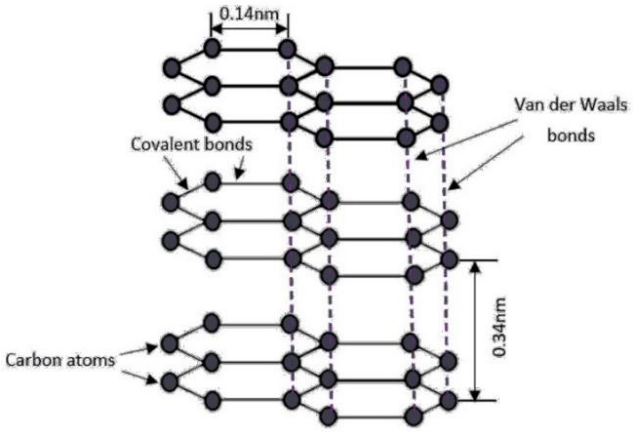

Figure I.3: Structure of graphite [47].

In 1898, British chemist B. C. Brodie [42] conducted the first study on the reactivity of graphite flakes by treating it with an oxidation mixture of potassium chlorate ($KClO_3$) and fuming nitric acid (HNO_3). Forty years later, Staudenmaier [43] proposed a variation of the original Brodie's method by employing concentrated sulfuric acid (H_2SO_4) and fuming nitric acid (HNO_3), while introducing potassium chlorate ($KClO_3$) in multiple aliquots throughout the reaction. The slight change proposed by Staudenmaier allowed to increase the C:O ratios until 2:1 meaning a major oxidation degree as previously described by Brodie. Subsequently, approximately sixty years later, Hummers and Offeman [44] introduced a novel method for the oxidation of graphite utilizing potassium permanganate ($KMnO_4$) and sodium nitrate ($NaNO_3$) in concentrated sulfuric acid (H_2SO_4), achieving a C:O ratio comparable to that obtained by Staudenmaier. This method involves also the utilization of a dilute solution of hydrogen peroxide (H_2O_2) to neutralize the excess of $KMnO_4$, leading to the formation of harmless manganese sulphate salts and oxygen gas which will be effectively eliminated in the purification process. All three procedures generate the toxic gases NO_2, N_2O_4, and/or ClO_2, the latter of which is also explosive.

Historically, Hummer's method has been the predominant method employed for the oxidation of graphite. In 2010, Mercano et al.[48] demonstrated that excluding $NaNO_3$, increasing the quantity of $KMnO_4$, and performing the reaction in a 9:1 mixture of H_2SO_4 and phosphoric acid (H_3PO_4) enhances the efficiency of the oxidation process. This method presents notable

advantages compared to the previous methods. The reaction protocol does not generate a significant exothermic response and does not emit toxic gases. Moreover, it has been shown that the elimination of $NaNO_3$ does not affect the yield of the overall reaction. This type of approaches is generally milder than the original Hummers' method and a careful control of the amount of water and the temperature of the reaction leads to layers with either hydroxyl and epoxide-rich or more carbonyl-rich domains [49].

It is evident that not only the different methods that already exist can produce important variation in the oxidation process. Additional parameters influencing the variety and density of functional groups during synthesis include: the nature of pristine graphite, its particle size, the oxidizing reagents employed, temperature of the reaction, and oxidation time. Minor alterations in those conditions may result in a broad range of functional group densities [50].

At this stage, the synthesized material is graphite oxide. It is crucial to differentiate GO from graphite oxide. Both are chemically analogous, yet they exhibit significant structural differences. GO consists of stacked layers, whereas it results from the exfoliation of graphite oxide into monolayers or multilayered stacks [51].

The exfoliation process can be achieved through various methods, with sonication of oxidized graphite in a solvent (water or organic solvents) being the most commonly used technique, Prades et al.[52] demonstrated that the prepared graphite oxide could be dispersed in N, N-dimethylformamide (DMF), N-methyl-2-pyrrolidone (NMP), tetrahydrofuran (THF), and ethylene glycol (EG). In all of these solvents, full exfoliation of the graphite oxide material into individual, single-layer GO sheets was accomplished by sonication.

Moreover, other exfoliation approaches are adopted to obtain GO sheets including the application of shear stress in a Couette–Taylor flow reactor [53] or homogenization employing a high-speed blade-impeller (blender), a magnetic Teflon stirrer or by gentle hand-shaking [54,55]. (Figure I.4 illustrates the three principal methods to exfoliate graphite oxide (sonication, mechanical forces and shearing stress).

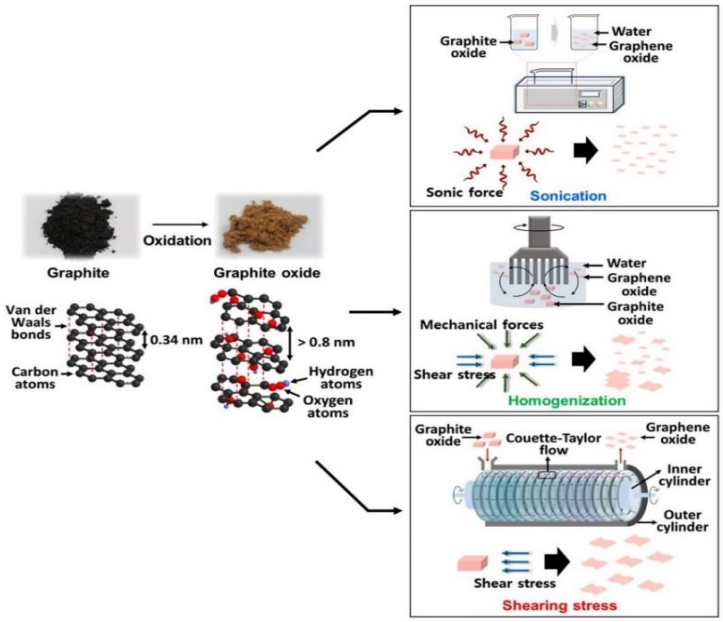

Figure I.4: Schematic of exfoliation methods of graphite oxide into GO (sonication, homogenization, and shearing stress) [53].

In addition to chemical methods, alternative approaches have been developed for the synthesis of GO. Among them, electrochemical synthesis presents a promising route, particularly for large-scale production. This method is considered more eco-friendly than conventional chemical processes, as it allows for the repeated use of electrolytes and requires minimal washing of equipment. Furthermore, electrochemically synthesized GO tends to exhibit superior quality compared to chemically produced GO. This can be attributed to the use of aqueous electrolytes and the absence of oxidizing agents, which helps prevent contamination by impurities. Additionally, the versatility of electrochemical setups enables precise control over the oxidation level and defect density [56].

I.2.2 Structure of graphene oxide (GO)

The structure of GO is highly variable and it depends on the conditions used for its synthesis. Currently, a precise molecular formula for GO remains elusive, despite significant research advancements. Various structures have been proposed concerning the variation of functional groups, the later were primarily identified in the form of hydroxyl and epoxy groups, with smaller quantities of carboxyl, carbonyl, phenol, lactone, and quinone.

The initial instructive model for the structure of GO was proposed in 1940 by Hofmann and Holst [57], suggesting that the distribution of hydroxyl (-OH) and epoxide (1,2-ether) groups were allocated on the basal plane parallel to the horizontal axis of the GO. Six years later, Ruess and Vogt [58] modified the Hoffman and Holst model. The improved structure consists of repetitive

units similar to cyclohexane, characterized by sp^3 hybridization. The model incorporated ethers at positions 1,3 on the cyclohexane, along with hydroxyl groups at position 4.

In 1969, Scholz and Boehm [59] introduced a model that entirely removed epoxy and ether (C-O-C) groups. This model assumes that ketone (C=O) functions and hydroxyl (-OH) groups are systematically incorporated into a wavy skeleton following the oxidation process. Indeed, research on the structure of GO continued uninterrupted; in 1994, Nakajima-Matsuo [60] proposed a model based on the covalent bond of the (C-C) with sp^3 hybridization, involving two layers of GO orientated perpendicularly to their surface. Consequently, the epoxy and ether functions have been substituted with hydroxyl groups that are distributed on the surface of GO. However, in 1998 Lerf and Klinowski [61] presented a model of GO that differs from previous models by integrating its amorphous and non-stoichiometric properties. The procedures implied reacting the original compound under different conditions to determine an appropriate structure; after several attempts, it was ultimately determined that the oxygenated functions are predominantly on the surface of GO sheets, manifesting as tertiary alcohols and ethers, while also identifying the existence of (C=C) double bonds. An improved model was subsequently proposed, by introducing carboxylic functions and ketones on the edges of GO to illuminate the structure.

In the first decade of the 21st century, the Dékàny et al.[62] introduced a new model in 2006 that represents a significant shift from previous ones while showing similarities to those proposed by Ruess and Scholz-Boehm. This model illustrates the existence of two distinct domains: trans-linked cyclohexane chairs and ribbons of flat hexagons with (C=C) double bonds and functional groups such as tertiary OH, 1,3-ether, ketone, quinone, and phenol (aromatic diol). Another study by Gao et al.[63] in which they demonstrated that the surface of GO contains ketone, lactol and tertiary alcohol functions in addition to epoxide and hydroxyl functions.

(the representation of the model in Figure I.4 “lactol groups (blue), esters (pink), hydroxyls (black), epoxides (red), and ketones (green)”).

Despite the various models proposed by researchers (Figure I.5), the exact structure of GO remains unclear to this day. Thereby several studies continue to unveil new insights into its composition [51,64].

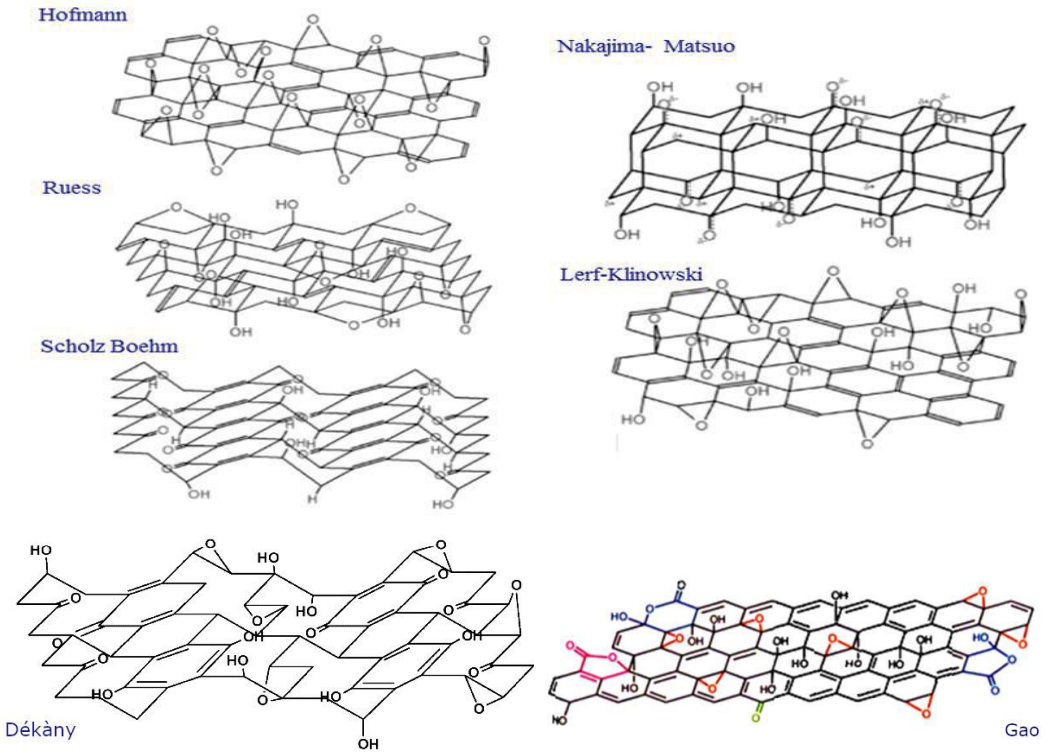

Figure I.5: Proposed structures of GO [57–63].

I.2.3 Properties of graphene oxide (GO)

As mentioned before the structure of GO consists of a repetitive arrangement of carbon atoms in a hexagonal configuration, incorporating both sp^2 and sp^3 hybridized carbon atoms with the presence of oxygen-containing functional groups on its surface and borders.

Generally, the conductivity of GO is a property that is relevant to the disturbance of the sp^2 bond network. The oxygenated functions induce structural defects, leading to the formation of holes between the valence band and conduction band, thereby converting the material into a semiconductor or insulator [65].

GO possesses additional properties, including amphiphilicity and a negative charge under physiological conditions. The material possesses a hydrophobic basal plane and hydrophilic edges, enhancing its solubility in various solvents [66]. It has also a very high specific surface area, which makes it attractive for applications in catalysis and various other fields. The Brunauer–Emmett–Teller (BET) method was employed to determine its large surface area. The calculated surface area for the GO is 890 $m^2 . g^{-1}$, whereas the experimentally determined surface area in aqueous solution is 736.6 $m^2 . g^{-1}$ [67].

The mechanical properties of GO have been investigated as well. A monolayer of GO exhibits a Young's modulus of 207.6 ± 23.4 GPa and a tensile strength of 76.8 ± 19.9 MPa [68].

I.3 Functionalization of graphene oxide (GO)

Surface functionalization is one of the most established and widely used techniques in materials science, enabling the introduction of functional groups onto material surfaces through chemical methods. Since each application demands specific chemical properties to achieve optimal performance, the functionalization of GO remains a crucial process and it is facilitated by the presence of various oxygen-containing functional groups on its surface. GO functionalization can be achieved through two main approaches: covalent and non-covalent modification [39].

I.3.1 Non covalent functionalization

The non-covalent functionalization of GO sheets mainly occurs through different weak interactions, it includes modifying the properties of GO while preserving its inherent structure. Among these interactions, Van der Waals forces or π-π stacking plays a crucial role in modifying GO with polymers or molecules containing an aromatic fraction. For example; Bouchareb et al.[69] demonstrated the successful formation of π-π interactions between the aromatic rings of the triphenylphosphine (PPh_3) molecule and those of the GO sheets. Beyond π-π interactions, the presence of oxygenated functional groups on the GO sheets, such as hydroxyl, carboxyl, and epoxide, favors the formation of hydrogen bonds with polar groups of other molecules or polymers. Zhao et al.[70] modified GO through a hydrogen-bonding interaction with diethyl-N,N-bis(2-hydroxyethyl) phosphoramide (DEPA), in addition, these functional groups facilitate the adsorption of positively charged molecules onto the surface of GO via electrostatic interactions, Lv et al.[71] functionalized GO with two-component organic gelator 1-OA (tetrazolyl derivative (1) and octadecylamine (OA)) via multiple non-covalent interactions including π-π stacking, hydrophobic interaction, hydrogen-bonds, van der Waals forces and electrostatic interactions (Figure I.6).

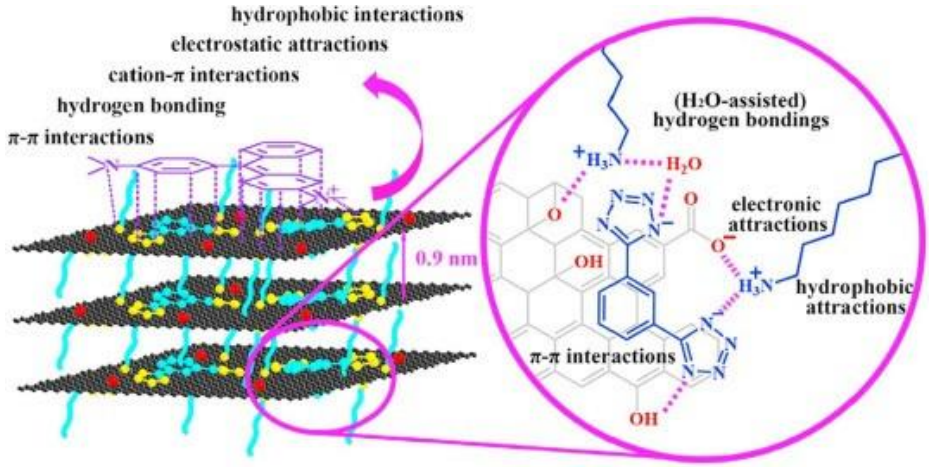

Figure I.6: Illustration of the non-covalent interactions between GO and 1-OA [71].

I.3.2 Covalent functionalization

Covalent functionalization involves the formation of covalent bonds between molecules, polymers, and the functional groups present on the GO surface. This modification enhances both the physical and chemical properties of GO, improving its solubility, catalytic activity, and introducing new functionalities to the material. It relies on well-established organic reactions, including nucleophilic and electrophilic substitutions, condensation reactions, and others. Moreover, covalent functionalization can induce the re-hybridization of carbon atoms from sp^3 to sp^2, partially restoring the electrical conductivity of graphite [39].

I.3.2.1 Reactions at the edges

Edge groups of GO, particularly carbonyl and carboxyl groups (COOH), serve as reactive sites for functionalization. Most chemical functionalization approaches use protocols suitable for reactions with carboxyl groups that are first activated and subsequently converted to esters or amides.

Amidation reactions, for example, enable the modification of GO's carboxyl groups with amines via nucleophilic acyl substitution, forming stable amide bonds (Figure I.7). However, the carboxylic groups must be activated by active reagents such as carbodiimides or thionyl chloride ($SOCl_2$). Notably, the amidation of GO with octadecylamine enhances its dispersion in tetrahydrofuran (THF), carbon tetrachloride, and 1,2-dichloroethane.

The formation of the ester bond, which is similar to the amidation process, results from the chemical reaction between hydroxyl groups (OH) and carboxyl groups (COOH). For instance, a study by Yu et al.[72] demonstrated that the -COOH group on GO, activated by thionyl chloride, well formed an ester bond with poly(3-hexylthiophene) terminated by CH_2-OH.[73]

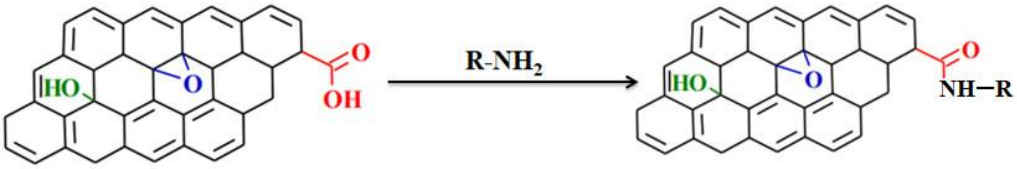

Figure I.7: Functionalization of GO via amidation reaction [73].

I.3.2.2 Reactions Mainly at the Basal Plane

On the basal plane, the functional groups present are hydroxyl groups and epoxy groups. However, hydroxyls are found with a higher concentration than epoxide groups, as they can be situated on both sides of the GO layers, with two hydroxyls for every epoxide group.

Organic compounds containing an isocyanate group (−N=C=O) are reactive with various nucleophiles (R−OH), resulting in the formation of the urethane (ROC(O)N(H)R′) linkage. The

isocyanate esterification serves as an effective approach for the removal of hydroxyl groups on GO. Stankovich et al.[74] suggested that the isocyanate treatment results in the functionalization of the carboxyl and hydroxyl groups in GO via formation of amides and carbamate esters, respectively. The formation of carbamate esters removes the surface hydroxyls and carboxyl groups at the edges that engage in hydrogen bonding (Figure I.8).

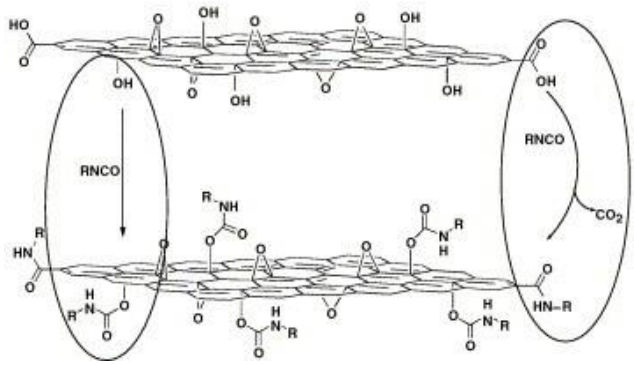

Figure I.8: Proposed reactions during the isocyanate treatment of GO where organic isocyanates react with the hydroxyl (left oval) and carboxyl groups (right oval) of GO sheets to form carbamate and amide functionalities, respectively [74].

On the other hand, epoxy groups are susceptible to be attacked by nucleophiles at the α-carbon by amine through ring opening reactions. The formed linkage may manifest as either an amide or ester bond, depending on the nucleophilic reagent (R−NH_2 or R−OH, respectively) (Figure I.9). For example, poly(allylamine) with a large number of reactive amine groups can react with epoxy groups of the GO sheets through ring-opening reaction, resulting in the formation of amide bonds. Meanwhile, poly (vinyl alcohol) can be grafted onto GO via ester bond.

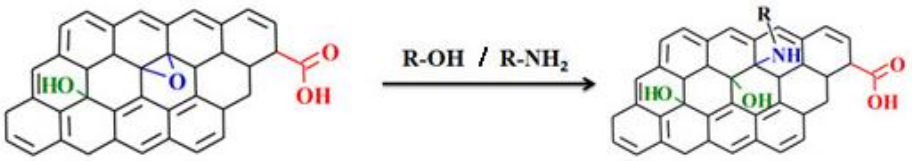

Figure I.9: Functionalization of GO via ring opening reaction [73].

Nevertheless, the amidation process cannot be excluded due to the presence of carboxylic groups and may occur concurrently with the epoxy ring-opening reaction under suitable conditions. This is a positive note for the fabrication of more stable graphene-based hybrids by utilizing more reactive sites, specifically epoxy and carboxylic groups. It has long been hypothesized that the amidation of edge −COOH groups may not adequately provide all the side chains necessary for the dispersibility of large sheets [75].Therefore, the parallel amidation

and epoxy ring opening reactions can be beneficial for the mechanical reinforcement of GO when cross-linked by providing more linkage points [76].

In addition to the functional groups on the basal plane, the −C=C sites on the basal plane of the graphene are susceptible to attacks by free radicals or dienophile species.

Diazonium salts ($R-N^{2+}2X^{-}$) represent the most widely used method in azo coupling, where the diazonium compound is reacted or coupled with electron-rich substrates, typically through electrophilic aromatic substitution. Heating diazonium salt, generates highly reactive radicals that interact with sp^2-hybridized carbon atoms to form covalent bonds. This reaction has been widely applied to functionalize sp^2-hybridized carbon materials, such as carbon nanotubes as well as graphene [73].

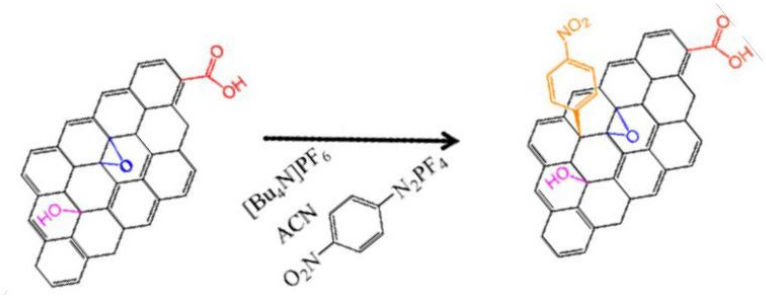

Figure I.10: Functionalization of GO via diazotization [73].

I.4 Silane coupling agent

Silanes refer to monomeric silicon compounds. A silane that contains at least one silicone carbon bond (Si-CH_3) is an organosilane, which is a functional organic compound carrying two different types of reactive groups attached to the silicon atom and characterized by the general formula $R_nSiX_{(4-n)}$ (n= 0, 1, 2, 3) where X represents a hydrolysable group (alkoxy, halide, or carboxylate) and R refers to a non-hydrolysable short-chain organic group. The reactive groups can react and link to an inorganic surface (e.g., ceramics and oxide layers on metals) or to organic resins via covalent bonds. This dual reactivity enables organosilanes to act as molecular bridges in a variety of applications including coatings, composites, and biological materials, thereby allowing adhesion, surface modification, and functionalization.

I.4.1 Key reactions of silane coupling agents

The reaction of organosilanes generally proceeds through four key steps (Figure I.11):

- Hydrolysis: The three hydrolysable groups (such as methoxy or ethoxy) react with water, producing silanol (-SiOH) species. This step is influenced by factors such as pH, solvent composition, and temperature, all of which affect the rate and extent of hydrolysis.

- Condensation: The silanol groups subsequently undergo condensation, forming siloxane (-Si-O-Si-) oligomers. The extent of condensation influences the stability and reactivity of the silane solution, ultimately affecting the thickness and uniformity of the final coating.
- Adsorption and Hydrogen Bonding: The resulting oligomeric silanol species then interact with hydroxyl (-OH) groups present on the substrate, forming hydrogen bonds. This step is crucial in ensuring strong adhesion before the formation of covalent linkages. The degree of hydrogen bonding depends on the density and availability of hydroxyl groups on the substrate, which varies depending on the material (e.g., glass, silica, graphene oxide).
- Covalent Bond Formation: During drying or curing, the hydrogen-bonded silanol groups react further, forming stable Si–O–substrate covalent bonds with the surface, accompanied by the release of water molecules. The efficiency and durability of this process are strongly influenced by curing conditions such as temperature and humidity.

Although these stages are often described in sequence, they frequently occur simultaneously after hydrolysis. At the interface, each silicon atom typically forms a single covalent bond with the substrate, while any remaining silanol groups may either remain free or undergo further condensation. Meanwhile, the organic R group remains available for additional functionalization, allowing further covalent modifications or physical interactions with other phases [77,78].

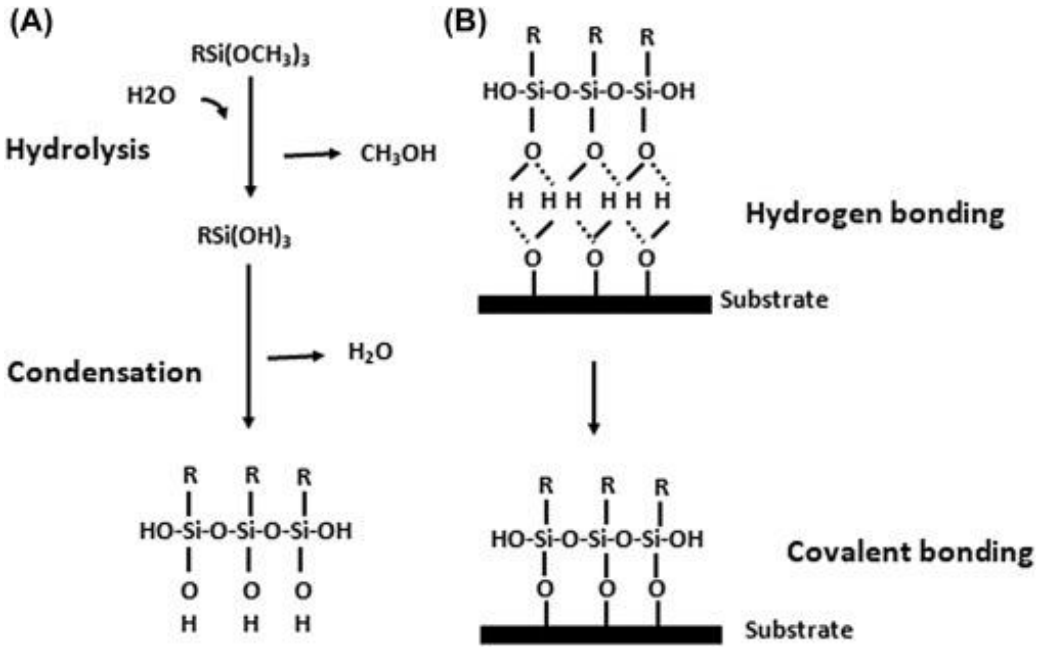

Figure I.11: Schematic illustration of the reaction mechanism of silane [78].

I.4.2 Surface modification of graphene oxide (GO) with organosilanes

Organosilanes are widely employed as surface modifiers for carbon-based nanomaterials, as they enable to create nanomaterials with novel chemical and physical properties. GO in particular, has been frequently functionalized with various silane precursors by multiple research groups, as its abundant oxygenated groups located on both the basal planes and sheet edges provide accessible reactive sites for covalent bonding [8]. In this context, silanization not only enhances the chemical versatility of GO but also improves its interfacial interactions, promotes better exfoliation, and increases compatibility with various matrices when employed as a reinforcing agent. Yang et al.[9] prepared modified graphene via facile covalent functionalization of GO with 3-aminopropyltriethoxysilane (APTES) and employed it as reinforcing agent in silica monoliths. Pourhashem et al.[10] demonstrated that the corrosion prevention performance of GO in polymer coatings may be effectively enhanced by modifying GO nanosheets using APTES and 3-glysidyloxypropyl trimethoxysilane (GPTMS), this was also proved in a study by Zhang et al.[27] in which they functionalized GO with 3-methacryloxypropyltrimethoxysilane (MPS) and subsequently dispersed it within a urushiol-formaldehyde polymer matrix (UFP), leading to a significant improvement in the anti-corrosion performance of the UFP coatings. Another research study by Dun et al.[11] reported that the anticorrosion properties of aluminium alloy were enhanced through the use of GO functionalized with GPTMS.

The surface treatment of GO by silane was employed as well to reinforce polymers; Lotfi et al.[79] modified the surface of GO by APTES (Figure I.12) and then incorporated it into an epoxy matrix. The results showed a considerable enhancement in the mechanical properties.

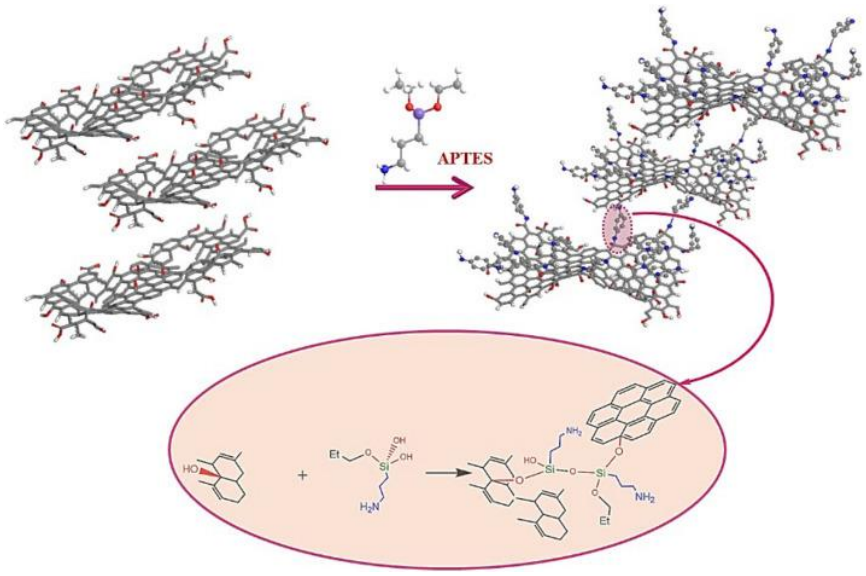

Figure I.12: Schematic of silane functionalized GO [80].

I.5 Nanohybrids based on graphene oxide (GO) and nanoparticles

I.5.1 Definition of hybrid materials

The term "hybrid material" has been used to refer to various systems that incorporate a range of different materials.

Yamamoto et al.[81] define hybrid materials as combinations of two or more materials that exhibit novel properties due to the formation of new electronic orbitals between each material. However, Makishima [82] describes hybrid materials as mixtures of two or more materials characterized by newly established chemical bonds. The categorization of hybrid materials is proposed as follows:

- Hybrids refer to a submicron-level mixture of various types of materials.
- Nanohybrids are atomic or molecular combination of different materials with chemical bonds between their different materials.

Another definition for hybrid materials proposed by Gómez-Romero and Sanchez [83], they described hybrid materials as systems in which both organic and inorganic species coexist. The hybrid nature of these materials confers properties that are intermediate between mineral and organic, as well as introducing new behaviors.

Niizeki [84] also describes hybrid materials as involving two or more types of chemical bonds created by "hybridizing" two or more monolithic materials, and consequently, hybrid materials have superior performance and/or new functions [85].

I.5.2 Decoration the surface of graphene oxide (GO) with metal oxide nanoparticles

Nanoparticles can be defined as primary particles with a small diameter less than 100 nm. The most prevalent nanoparticles presently employed are composed of transition metals, silicon, and metal oxides [86].

Metal oxide nanoparticles have gained significant attention among nanoparticles due to their distinctive physical and chemical properties. These nanoparticles can be composed of various materials, including zinc oxide (ZnO), titanium dioxide (TiO_2), copper oxide (CuO), zirconium oxide (ZrO_2), aluminium oxide (Al_2O_3), silicon dioxide (SiO_2), iron oxide (Fe_3O_4), magnesium oxide (MgO), nickel oxide (NiO), and manganese dioxide (MnO_2). Due to their distinct characteristics, metal oxide nanoparticles are commonly used as nanofillers in polymeric nanocomposites to enhance electrical, mechanical, and optical properties, as well as in metallic nanocomposites [87].

The GO has been used as an anchoring platform for nanoparticles. Decorating its surface with nanoparticles synergistically enhances its properties, making it highly versatile for applications

in energy storage, catalysis, electronics, biomedicine, and nanocomposites [88]. Like in a study by Liu et al.[12], in which they prepared epoxy-based nanocomposites by decorating the surface of GO with TiO_2 nanoparticles to enhance the anti-corrosion properties of the epoxy coating. In another study conducted by Sahoo et al.[89] GO-Fe_3O_4 nanohybrids were successfully synthetized using silane as a coupling agent, demonstrating its efficacy as an adsorbent for removal of hexavalent Chromium.

ZrO_2 is a bio-inert and nonresorbable metal oxide that has attracted significant research attention owing to its remarkable properties, including high hardness, superior mechanical strength, outstanding chemical and thermal stability [13,14], it has shown quantifiable success in all the forms; monoclinic, tetragonal, and cubic phases. Furthermore, ZrO_2 nanoparticles are regarded as highly promising for anchoring onto the surface of GO. Previous research has reported that the combination of ZrO_2 with carbon-based nanomaterials like GO generates synergistic effects on various properties, for instance, positive impacts on photocatalytic activity, chemical stability, and mechanical performance [90,91]. These nanohybrids can be synthesized using diverse techniques. A hydrothermal approach was used by Smirnov et al. [92] to create GO-ZrO_2. Another research group, headed by Teymourian et al. [15] have also reported on the same synthesis technique and its application as a new architecture for electrochemical sensing and biosensing purposes. Di et al.[16] have synthesized GO–ZrO_2 nanohybrids using two dissimilar silane-coupling agents, GPTMS and APTMS. These nanohybrids were subsequently incorporated into an epoxy matrix and has enhanced its corrosion prevention properties (Figure I.13). Toorchi et al.[17] have produced the nanohybrids GO-ZrO_2 by modifying both ZrO_2 and GO with the APTMS; the results showed that the introduction of these nanohybrids into the matrix of basalt fiber-reinforced epoxy composites has improved their energy absorption.

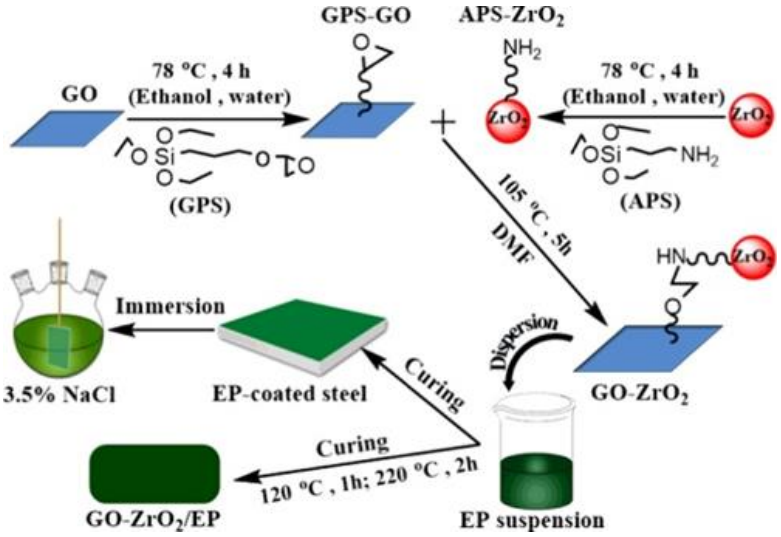

Figure I.13: Schematic of preparation of GO–ZrO_2 and the corresponding hybrid coatings [16].

Chapter II: Electrospun Nanofibers: From Fundamentals to Functional Applications

Chapter II: Electrospun Nanofibers: From Fundamentals to Functional Applications

Table of content

Chapter II: Electrospun Nanofibers: From Fundamentals to Functional Applications

Chapter objective

This chapter aims to provide a clear and structured overview of nanofibers, beginning with their definition and unique characteristics. It focuses on the electrospinning process as a versatile and widely used technique for their fabrication, detailing the fundamental principles and the influence of various processing parameters on fiber morphology. In addition, the chapter outlines the main approaches for fabricating electrospun nanocomposite fibers, emphasizing their structural and functional enhancements. Finally, it highlights the integration of electrospun nanofibers in advanced applications across fields such as energy and environmental science.

II.1 Definition of nanofibers

Nanofibers are fibrous structures with diameters typically ranging from a few nanometers to several hundred nanometers. Unlike traditional microfibers, they exhibit a high surface area-to-volume ratio, tunable porosity, and enhanced mechanical properties. Nanofibers can be synthesized from diverse materials, including polymers, ceramics, metals, and carbon-based compounds, owing to their distinct remarkable properties. They have been extensively utilized in various domains including filtration, biomedicine, energy storage, sensors, and advanced functional materials.

Various techniques are used in the production of nanofibers such as electrospinning, phase separation, self-assembly, and template synthesis. Among these, electrospinning is considered the most prominent method for producing polymer nanofibers. This relatively simple and scalable process enables the fabrication of long, continuous nanofibers with controlled alignment and morphology. Moreover, electrospinning allows for the processing of a wide range of polymers. the next section will focus on detailing the electrospinning process, including its fundamental principles, key parameters, and its role in nanofiber fabrication.

II.2 The electrospinning process

II.2.1 A brief history

Electrospinning is an efficient method for producing extremely thin fibers from various materials, such as polymers, ceramics, and composites. While the term "electrospinning," originating from "electrostatic spinning," has been in use since 1994, the fundamental principles of the process have been around for much longer nearly a century.

The story of electrospinning began in 1934, when Anton Formhals [93] introduced a significant patent detailing the process of electrospinning plastics. Between 1934 and 1944, Formhals

submitted a series of patents detailing the experimental setup for the creation of polymer filaments through the application of electrostatic force [94]. A cellulose acetate solution was subjected to an electric field to prepare polymer filaments, where one electrode was immersed in the solution, while the second electrode was positioned on a collector. The charged solution jets were ejected from a metal spinneret with a small orifice and subsequently evaporated to form fibers, which were collected at the electrically grounded collector. Decades later, in 1971, Baumgarten [95] developed a device for electrospinning acrylic fibers with diameters between 0.05 and 1.1 microns [96]. In this procedure, a stainless-steel capillary tube was utilized to suspend a droplet polymer solution, and feed rate was controlled by infusion pump while maintaining constant droplet size. The capillary tube was connected to a high-voltage DC current, fibers were collected at a specific distance on a grounded metal screen. However, this innovation, which was followed by an additional 12 patents, went mostly unrecognized.

The electrospinning procedure, essentially like that described by Baumgarten, has got more attention since the 1990s, notably in recent years. Ultrafine fibers or fibrous structures of different polymers can be created in the laboratory with a setup and have potential for industrial scale application.

II.2.2 Electrospinning process

The polymer solution used in the electrospinning process must possess the ability to carry a charge and exhibit adequate viscosity to elongate without fragmenting into droplets [97]. Three primary requirements are necessary to execute the procedure: a high voltage supply, a capillary tube with a small needle, and a grounded gathering screen. The initial step in the processing stage involves filling the capillary tube with a polymer solution. Sometimes, the use of solvents may result in the release of noxious odors from the polymer. Therefore, sufficient ventilation is necessary for conducting electrospinning within a chamber. High voltage, typically ranging from 1 to 30 kV, is utilized to suspend droplets of the polymer solution, thereby electrifying the liquid surface. This results in the droplet deforming into a conical structure referred to as a Taylor cone. The charged jet of solution is ejected from the tip of the Taylor cone when the electric voltage reaches a critical threshold, as the electrostatic force surpasses the surface tension of the droplets. As the jet moves toward a collector, solvents either solidify or evaporate in under one-tenth of a second, resulting in the collection of fine fibers into a web structure (Figure II.1) [96].

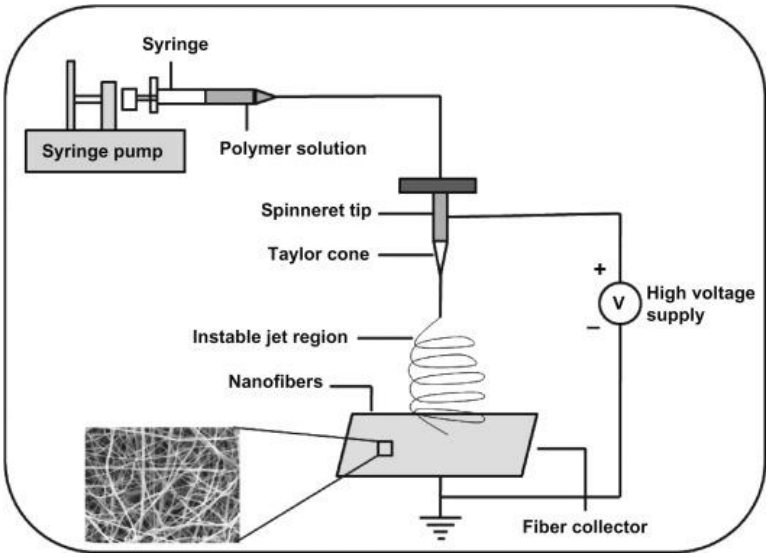

Figure II.1: Schematic representation of electrospinning set-up [98].

II.2.3 Effects of parameters on electrospinning

During the electrospinning process, the polymer solution is converted into nanofibers. Multiple factors influence the process and are categorized into solution parameters, electrospinning parameters and environmental parameters.

- **Parameters related to the solution**

The concentration of a polymer solution is a key parameter in electrospinning, influencing fiber formation and morphology. A low polymer concentration leads to insufficient chain entanglement, resulting in bead formation instead of continuous fibers. On the other hand, an excessively high concentration increases solution viscosity, which may obstruct the flow through the needle tip and disrupt the process. Moreover, an increase in polymer concentration typically leads to thicker fibers due to higher polymer content in the jet.

Research indicates also that viscosity plays a key role in determining fiber diameter and morphology. Increasing viscosity through molecular weight or elevated polymer concentration results in the production of polymer fibers with larger diameters, reduces the probability of bead formation, and yields fibers that are more uniform in appearance. At very low viscosities, the lack of chain entanglement prevents the formation of continuous fibers, resulting in the fiber jet breaking into droplets. Conversely, a polymer solution with high viscosity presents challenges in jet formation, as the polymer flow ceases at the needle's tip.

In electrospinning, each polymer has an optimal viscosity which has significant influence on morphology of the resulting polymer nanofiber. For instance, studies indicates that polyethylene oxide (PEO) solutions must exhibit a viscosity range of 800 to 4000 cP to ensure the production

of stable fibers [99] (Figure II.2). In another study by Altin et al.[100] explored the effect of polymer concentration on the production of polyacrylonitrile (PAN) nanofibers. The results demonstrated that increasing the polymer concentration in the solution led to enhanced viscosity, which consequently resulted in an increase in fiber diameter.

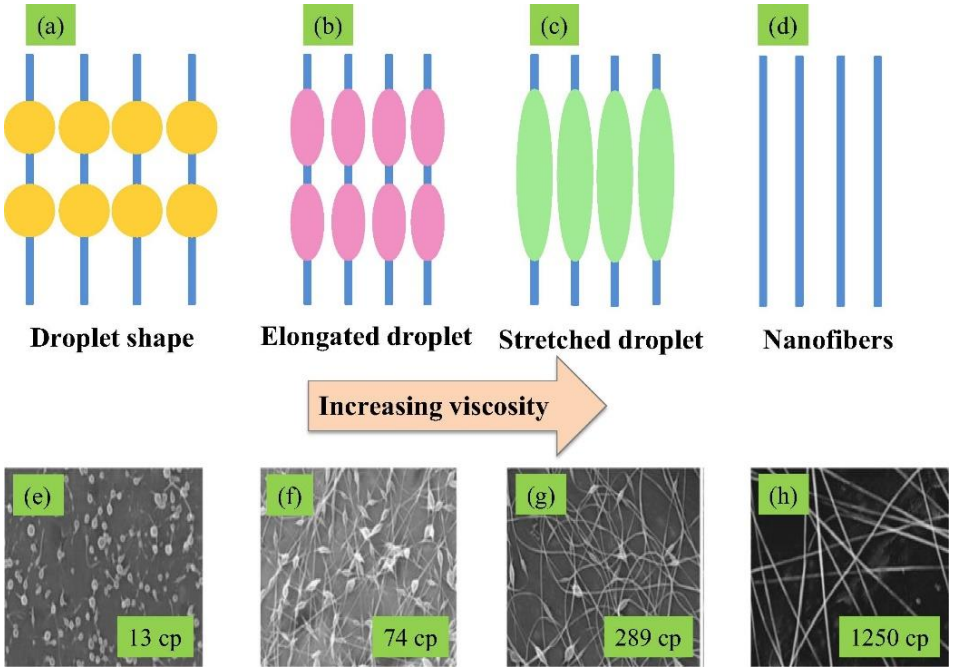

Figure II.2: Variation in morphology of electrospun nanofibers of PEO with viscosity: (a–d) schematic and (e–h) SEM micrographs [99].

Furthermore, the choice of solvent in electrospinning is essential for the generation of smooth, bead-free electrospun nanofibers. The solvent must exhibit appropriate properties, such as an optimal evaporation rate, boiling point, and vapor pressure, to enable efficient fiber generation. In electrospinning, the polymer jet shifts from the needle tip to the collector, where solvent evaporation and phase separation occur, thereby significantly affecting the resulting fiber structure.

Various solvents, such as ethanol, chloroform, DMF, and tetrahydrofuran (THF), are frequently employed. The choice of solvent influences both fiber diameter and porosity. Highly volatile solvents, such as tetrahydrofuran (THF), exhibit rapid evaporation, resulting in porous fibers with enhanced surface area. In contrast, less volatile solvents like DMF yield smoother fibers. The evaporation rate requires careful regulation, as rapid evaporation may lead to flat fibers caused by trapped solvent. Kanani and Bahrami [101] investigated the effect of solvent on the morphology of polycaprolactone (PCL) nanofibrous. SEM images revealed the formation of

beads and variations in fiber diameter (Figure II.3). Additionally, surface tension plays a role in fiber formation. According to Renker and Doshi [99], the creation of fibers without beads is facilitated by lowering surface tension of the polymer solution. Since surface tension is more dependent on composition of the solvent than on concentration of polymer.

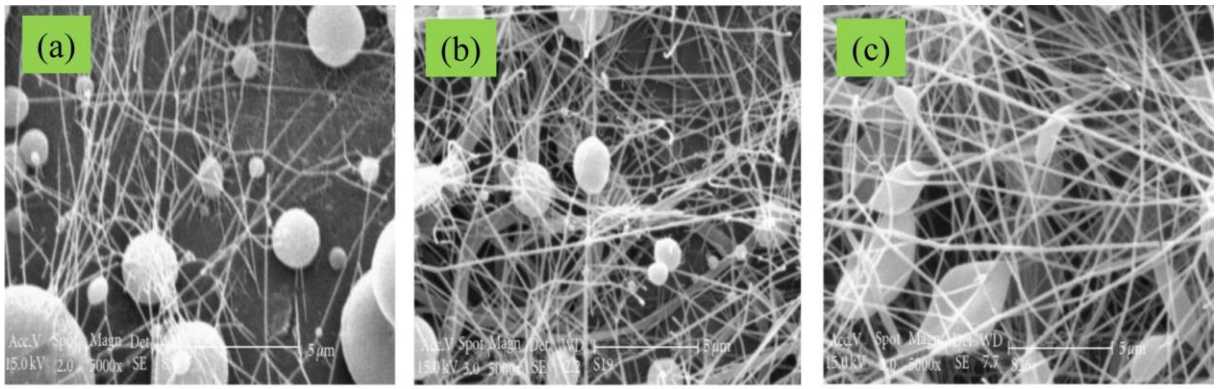

Figure II.3: SEM images of 5% PCL solutions dissolved in different solvents: (a) glacial acetic acid, (b) 90% acetic acid, (c) methylene chloride/DMF = 4/1 [101].

One other thing, the electrical conductivity of a polymer solution determines how charges distribute along the fiber jet, affecting fiber diameter and uniformity. When conductivity is higher, the jet experiences stronger stretching forces, which helps to produce finer and more uniform fibers. Adding salts or metal nanoparticles, can boost conductivity, making fiber formation smoother and reducing defects like bead formation, Fong et al.[102] investigated the effect of the addition of NaCl and its impact on the electrospinning process of PEO. The addition of salt led to a reduction in bead content and an enhancement in fiber uniformity due to the increase of solution conductivity (Figure II.4). However, if the conductivity is too high, the jet can become unstable, leading to inconsistencies in fiber diameter. On the other hand, when conductivity is too low, the stretching forces are weaker, resulting in thicker, less uniform fibers with more beads. For instance, natural polymers like gelatin, which have low conductivity, often require the addition of salts to achieve well-formed fibers [96,103].

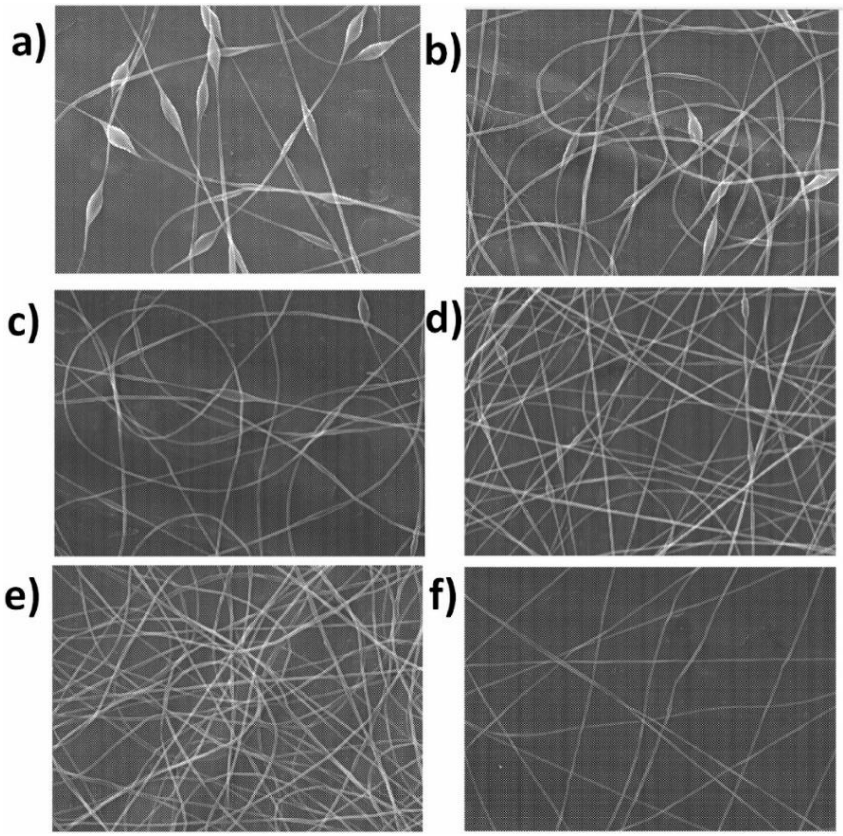

Figure II.4: Effect of conductivity on bead content of PEO nanofibers due to the addition of NaCl at a) 1.23, b) 1.77, c)3.03, d) 6.57, e) 8.67, f) 28.8 Coulomb/L [102].

- **Parameters related to processing**

The applied voltage influences directly fiber formation and morphology, it plays an essential role in the electrospinning process.

Generally, it is a known fact that the flow of current from a high-voltage power supply into a solution through a metallic needle, the resulting electrostatic forces induce the deformation of a spherical droplet into a Taylor cone, leading to the formation of ultrafine nanofibers at a critical voltage (Figure II.5).

Each polymer system has a specific critical voltage; near this voltage, charge repulsion within the polymer jet enhances stretching, resulting in thinner fibers. If the applied voltage is too low, the polymer jet may not form, while excessive voltage, can lead to the formation of nanofibers with beads. Altin et al.[100] proved in their study that thinner PAN nanofibers were obtained by increasing the voltage.

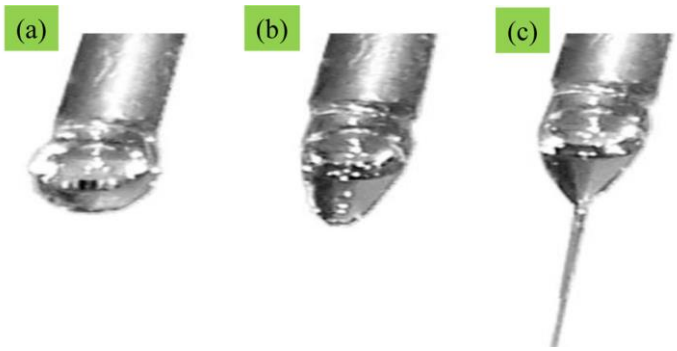

Figure II.5: (a–c) Digital images showing the three-stage deformation of the polyvinylpyrrolidone droplet under the influence of increasing the applied voltage [104].

Another important parameter influencing the morphology of electrospun nanofibers is the flow rate of the polymer solution through the metallic needle tip. Each polymer system has a critical flow rate at which uniform, bead-free nanofibers can be produced. For example, in polystyrene, increasing the flow rate to 0.10 mL/min results bead formation, while reducing it to 0.07 mL/min produced uniform, bead-free nanofibers.

A minimum flow rate is preferred to allow the formation of a stable jet cone and sometimes a receded jet (a jet that emerges directly from the inside of the needle with no apparent droplet or cone). Receded jets are not stable jets, and during the electrospinning process, these jets are continuously replaced by cone jets. As a result of this phenomenon, nanofibers with a wide range diameter are formed. In addition to bead formation, in some cases, at an elevated flow rate, ribbon-like defects and unspun droplets have also been reported in the literature due to the non-evaporation of the solvent and low stretching of the solution between the needle and metallic collector [103,105].

Other than that, any change in the surface charge density may also affect the morphology of the nanofiber. For instance, Theron et al.[106] revealed that the flow rate and electric current are directly related to each other. They studied the effects of the flow rate and surface charge density using various polymers, including PEO, polyacrylic acid (PAA), polyvinyl alcohol (PVA), polyurethane (PU), and PCL. In the case of PEO, they observed that an increase in the flow rate simultaneously decreased the surface charge density; because more solution was delivered, leading to a thicker jet with a lower charge-to-mass ratio. This resulted in less stretching and an increased risk of fiber defects.

One more significant factor is the distance between the metallic needle tip and collector. Similar to the applied voltage and flow rate, it also differs with the polymer system.

The nanofiber morphology could be easily affected by the distance because it depends on the deposition time and evaporation rate. Hence, a critical distance needs to be maintained to prepare smooth and uniform electrospun nanofibers, and any changes on either side of the critical distance will affect the morphology of the nanofibers.

Several research groups have investigated the influence of the distance between the needle tip and the collector on nanofiber morphology. They found that a shorter distance led to the formation of defective and larger-diameter nanofibers, while increasing the distance resulted in thinner fibers [107]. However, there are cases where no effect on the morphology of the nanofiber was observed with a change in the distance between the metallic needle and collector [96,103].

- **Parameters related to environmental factors**

Beside the parameters related to processing and solution, recently it has been reported that the quality of electrospun nanofibers is strongly affected by environmental factors such as temperature, airflow velocity, and humidity, along with electrospinning equipment and substrate properties. While electrospinning is typically carried out at room temperature, raising the temperature from 25°C to 60°C reduces fiber diameter due to lower viscosity, as viscosity decreases with increasing temperature.

Humidity also affects the morphology of fibers. At higher humidity levels, small spherical pores start to form on the fiber surface, and as humidity increases further, these pores gradually merge. In contrast, very low humidity accelerates solvent evaporation, causing the solution to dry too quickly, which can disrupt fiber formation. However, excessive humidity may lead to uncontrolled solution discharge, affecting fiber uniformity.

Changes in any parameter among these sets will definitely change the evolution of the electrospinning process and, thus, will change the characteristics of the resulting nanofibers. Therefore, it is important to investigate these parameters within their containing sets and assess respective effects on the process [96,103].

II.3 Electrospun nanofibers in advanced applications

Electrospinning technology experienced a dramatic development due to the convenience of producing nanofibers and huge potential of these fibers for varied applications.

In the past decade, hundreds of polymers have been successfully electrospun into nanofibers, including commercially available polymers like nylons, PEO, PAN, polyvinyl alcohol (PVA), poly-L-lactide (PLLA), polyvinylidene fluoride (PVDF), etc. Among this, PAN was a popular choice because of its good mechanical strength, chemical resistance and thermal stability, also

it is widely used in applications involving sensors and storage devices. Therefore, the focus of this work will be placed on PAN based nanofibers [22,108].

PAN is a synthetic polymer composed of repeating acrylonitrile units, it is widely used and valued for its remarkable properties. Its ability to form composites and blends with a variety of materials further enhances its versatility across different applications [22]. Moreover, PAN's low production cost and its suitability for producing fine fibers ranging from tens to hundreds of nanometers in diameter make it especially attractive for large-scale use in advanced materials [109,110].

Electrospun fibers are no longer limited to single-component polymers; they now also come from polymer blends and hybrid materials, including combinations with metals, metal oxides, ceramics, carbon nanotubes, and even biological entities like bacteria, viruses, and enzymes. This variety enhances the uniqueness of 1D fibrous structures, adding functionalities such as optical, electronic, sensing, magnetic, and catalytic properties, which broadens their applications in areas like tissue engineering, drug delivery, filtration, textiles, sensors, fuel cells, batteries, catalysis, and nanocomposites [108].

To form PAN based nanocomposite fiber, various strategies have been used to modify the polymer and fiber structure. incorporating nanofillers such as graphene, GO, CNT, and inorganic nanoparticles in nanofibers has been used as a facile and effective way to introduce functionalities (strength, stiffness, and electrical conductivity) in nanofibers. Additionally, electrospinning has been defined as a convenient technique for facilitating the self-assembly, effective orientation, dispersion, and alignment of nanoparticles. Other than that, the strong interfacial bonding between PAN's negatively charged –C≡N functional groups and nanofillers play a key role to enhance the mechanical, thermal, and other properties.

PAN nanocomposite fibers based on graphene and its derivatives have attracted significant attention due to their remarkable mechanical and electrical performances [111]. Electrospinning has also been one of the primary methods for making such nanocomposites, Uddin et al.[112] showed in their study that electrospun PAN-graphene nanofibers exhibited higher thermal stability and mechanical properties than neat PAN nanofibers.

Furthermore, Surface modification and the use of graphene derivatives further improve their various properties. For instance, Kaur et al.[113] optimized the structural morphology of PAN-CNT nanofibers by adjusting electrospinning parameters, highlighting their excellent mechanical properties. Simultaneously, Abdel-Mottaleb et al.[114] reported an enhancement of 64.4% in tensile strength and an improvement of 71.4% in Young's modulus with the

incorporation of just 1 wt% GO into PAN nanofibers. Zhang et al.[115] produced GO-coated aminated PAN (APAN-GO) nanofibers via electrospinning, demonstrating their effectiveness in oil–water separation. In a different study, Wang et al.[116] explored PAN-GO nanofibers as suitable materials for enzyme immobilization, and studied the mechanical properties, such as elasticity.

Another study by Ma et al.[117] fabricated polyethyleneimine (HPEI)-grafted PAN-GO nanofibers and used them for the recovery of Ag(I) from aqueous solutions. The same research group later modified GO with HPEI as well and incorporated it into electrospun nanofibers, which were then employed as efficient adsorbents for the recovery of Au (III) from wastewater [118].

Besides graphene derivatives nanofillers, various inorganic nanoparticles were incorporated into PAN nanofibers to align its properties with particular applications [119]. For example, PAN-Ag nanofibers have been developed for antibacterial applications [120], while PAN-Fe_2O_3 and PAN-ZnO nanofibers have been investigated as CO_2 sensors [121]. Similarly, Ozcan [122] doped PAN with ZnO nanoparticles revealing substantial improvements across radiation protection. Mpukuta et al.[123] reported that doping PAN with Cu nanoparticle improved electrical conductivity by a factor of 2.37. Furthermore, Wang et al.[124] electrospun PAN-ZrO_2 nanofibers, for fluoride removal from water, while in a work by Sharma et al.[125] in which they demonstrated the effectiveness of these nanofibers in removing Hg (II) from water.

It is evident as well that incorporating hybrid nanofillers into PAN nanofibers creates a synergistic effect, significantly enhancing their performance in advanced applications. As evidenced by Abdel-Mottaleb et al.[126] who demonstrated that PAN-GO-ZnO nanofibers improved notably both photocatalytic activity and mechanical properties. In a different study, Sigwadi et al.[127] doped PAN nanofibers with ZrO_2 and GO, to enhance the fuel cell performance and the conductivity of Nafion. In addition, Sahoo et al.[128] synthesized PAN-GO-Fe_3O_4 nanofibers, which were successfully used for Cr (VI) remediation from aqueous solutions. Recently it has been reported by Wang et al.[129] who enlightened the successfully developed PAN-TiO_2-Ag nanofibers for application in wastewater purification, indicating their excellent photocatalytic activity in degrading dyes under visible light and their good antibacterial activity. Hartati et al.[130] fabricated same nanofibers but for different application they revealed that PAN-TiO_2-Ag nanofibers are suitable to be applied on air filtration media with photocatalytic activity for self-cleaning performance.

II.4 Methods for fabricating electrospun nanocomposite fibers

Electrospun nanocomposite fibers are generated by two main approaches. The initial method involves the indirect production of fibers, achieved through the application of post-processing techniques following the electrospinning phase. This approach is especially beneficial when nanoparticles exhibit poor dispersion in the initial solution or when large-scale production presents difficulties.

One of the simplest post-processing methods involves surface modification of the electrospun fibers. In this technique, the modified fibers are immersed in a colloidal nanoparticle solution, allowing the nanoparticles to adhere to the fiber surfaces through electrostatic interactions, hydrogen bonding, or functional group-based interactions. For example, Zhang et al.[115] fabricated PAN-GO nanofibers by initially treating PAN nanofiber mats with diethylenetriamine (DETA) to produce aminated PAN (APAN). The APAN mats were subsequently immersed in a homogeneous graphene oxide (GO) solution, facilitating the grafting of GO onto their surfaces through a nucleophilic reaction involving the amine groups of APAN and the carboxyl or epoxy groups of GO (Figure II.6).

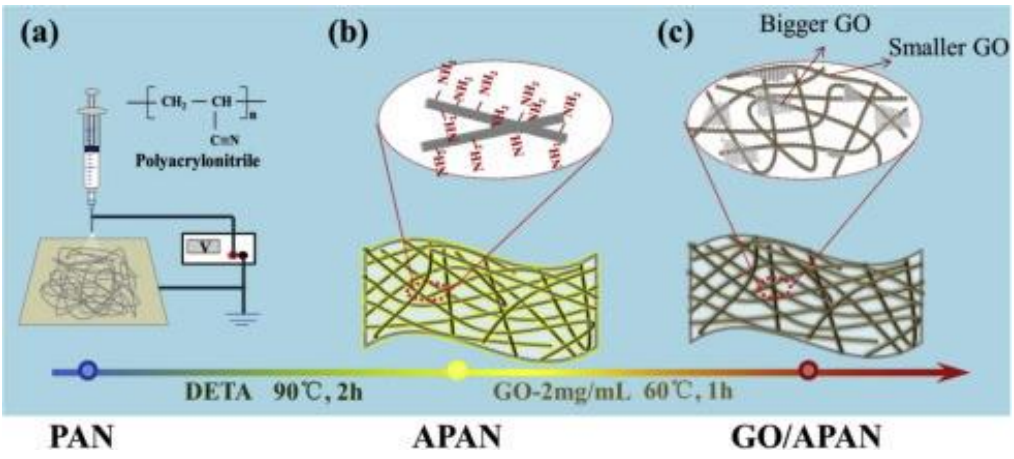

Figure II.6: Design and processing of the GO/APAN nanofibers [115].

In some cases, fiber surfaces are chemically stable and do not easily adsorb nanoparticles. So, nanoparticles can be formed directly on the fiber surfaces through an in-situ reduction process. This requires immersing the electrospun mats in a solution containing metal ion precursors, which interact with functional groups on the fiber surface. Nanoparticles are then generated by reducing the metal complexes using either a chemical reducing agent or photoreduction. In a study conducted by Karbownik et al.[131] in which they developed PAN-Ag nanofibers using silver nitrate ($AgNO_3$) as the silver ion precursor and ascorbic acid ($C_6H_8O_6$) as the reducing

agent. Initially, silver nitrate was dissolved in a PAN/DMF solution under stirring. Then, a solution of ascorbic acid, also prepared in DMF, was added to the polymer mixture, facilitating the reduction of silver ions during the preparation of the spinning solution.

The second method involves the direct formation of nanocomposites during the electrospinning process. In this method, pre-synthesized nanomaterials are uniformly dispersed within the polymer solution, which is then electrospun to produce nanocomposite fibers in a single step. This straightforward and efficient technique has become widely adopted for fabricating a variety of nanocomposites incorporating different types of nanoparticles. For instance, Sahoo et al.[128] synthesized PAN-GO-Fe_3O_4 nanofibers using a simple one-step electrospinning method. To begin, PAN solution was prepared by dissolving PAN powder in DMF. Then, pre-synthesized GO and Fe_3O_4 powder were gradually added to the PAN solution and thoroughly stirred to ensure uniform dispersion before electrospinning (Figure II.7).

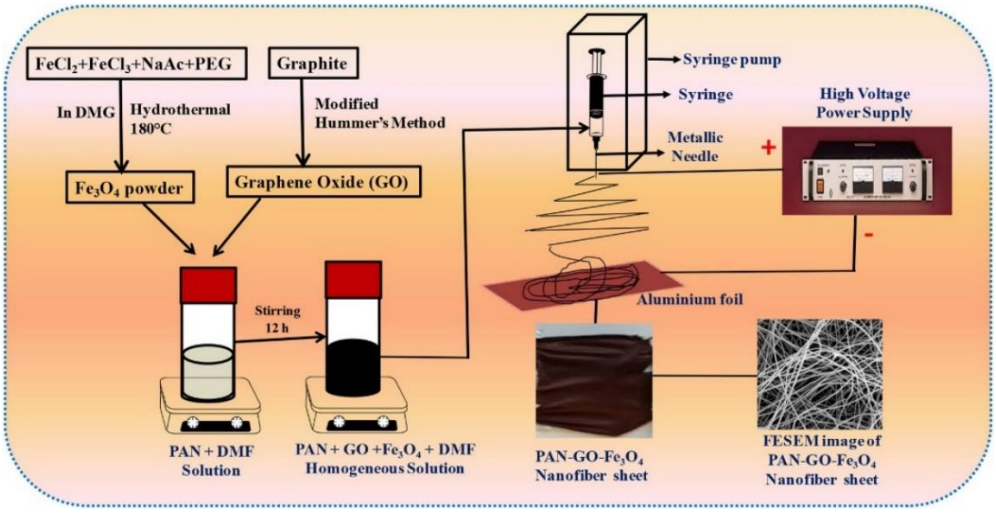

Figure II.7: Overall synthetic procedure for the synthesis of PAN-GO-Fe_3O_4 nanofibers [128].

Chapter III: Advancements in Triboelectric Nanogenerators: Mechanisms, Materials, and Performance Enhancement

Chapter III: Advancements in Triboelectric Nanogenerators: Mechanisms, Materials, and Performance Enhancement

Table of Content

Chapter III: Advancements in Triboelectric Nanogenerators: Mechanisms, Materials, and Performance Enhancement

Chapter objective

This chapter provides a comprehensive overview of triboelectric nanogenerators (TENGs), detailing their fundamental operating modes and working mechanisms. It examines key strategies for enhancing device performance, through material selection, surface engineering, and nanoscale structuring contribute to improved energy harvesting efficiency.

III.1 Nanogenerators

Nanogenerators are small-scale energy-harvesting devices that convert ambient energy such as human motion, vibrations, water flow, and wind into electricity. Typically, these devices rely on effects like piezoelectric, triboelectric, pyroelectric, and electromagnetic induction, and are used to power low-power electronic devices like sensors, wearable electronics, etc.

Devices based on piezoelectric nanogenerators (PENGs) and triboelectric nanogenerators (TENGs) are essential components of the power generating field. Their characteristics include a lightweight, sustainable, and stand-alone design, which facilitates efficient energy utilization. Since Wang et al.[18] introduced a zinc oxide nanowire-based PENG in 2006, it has been recognized as a significant advancement in energy harvesting. The operational principle of PENGs is based on the piezoelectric effect, which generates charge separation both negative and positive through the deformation of piezoelectric material when exposed to mechanical energy, thereby producing a piezoelectric potential.

In 2012, Wang's research group [19] developed TENGs for the first time by combining the triboelectric effect with electrostatic induction. Due to its simple method, low cost, and high conversion efficiency, it has emerged as the most effective energy harvesting technology [132]. Despite the significant roles of both PENGs and TENGs in energy harvesting, this work will specifically focus on TENGs.

III.2 Triboelectric nanogenerators (TENGs)

A TENG is a device designed to convert mechanical energy into electrical energy through the combined effects of contact electrification (the triboelectric effect) and electrostatic induction. It typically consists of two triboelectric layers (dielectric materials) one tribopositive and the other tribonegative. The tribonegative layer is made from a material with a strong tendency to gain electrons while the tribopositive layer is made from a material that readily loses electrons. When these two layers come into contact and then separate, opposite charges are generated on their surfaces. However, the exact mechanism of charge formation on triboelectric surfaces remains unclear and is still a topic of ongoing debate. Electrodes, usually made of conductive

materials like aluminum or copper, are placed behind these triboelectric layers to collect and transfer the induced charges. The entire structure is often supported by a flexible or rigid substrate, such as polyethylene terephthalate (PET) or paper, and may include a spacer to control the contact and separation motion [132–134].

As indicated previously, TENGs operate based on the combined principles of triboelectrification and electrostatic induction. Triboelectrification involves the generation of surface charges resulting from the contact between two distinct materials which is one of the most frequently experienced effect that each and every one of us inevitably uses every day. Electrostatic induction, on the other hand, refers to the transfer of electrons between electrodes through an external circuit due to a difference in electric potential [135–137].

The discovery of TENGs occurred unexpectedly when Wang and his team noted a high voltage output during the design of a piezoelectric nanogenerator with a small gap, which was subsequently attributed to the triboelectric effect. Leading to the introduction of TENGs for the first time in 2012 by the use of flexible polymer films, Kapton, and polyester (polyethylene terephthalate, PET) as dielectric layers and gold (Au) deposited on the polymer films as electrodes [19] (Figure III.1).

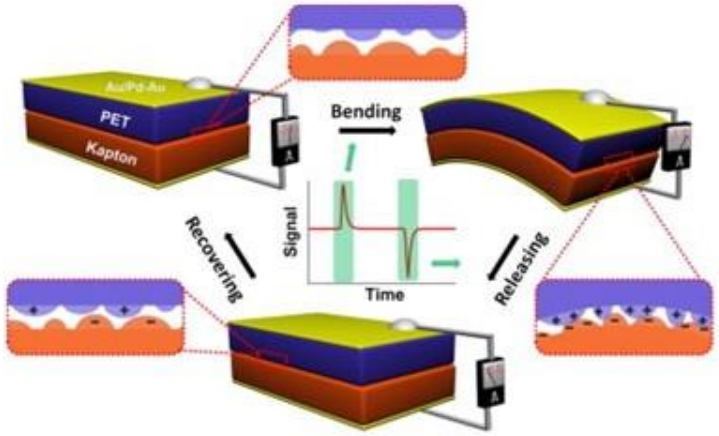

Figure III.1: Schematic illustration of the structure and working principle of the energy harvester based triboelectricity [19].

III.2.1 Operating modes of TENGS

Recent advancements have led to the identification of four fundamental working modes of TENGs: vertical contact-separation, linear sliding, single-electrode, and free-standing modes. These modes require two different triboelectric materials with proper electrode connections with proper insulation between each layer.

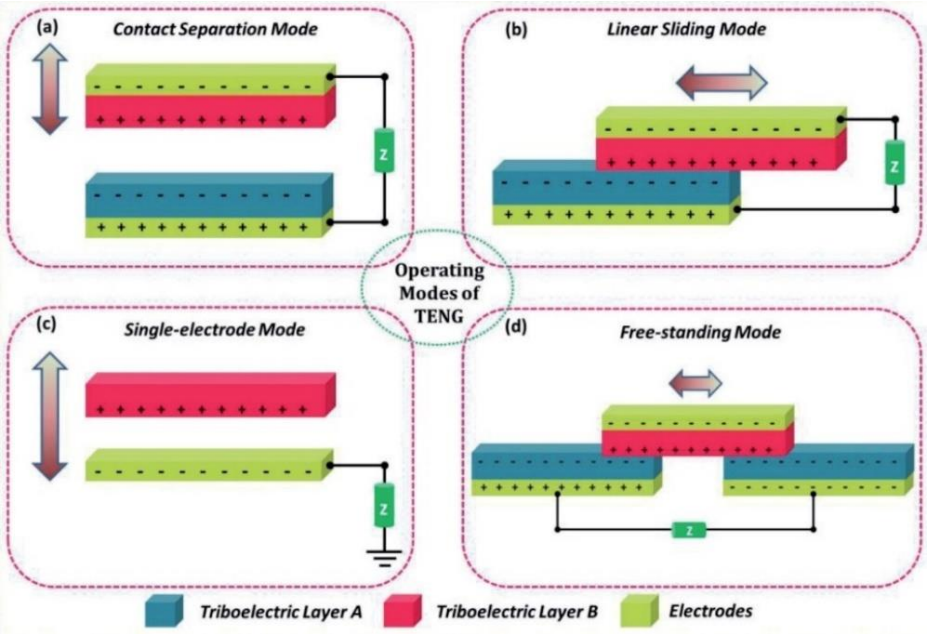

Figure III.2: Schematic representation of the four fundamental operating modes of TENG [138].

III.2.1.1 Contact separation mode

The contact separation mode TENG is the first developed. The triboelectrification occurs by the contact and separation process of two different dielectric materials or layers. The external force is applied vertically on the triboelectric materials. The charges are formed on the surface of the materials, and as they are separated by a distance, an electric potential difference is established between the two electrodes attached to the triboelectric materials. The reciprocal motion of the materials can produce alternating current (Figure III.2a). This mode has a significant advantage with its simple design, easy fabrication, and low cost. It is applied generally to harvest mechanical energy from human motions, the vibration of a machine, wind, flowing water [132,138].

III.2.1.2 Linear sliding mode

In the linear sliding mode, the charge generation is by the relative to and from sliding between the layers of TENG. The construction is almost similar to the contact separation mode with electrodes attached to the back of the triboelectric layers, but the displacement is in sideward (Figure III.2b). This mode offers the advantage of generating increased charge density with a highly effective charge generation, attributed to its high contact area. Furthermore, the incorporation of additional grating structures can improve output performance. Adding that this mode is capable of operating in a rotational manner with cylindrical grating structures. It is used to generate power from rotational motion, waves, and pressure or touch [132,138].

III.2.1.3 Single-electrode mode

The simplest structure of TENG is the single-electrode mode TENG, unlike in the other two operation mode. It has a triboelectric surface and only one electrode grounded (Figure III.2c). The output performance is insufficient due to limited charge transfer, resulting in reduced voltage and current generation; however, it is well-suited for self-powered applications.

It is used to harvest energy from moving objects, such as turning book pages, raindrops, rotating tires, and footsteps [132,138].

III.2.1.4 Free-standing mode

The free-standing mode is used to harvest energy from moving objects. A pair of identical electrodes are placed below the triboelectric layer with a gap distance. An asymmetric charge distribution is generated in the media as the triboelectric layer is brought in contact and separated from the electrodes. Due to this, the electrons will flow between the electrodes to equate the potential distribution (Figure III.2d). This mode of TENG device has a high figure-of-merits and has demonstrated high output efficiency and electrical output. This type of device can be fabricated easily and integrated into various real-time applications. It harvests energy from automobiles, human walking, air flow, computer mouse operation [132,138].

III.2.2 Triboelectric materials

There is a wide range of triboelectric materials that can be utilized to construct an effective TENG device. The choice of material plays a crucial role in determining the overall performance of the generator, as the triboelectric polarity (whether a material tends to gain or lose electrons) and the surface charge density directly influence the amount of electricity that can be generated. These properties govern the ability of a material to act as either a tribopositive or tribonegative layer. Therefore, careful selection of triboelectric materials is a critical step in the design and fabrication of high-efficiency TENGs [139].

Materials are commonly chosen based on their positions in the triboelectric series (Figure III.3), ordered by their tendency to gain or lose electrons upon contact with other materials. Metals such as aluminum (Al) and silver (Ag), along with organic materials like nylon, cotton, and silk, are frequently used as positive triboelectric layers due to their strong electron-donating characteristics. On the other hand, polymeric materials such as polytetrafluoroethylene (PTFE), epoxy, polyacrylonitrile (PAN), and rubber serve as excellent negative triboelectric layers, thanks to their strong electron affinity and ability to retain negative charges after separation. By carefully pairing a strong electron donor with a strong electron acceptor, the resulting TENG can maximize charge transfer and improve energy conversion efficiency [20,23].

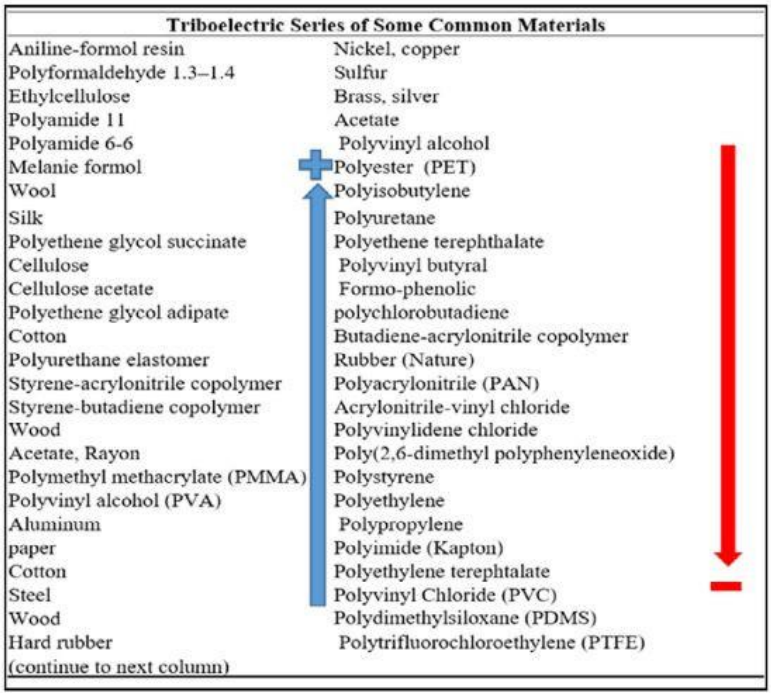

Figure III.3: Conventional triboelectric series of materials [23].

III.2.3 Working mechanism of TENGs

The operational mechanism of TENGs remains under investigation and may be subject to ongoing debate. It is generally recognized that when two distinct materials come into contact, a chemical bond, referred to as adhesion, forms between certain areas of the surfaces, leading to the transfer of charges from one material to the other in order to equalize their electrochemical potential. The transferred charges may consist of electrons or ions/molecules. Upon separation, certain bonded atoms exhibit a tendency to retain additional electrons, while others tend to donate them, potentially resulting in triboelectric charges on surfaces. The presence of triboelectric charges on dielectric surfaces can drive electron flow in the electrode to balance the generated electric potential drop. The three types of mechanisms are explained below [140].

III.2.3.1 Electron Transfer

Wang et al.[141] introduced the electron cloud overlap model to describe how charge transfer can occur between atoms. Under normal conditions, two atoms maintain a stable distance, referred to as bond length, at which their electron clouds remain non-overlapping. When an external force brings the atoms closer together, the distance becomes shorter than the bond length, causing their electron clouds to overlap. This overlap reduces the energy barrier between the atoms, making it easier for electrons to transfer from one to the other. Upon atom separation, the transferred electrons remain in place, contributing to the formation of surface charges [142,143].

III.2.3.2 Ion Transfer

Ion transfer refers to the movement of ions between two materials, this process involves the asymmetric separation of ions, which leads to the generation of frictional charges. Lin et al.[144] proposed an electrical double-layer model to describe this process at solid–liquid interfaces. According to the model, an object is surrounded by two layers of parallel charges. The first layer, known as the surface charge, is created when liquid molecules impact the solid surface due to thermal motion or pressure, causing electron cloud interactions between the two materials. The second layer is made up of ions in the liquid that are attracted to the surface charge by Coulomb forces. These ions are not fixed in place but move freely in the liquid, influenced by thermal energy [142,143].

III.2.3.3 Material Particle Transfer

Although material particle transfer is not the dominant mechanism triboelectrification unlike electron or ion transfer, it offers insight into cases those mechanisms cannot fully explain, such as contact initiation between identical materials [145]. As proposed by Baytekin et al.[146] when two polymer surfaces come into contact, they develop a random distribution of nanosized regions with oppositely charged regions. Changes in this distribution can alter the surface composition, resulting in the transfer of material particles between the two surfaces [142,143].

III.3 Strategies for improving the TENG performance

Enhancing the charge density on the frictional surfaces is a key strategy for improving the output performance of TENGs. In recent years, numerous studies have focused on boosting charge density through appropriate material selection, nanoscale engineering, the introduction of new functionalities, charge enhancement, and power management [137,147].

The surface morphology of the contact layer significantly influences the output performance of TENGs [148]. The morphology of triboelectric materials can be modified using surface engineering techniques to effectively increase contact area and improve triboelectric performance. The techniques include surface coating, electrospinning, three-dimensional (3D) printing, and etching.

Among these methods, electrospinning allows precise control over fiber diameter and structure. It is particularly effective due to its ability to produce nanofibers with a high specific surface area, significantly leading to an increase in the friction surface and improving charge generation plus transfer efficiency in TENGs [21]. Kim et al.[149] presented a silk bio-TENG, consisting of polyimide (PI) and silk fibroin nanofibers, the SF film was produced through electrospinning,

resulting in a nanofiber network structure that enhanced both the surface-to-volume ratio and surface roughness relative to the bare film (Figure III.4a). The output voltage of the silk nanofiber was 1.5 times greater than that of the cast silk (Figure III.4b) attributed to its extensive surface area. In another study, Sun et al.[150] fabricated a nanofiber-based triboelectric nanogenerator (NF-TENG) consisted of an electrospun PA66/MWCNTs nanofiber film as the tribopositive layer and an electrospun PVDF nanofiber film as the tribonegative layer. The NF-TENG exhibits a peak voltage of 142 V, a current of 15.5 µA, and a maximum power density of 1.30 $W.m^{-2}$ [147,151].

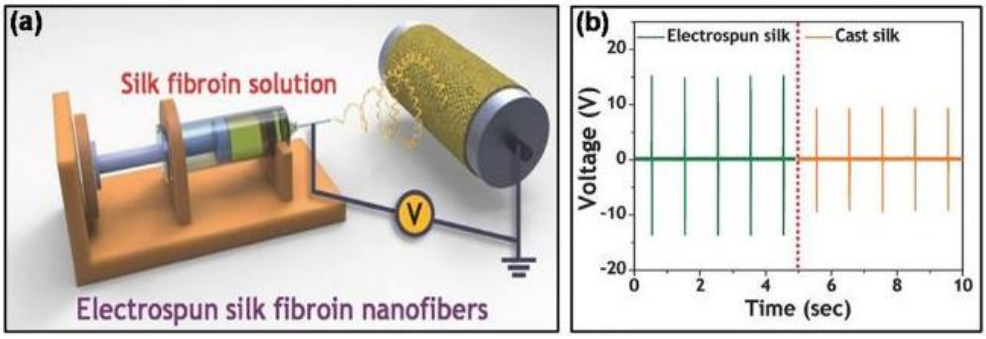

Figure III.4: (a) Schematic of electrospun SF preparation and (b) open-circuit voltage (V_{oc}) of a TENG using two types of regenerated SF [149].

Furthermore, the incorporation of nanomaterial additives into the contact layer can improve TENG performance by augmenting surface charge density and reducing triboelectric losses. These nanomaterials enhance the dielectric properties of the triboelectric material, thereby improving charge retention. The dielectric constant is essential for enhancing the output performance of TENGs [151].

For instance, inorganic fillers possessing a high dielectric constant or conductive filler have been documented as incorporated into the polymer matrix, however, only a small portion of inorganic nanomaterials have been studied in the last several years, therefore application of new types of inorganic nanomaterials in TENGs is required. Chen et al.[152] demonstrated that using strontium titanate ($SrTiO_3$) nanoparticles as additives in porous PDMS layers significantly improved the efficiency of the triboelectric layer. The peak voltage of a TENG based on composite PDMS film including 10 vol% $SrTiO_3$ nanoparticles attained a maximum value of 305 V, in contrast to the pure PDMS film, which measured only 172 V, representing an enhancement of 1.8 times. In a study conducted by Jian et al.[153] polymethyl methacrylate (PMMA)- TiO_2 composite was revealed as an effective tribopositive material for producing a high-performance triboelectric nanogenerator (TENG). When paired with PDMS, the TENG

generated a voltage of 1200 V, a current of 139 $mA.m^{-2}$, and an output power of 34.85 $W.m^{-2}$. These values represent a significant enhancement compared to the counterpart that used neat PMMA as the tribopositive material under the same operating conditions, which produced a voltage of 620 V, a current of 78 $mA.m^{-2}$, and an output power of 13.89 $W.m^{-2}$.

A single-electrode triboelectric nanogenerator (STENG) based on poly (vinylidene fluoride-co-hexafluoropropene)-ZrO_2 nanocomposite was reported by Saikh et al.[26] The STENG demonstrated remarkable output performance, generating 7 V from a simple finger touch. This promising approach offers a scalable solution for powering self-sustained systems by converting small mechanical energy from human activities into electrical energy.

In addition, the carbon-based material such as graphene, GO and CNTs are popular and widely applied to energy fields [23,154].

As previously mentioned in Chapter I, GO consists of a hexagonal carbon ring structure containing both sp^2 and sp^3 hybridization. Nonetheless, the presence of covalently bonded oxygen-containing functional groups on the GO nanosheets significantly reduces its electrical conductivity [65]. As a result, GO is less suitable for use in advanced electrical and electronic devices. However, GO has garnered considerable attention as a triboelectric material due to its capacity to gain electrons via the oxygen functional groups present on the basal planes and edges of the graphene structure. Moreover, it demonstrates notable flexibility, a significant elastic modulus, an extensive surface area, and a marked charge effect, all of which enhance the performance and durability of GO-based TENGs [23]. Huang et al.[24] produced TENGs using electrospun nanofibers composed of PVDF and poly(3-hydroxybutyrate-co-3-hydroxyvalerate) (PHBV), incorporating GO as a dopant. The addition of GO was aimed to boost the output performance of the device. The well-dispersed GO sheets within the PVDF matrix functioned as charge trapping centers, thereby improving the output performance of the TENG. The maximum output peak-to-peak voltage and current were 340 V and 78 µA, respectively, higher than those of a TENG with neat PVDF nanofibers. Parandeh et al.[155] fabricated TENG based on a silk fibroin layer and a PCL-GO layer. The results showed that the incorporation of GO notably enhanced the performance of the TENG delivering a voltage of 100 V, a current of 3.15 $mA.m^{-2}$, and a power density of 72 $mW.m^{-2}$. Jannesari et al. [156] developed a TENG consisted of polypyrrole (PPy)-GO, the open-circuit voltage and short-circuit current were obtained as 413.2 V and ~ 41 µA, respectively. A new approach was reported by Harnchana et al.[157] to modify PDMS as a negative triboelectric material using GO and a sodium dodecyl sulfate (SDS) surfactant. The TENG could deliver an output voltage and current of up to 438 V and 11 µA,

respectively. These values were 3-fold higher than those of the flat PDMS. The superior performance is attributed to the intensified negative charges on PDMS from the oxygen functional groups of GO and anionic head groups of the SDS molecules.

Besides the previously discussed modification methods, chemical modification is another promising way to increase the charge density of friction materials.

In general, materials with different charge densities can be used in TENGs, but selecting ones with good triboelectric properties is key to achieving better performance. Among the different approaches, chemical modifications that affect a material's tendency to gain or lose electrons through the addition of electron-withdrawing or electron-donating groups are some of the most commonly explored strategies to boost TENG output and expand their applications.

The introduction of electron-withdrawing groups, such as halogens or the nitro group, is effective in enhancing the triboelectric performance of materials by increasing their electron affinity. Chen et al.[158] employed crepe cellulose paper and a nitrocellulose membrane as friction layers to create a paper-based TENG (P-TENG) (Figure III.5). The P-TENG showed an outstanding triboelectric performance; a voltage, current and a high-power density of 196.8 V, 31.5 µA and 16.1 $W.m^{-2}$ respectively.

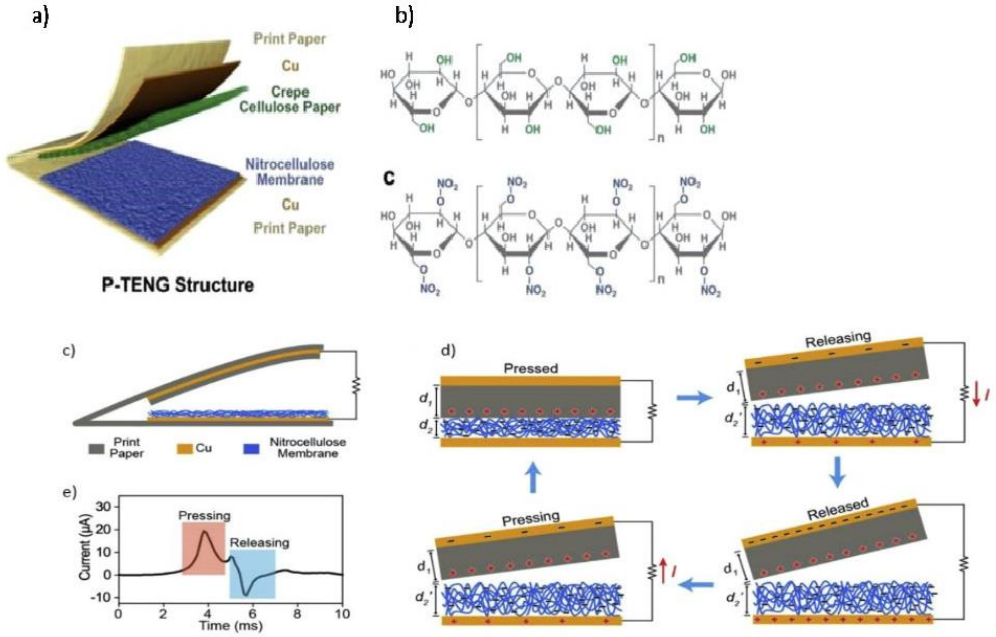

Figure III.5: (a, b) TENG based on crepe cellulose paper and a nitrocellulose membrane (P-TENG). (c, d, e) Working principle of the P-TENG containing print paper as the positive friction layer, and its short-circuit current output under one cycle of pressing and releasing [158].

When it comes to the introduction of electron-donating groups, metals are the most frequently utilized as positive materials for TENGs due to their electropositive nature. Other than that, the amino group has an excellent electron-donating ability, and many studies have been published based on amino modifications. Zheng et al.[159] demonstrated in their study that enhancing the tribopositive polarity of the cellulose aerogel film through silanization with amino silane can significantly improve the triboelectric performance [147]. Shin et al.[160] demonstrated the effect of surface functionalization on the output performance of TENGs. They functionalized the surfaces of the PET films either with poly-l-lysine solution or trichloro perfluorooctyl silane. The fabricated TENGs showed a maximum voltage open-circuit of ~330 V. In another work, Shin et al.[161] studied various surface functionalization, multiple PET films were used as substrates, with each surface selectively functionalized to exhibit either electronegative or electropositive behavior. Cl, F, Br, and H were used for electronegative functionalization, while linear poly (ether imide) (PEI(l)), branched poly (ether imide) (PEI(b)), hexyltrimethoxysilane (HTMS), poly-L-lysine (PLL), and APTES were applied for electropositive functionalization (Figure III.6). The results indicated that the higher output power of 55 $W.m^{-2}$ was achieved using the combination of Cl and PEI(b).

In summary, the choice of materials, surface structure configurations and patterning, surface functionalization, and the incorporation of nanomaterials are important factors that need to be considered to enhance the output performance of TENGs.

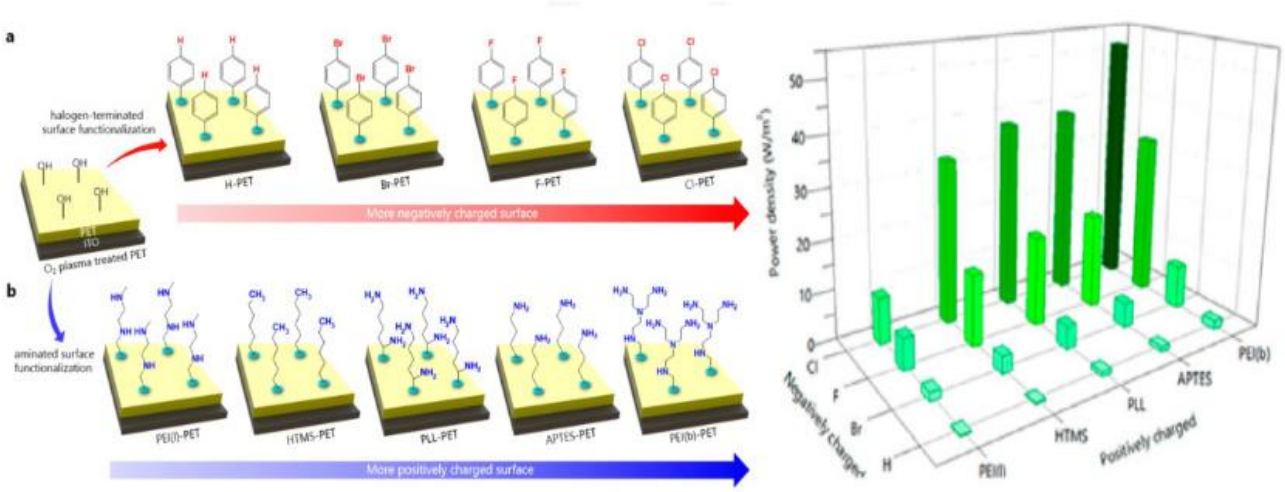

Figure III.6: Schematic representations of surface-functionalized negative and positive PETs with the molecules adopted here (left). Power density of TENGs with different contact pairs (right) [161].

III.4 Electrospun PAN nanofibers-based TENGs

PAN has emerged as a widely used material in TENG applications due to its capability to produce fine nanofibers and its ease of modification. Through the incorporation of functional materials, surface modifications, or nanomaterials, PAN can be adapted to enhance charge generation and maximize the efficiency of TENG devices [109].

Kinas et al.[162] achieved a substantial enhancement in the output voltage of TENGs by grafting rGO and CNTs onto PAN nanofibers. This modification led to a notable 125% increase in maximum peak power density.

A separate study by Zhuo et al.[163] focused on enhancing the tribopositive performance of PAN-based TENGs through the incorporation of molybdenum disulfide (MoS_2) nanosheets. MoS_2 was added at varying concentrations (1, 2, 3, and 4 wt%) to PAN nanofibers using electrospinning. The resulting nanocomposite fiber-based TENGs exhibited significantly improved triboelectric outputs. Notably, the TENG fabricated with 4 wt% MoS_2 achieved a peak open-circuit voltage of 296 V and a short-circuit current of 6.16 µA representing enhancements of approximately 95% and 77%, respectively, compared to pure PAN nanofiber-based TENGs.

In another work by Yar et al.[25] PAN/boric acid $B(OH)_3$ was employed as the tribopositive dielectric layer, while polyvinyl butyral (PVB) served as the tribonegative counterpart. The study revealed that the TENG achieved a peak power density of 6.67 $W.m^{-2}$.

Ye et al.[164] demonstrated that incorporating liquid metal (LM) particles into electrospun PAN films can significantly enhance triboelectric performance. As LM concentration increased, the output parameters of the TENGs improved correspondingly. At approximately 1.5 wt% LM content, the current density and the output voltage, increased by about 40% and 70% respectively. A study by Tabassian et al.[165] where they revealed that the addition of zeolitic imidazolate framework-8 (ZIF-8) nanocrystals to PAN-based electrospun nanofibers was found to enhance the output performance of the TENGs; the output voltage gradually increased to 178 V while the current value reached 7.5 µA.

These enhancements in TENG performance have directly contributed to the development of various functional devices for real-world applications. For instance, Varghese et al.[166] developed a self-powered sensing system using a PAN nanofiber layer in contact with a PDMS layer. This design enabled the detection of nearby objects without the need for an external power source.

In the area of air filtration, Yang et al.[167] designed a TENG-based self-powered filter. They used electrospun poly butanediol succinate (PBS) nanofibers as the tribopositive layer and PAN/ PS nanofibers as the tribonegative layer. The device produced an open-circuit voltage of 8 V.

To create a self-charging power system, Park et al.[168] combined a TENG with a supercapacitor. the electrospun nanofiber of PAN and nylon 66 were applied to the dielectric layer of a TENG, while the PAN and PANI composites were utilized as an electroactive material of supercapacitor. The device was able to power a commercial LED.

For wireless communication applications, Pandey et al.[169] developed a piezoelectric-triboelectric nanogenerator (PZ-TENG) for a self-powered visible light communication (VLC) system. They used PAN nanofibers embedded with ZIF-8 as the tribopositive layer and a PTFE film as the tribonegative layer. The modified PAN nanofibers produced three times higher output voltage than unmodified ones, making the system suitable for wireless human-machine interfaces [21,109,170].

Chapter IV: Experimental Insights into Nanomaterials and Nanofibers Production

Chapter IV: Experimental Insights into Nanomaterials and Nanofibers Production

Table of Content

Chapter IV: Experimental Insights into Nanomaterials and Nanofibers Production

Chapter objective

The objective of this chapter is to present the materials and experimental procedures used throughout this work. It includes the synthesis of GO and GO-ZrO_2 nanohybrids, as well as their incorporation into PAN matrix then fabricate electrospun nanofibers. The chapter also describes the steps involved in fabricating the nanomaterials and the nanocomposite fibers, it explains also the characterization techniques used to evaluate the structural and the functional properties of the fabricated materials in order to be used as layers for triboelectric nanogenerators (TENGs).

IV.1 Chemicals and Reagents

IV.1.1 Chemicals Used in the Synthesis and Functionalization of GO

The powder of natural graphite with particle size (<20 µm) was received from Sigma-Aldrich under CAS number 7782-42-5. The chemical reagents needed to synthesize graphene oxide (GO) were purchased from Sigma-Aldrich. These reagents included sodium nitrate ($NaNO_3$, 99 %), sulfuric acid (H_2SO_4, 98 %), hydrogen peroxide (H_2O_2, 30 %), and hydrochloric acid (HCl, 37 %). Potassium permanganate ($KMnO_4$, 99.5 %), was bought from Fisher. Jinan Future Chemical of China supplied the N-(b-aminoethyl)-c-aminopropyltrimethoxysilane (AEAPTMS; Z-6020, >98 %), it was employed for silanization. Sigma-Aldrich supplied zirconium oxide nanoparticles (ZrO_2) to decorate the surface of GO and the ethanol (C_2H_5OH; 98 %). All chemicals were used without further purification.

IV.1.2 Materials for nanofiber preparation

Polyacrylonitrile (PAN) (Mw=150000 g/mole) was sourced from J&K Scientific (Shanghai, China). N,N-dimethylformamide (DMF, ≥ 99 wt%) was acquired from Sigma-Aldrich and utilized without additional purification.

IV.2 Preparation

IV.2.1 Synthesis of graphene oxide (GO)

GO was synthesized from natural graphite powder using the modified Hummer's method [44]. Initially, 1 g of graphite powder was combined with 0.5 g of $NaNO_3$ in a three-neck flask, followed by the addition of 30 ml of concentrated H_2SO_4 to the mixture, which was then stirred. The mixture was placed in an ice bath, and then 5 g of $KMnO_4$ was gradually added to the solution in small amounts. The mixture was stirred for 12 h at room temperature. Subsequently, 30 ml of distilled water was slowly added and stirred for 30 minutes to ensure the completion

of the reaction. The solution was subsequently diluted with 100 ml of distilled water and treated with 4 ml of H_2O_2 (30% solution) to eliminate the excess of $KMnO_4$.

The mixture underwent centrifugation at 4500 rpm for 15 min. The resultant product was washed with HCl solution and then with water multiple times to remove residues. The precipitate was suspended in distilled water and exfoliated through ultra-sonication to obtain GO sheets. The obtained GO was subjected to drying in a vacuum oven at 90 °C for 24 h.

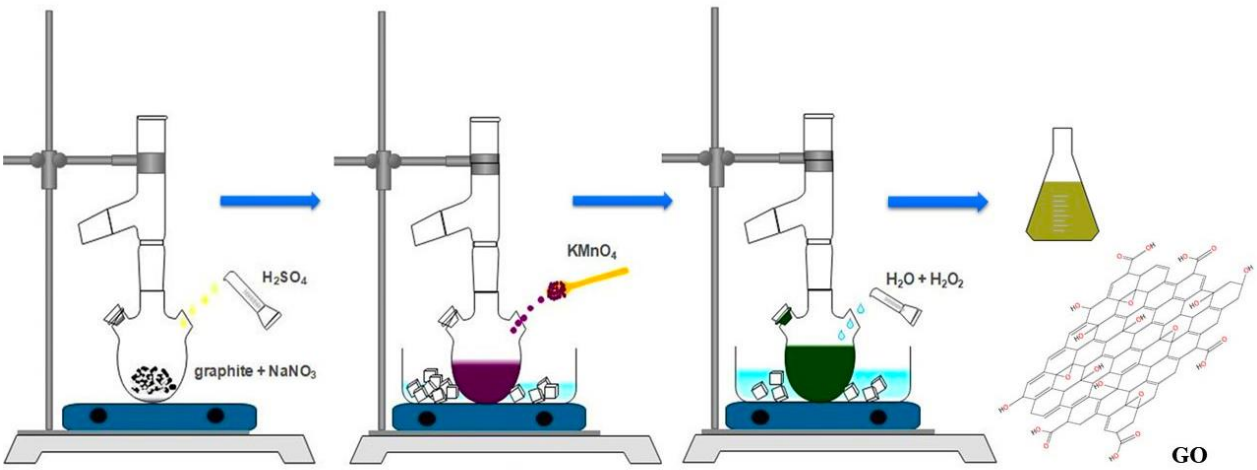

Figure IV.1: Schematic illustration of the synthesis of GO.

IV.2.2 Synthesis of silanized graphene oxide (SGO)

First, AEAPTMS was hydrolyzed in a stirring combination of alcohol and water (70/30) for 30 min, and the pH of the suspension was adjusted to a range of 4–5 using acetic acid. Subsequently GO powder was dispersed in the hydrolyzed silane within a round-bottomed flask, and the mixture was stirred for 5 h. The SGO was ultimately collected, subjected to several washings via centrifugation with water and ethanol, and then dried for 24 hours (Figure IV.2).

IV.2.3 Synthesis of SGO-ZrO_2 nanohybrids

The SGO powder was first exfoliated using sonication in water. In addition, ZrO_2 powder was dispersed in deionized water using sonication for 10 min at a concentration of 0.5 mg/ml. The two solutions were afterwards combined and stirred vigorously for 5 h in a round-bottomed flask to obtain a homogenous suspension. Ultimately, the obtained nanohybrids was collected and subjected to many washes using centrifugation processes. Then, it was dried in an oven at 70 °C for 24 h (Figure IV.2).

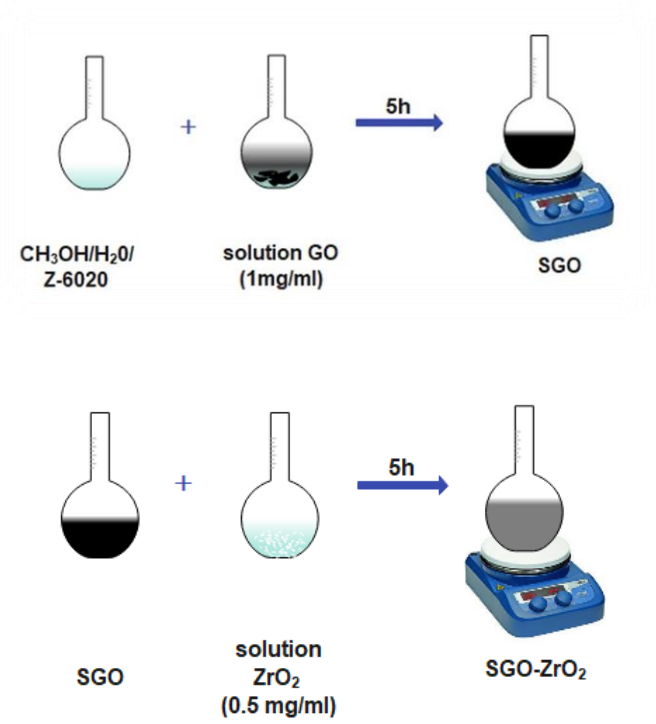

Figure IV.2: Schematic illustration of the synthesis of SGO and SGO-ZrO_2.

IV.2.4 Preparation of nanofibers solutions

The PAN spinning solutions was prepared by dissolving (7.5 wt %) of PAN in DMF at T= 50-60 °C for 3h combined with a magnetic stirrer. Then the stirring was continued for 24 h at room temperature in order to obtain a homogeneous clear solution of PAN [100].

For the PAN-SGZ spinning solutions, the various concentrations (0.25, 0.5, 1, 2 wt %) of SGZ nanofillers were sonicated in a probe sonicator for 90 min after that PAN was added in the previous solution mixed with a magnetic stirrer at T=50-60 °C for 3h. Then, the mixture was stirred continuously for 24 h at room temperature (Figure IV.3).

Table IV.1: Summary and codes of the different compositions.

Samples	Code	PAN-SGZ (wt%)	SGZ (wt%)
PAN	PAN	7.5	0
PAN-0.25% SGO-ZrO_2	PAN-0.25SGZ	7.5	0.25
PAN-0.5% SGO-ZrO_2	PAN-0.5 SGZ	7.5	0.5
PAN-1% SGO-ZrO_2	PAN-1SGZ	7.5	1
PAN-2% SGO-ZrO_2	PAN-2SGZ	7.5	2

IV.2.5 Production of the nanofibers

Fabrication of the nanofibers was achieved via electrospinning technique which is equipped with a rotating collector to improve the fiber alignment. Electrospinning solution fed into the syringe and parameters were set as follows: 2.0 ml/h feeding ratio, 25 kV, 175 mm (tip to collector distance) and 500 rpm was the rotational speed of collector (Figure IV.3).

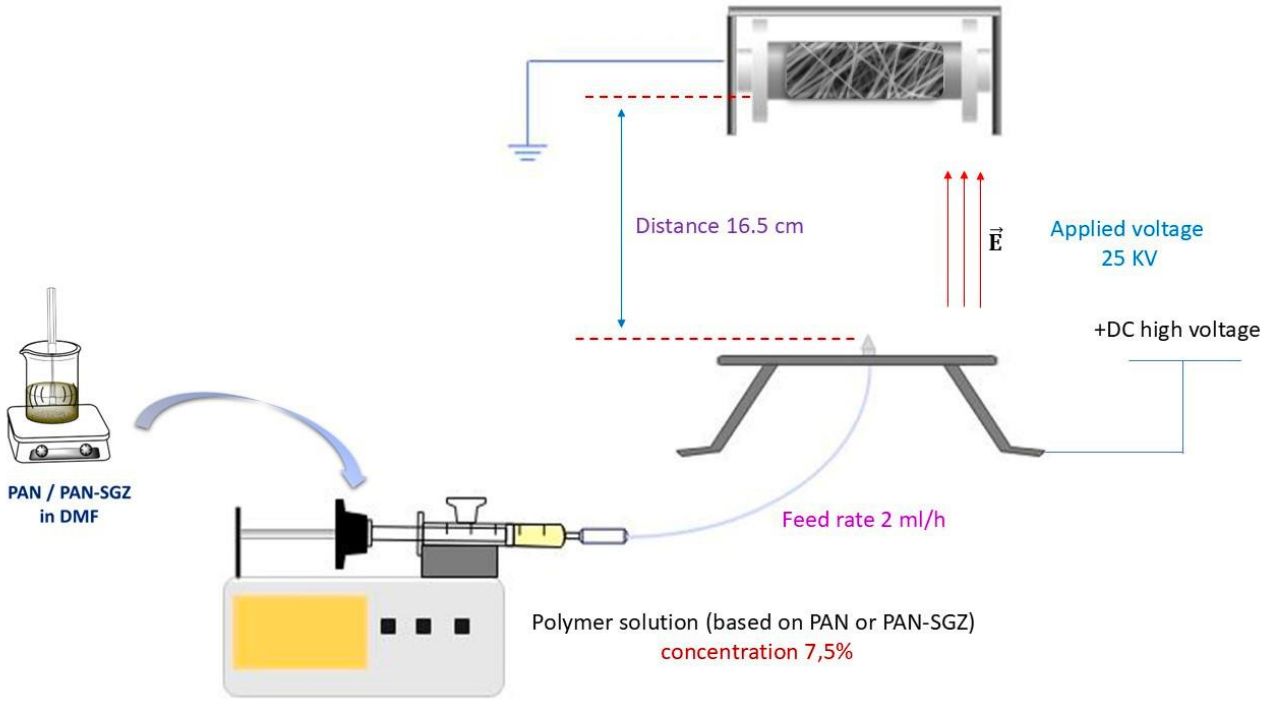

Figure IV.3: Schematic illustration of electrospinning process.

IV.2.6 TENG device fabrication

PAN-SGZ fiber mats were used as the tribopositive, while PAN fiber mats were as the tribonegative layer for the TENGs. One side of nanofibers was coated with 20 nm thick of gold by magnetic sputter. An aluminum tape was then attached to the gold-coated surface of the nanofiber mats, and electrical contact wires were connected to the aluminum tape to serve as the top and bottom electrodes (Figure 3). The electrode-integrated tribolayers were subsequently mounted on polymer plates as protective layers (Figure IV.4).

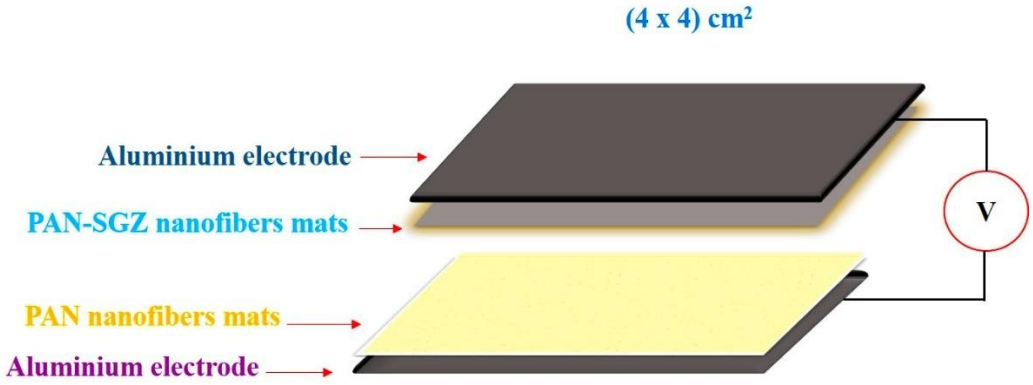

Figure IV.4: Schematic illustration of the fabrication of TENG device.

IV.3 Characterizations

IV.3.1 Fourier transform infrared (FTIR) spectroscopy

FTIR spectroscopy in the attenuated total reflectance mode (ATR-FTIR) was employed using a JASCO-IR spectrometer to investigate to verify the characteristic oxygen functionalities present on GO nanosheets and to provide evidence of successful functionalization following the grafting of silane molecules and the incorporation of ZrO_2 nanoparticles.

Concerning the nanocomposites fibers, FTIR spectroscopy was also used to investigate the interaction between nanofiller and PAN matrix. The device used is a NICOLET-IS50 spectrometer. All the analyses in the case of nanomaterials and nanocomposite fibers were conducted at room temperature and the spectra were collected in the wavenumber range from 4000 to 400 cm^{-1} at a resolution of 4 cm^{-1}.

IV.3.2 X-ray diffraction (XRD)

The crystallinity of the powders was analyzed by X-ray diffraction and the scan was operated at room temperature using a Phillips System XPERT-PRO model with a CuKα radiation (λ=1.54 Å) using a 56 kV voltage generator and 50 mA current the 2θ scanning range was 5-70° with a step interval of 0.016 °. It was used to analyze the crystal phase structure, stacking

order, and morphology of flake graphite, GO, SGO, ZrO_2, and SGO-ZrO_2 nanohybrids. The spacing between layers and the average size of the crystals can be calculated using Bragg's (Eq IV.1) and Debye-Scherrer equations (Eq IV.2), respectively. By combining these equations, the average number of graphene layers (n) per domain can be estimated (Eq IV.3).

$$d(hkl) = \frac{\lambda}{2\ \sin(\theta)} \quad \text{(IV.1)}$$

$$D = \frac{K\lambda}{\beta \cos(\theta)} \quad \text{(IV.2)}$$

$$n = \frac{D}{d} + 1 \quad \text{(IV.3)}$$

Where λ is the X-rays incident wavelength, ß is the full width at half maximum intensity (FWHM) of the diffraction peak, θ is the Bragg's diffraction angle, d(hkl) is the interlayer distance between each (hkl) crystalline planes, D is the crystallite particle size and n is the number of layers [171].

XRD was utilized as well to investigate the crystalline structure and phase composition of the electrospun PAN-SGZ nanofibers and to confirm the successful incorporation and dispersion of the nanofillers within the PAN matrix. The nanofibers were examined by the device Bruker/D8 advance with a CuKα radiation (λ=1.54 Å) and the 2θ scanning range was 5-70°.

IV.3.3 Raman spectroscopy

Raman spectroscopy was carried out on a Renishaw inVia dispersive Raman spectrometer equipped with a 532 nm excitation laser. Measurements were performed at room temperature in the range of 250–3500 cm^{-1} to characterize the structural features of the synthesized materials (GO, SGO, and SGO–ZrO_2) nanohybrids. Crystallite size (L_a) can be estimated through the integrated intensity ratio between band D and G (I_D /I_G) and can be expressed (Eq IV.4) as [172]:

$$L_a = 2{,}4 * 10^{-10} \lambda^4 \left(\frac{I_D}{I_G}\right)^{-1} \quad \text{(IV.4)}$$

IV.3.4 X-ray photoelectron spectroscopy (XPS) analyses

XPS was employed to verify the surface functionalization of GO and the successful attachment of nanoparticles. The measurements were conducted on a PHI 5000 VersaProbe spectrometer using Al Kα radiation as the excitation source. The acquired survey spectra were deconvoluted and fitted with Gaussian–Lorentzian functions.

IV.3.5 Thermal analysis (TGA)

This technique involves measuring the mass variation of a sample as a function of time or temperature in order to analyze its thermal decomposition and determine its thermal degradation

(or stability) temperature. The TGA/DTG measurements of GO, SGO and SGO-ZrO_2 were carried out using a TA-SDT Q600 thermal analyzer at a heating rate of 10 °C/min from 25 to 900 °C under a nitrogen atmosphere.

IV.3.6 Zeta potential measurement

The surface charge characteristics and dispersion stability of the colloidal suspensions were evaluated using a Nano Particle SZ-100 analyzer. Measurements were carried out at room temperature on aqueous dispersions of the synthesized materials (GO, SGO, and SGO–ZrO_2 nanohybrids) prepared at a concentration of 0.5 mg/mL, with the applied potential ranging from –200 to +200 mV.

IV.3.7 Differential Scanning Calorimetry (DSC)

DSC analyses allow measuring the difference in heat flow that establishes between a sample and a reference during heating or cooling while maintaining their temperatures equal. The heat flow is directly proportional to the heat capacity of the material in question. If an endothermic or exothermic process occurs during the scan, a variation in the flow is observed, resulting in a peak on the DSC thermogram. It is also used to measure melting temperatures, crystallization, and glass transition temperatures, as well as the degree of crystallinity.

All DSC analyses were performed on a TA Instruments/DSC25 in a dry nitrogen environment. As well as all the samples were placed in tightly sealed aluminum DSC containers and subjected to heating at 350 °C at a continuous rate of 10 °C/min.

IV.3.8 Scanning electron microscope (SEM)

Scanning electron microscopy (SEM) was performed using a Zeiss Gemini 300 instrument to examine the surface morphology of the synthesized materials, including GO, SGO, and SGO–ZrO_2 nanohybrids. The characterization of the morphology of the different nanocomposite fibers was also carried out using SEM (Zeiss/Gemini 300) to provide important information on the quality of dispersion/distribution of the nanofillers within the PAN matrix.

IV.3.9 Viscosity Measurement

viscometer measuring device were employed to measure viscosity at room temperature of the electrospinning solutions PAN in DMF and PAN-SGZ in DMF using a digital rotational viscosimeter PCE-RVI 1.

IV.3.10 Tensile test

The tensile properties were measured using a SHIMADZU-AGS-X machine. The tests were performed at room temperature with a speed of 5 mm/min in accordance with ASTM D882-02 standards (Figure IV.5).

The purpose of these tests is to be able to compare the obtained materials in terms of rigidity and toughness, evaluated respectively by stress, modulus, and strain at break. For each sample, five specimens are tested to verify the reproducibility of the results.

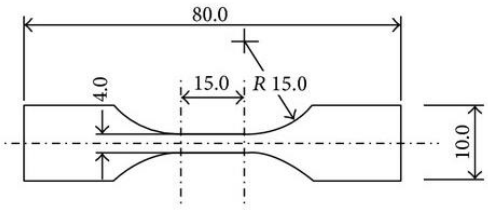

Figure IV.5: Geometry of the tensile test specimen used in this investigation according to ASTM D882-02.

IV.3.11 Electro-mechanical analysis

TENG devices' electrical contacts were connected to an oscilloscope (1102B, GWInstek, New Taipei, Taiwan) and a periodic compress test device were utilized to contact-separation movement between nanofiber surfaces. All electromechanical tests were performed at a frequency of 4.2 Hz. At least two of each nanogenerator (PAN or PAN-SGZ) were produced and electromechanically characterized. (Figure IV.6).

$$Vp-p = Vmax - Vmin \quad \text{(IV.5)}$$

$$Ip-p = Imax - Imin \quad \text{(IV.6)}$$

$$Wp-p = Vp-p \,.\, Ip-p \quad \text{(IV.7)}$$

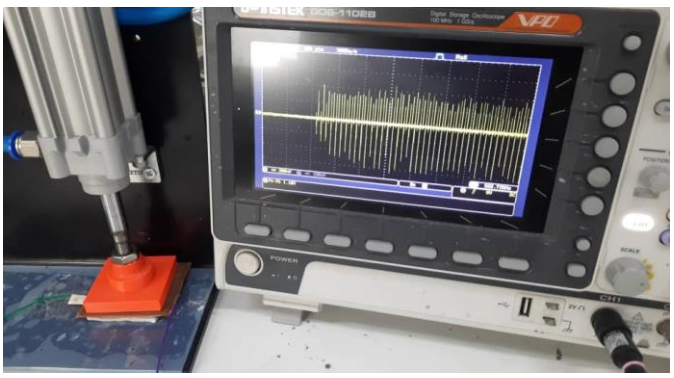

Figure IV.6: Oscilloscope (1102B, GWInstek, New Taipei, Taiwan) and a periodic compress test device.

Chapter V: Results and Discussion

Chapter V: Results and Discussion

Table of content

V.1 Results and Discussion of Synthesized Nanomaterials

V. 1.1 Fourier transform infrared (FTIR) spectroscopy

Figure V.1a presents the results of FTIR spectrum of graphite, GO and ZrO_2. No absorption band was observed in the spectrum of the virgin graphite indicating the inert chemical structure of the latter [173,174]. However, several characteristic bands have been observed in the GO spectrum confirming the successful oxidation of graphite through the presence of various oxygenated functionalities on the basal planes and edges as reported Lerf et al.[61]

The broad band observed in the range of 3671–2981 cm^{-1} corresponds to the elongation vibrations of the hydroxyl (-OH) and carboxyl (-COOH) groups. The characteristic peaks at 1727, 1383, and 1236 cm^{-1} are associated with the elongation vibrations of the carboxyl (C=O), the C–O bonds of the alcohol groups (C-OH), and the C–O bonds of the groups (C-O-C), respectively [175]. The presence of epoxy groups is evidenced by two peaks at 1046 cm^{-1} and 953 cm^{-1}, while the peak at 1596 cm^{-1} is assigned to the C=C stretching of unoxidized sp^2 carbon domains. These findings align with earlier reported studies [174,176]

The spectra of ZrO_2 exhibit a wide band between 3650-2680 cm^{-1}, caused by the vibrations of the hydroxyl group (-OH) associated with the physical absorption of water on the surface of the ZrO_2 nanoparticles [177]. Additionally, the peaks at 473, 572, 668, and 750 cm^{-1} are associated with the characteristic peaks of ZrO_2 [17].

Furthermore, in the FTIR spectrum of SGO (Figure V.1b), four new absorption bands were detected at 1585 cm^{-1}, 1064 cm^{-1}, 770 cm^{-1} and 696 cm^{-1}, attributed to the functional groups N-H, Si-O-Si, Si-OH and Si-O-C, respectively. In addition, the disappearance of the peaks associated with carboxyl (C=O), and epoxy groups suggests that these functionalities reacted with the silane molecules; consequently, the reduction of GO has occurred by covalent functionalization with silane. Moreover, a decrease was seen in the intensity of the hydroxyl (-OH) vibration band and the peaks caused by the vibrations of C-O-C and C-OH. Also, it is noticeable that the N-H bending of primary amine, which is often seen at a wavenumber of 3370 cm^{-1}, may have overlapped with the (-OH) band ranging from 3671-2981 cm^{-1}. The results indicate that the silane AEAPTMS was successfully grafted onto the surface and edges of GO [4,178].

When comparing the FTIR spectrum of SGO and ZrO_2 with SGO-ZrO_2 nanohybrids, a new peak was detected at 906 cm^{-1}, that can be attributed to the vibration of Si-O-Zr and two other peaks were observed at 2995 and 2890 cm^{-1}, which are associated with the asymmetric and

symmetric stretching vibrations of the C–H bond in CH_2 and CH_3 groups, respectively. The hydroxyl, Si-O-C and Si-OH groups have entirely disappeared as well. All these findings indicate that GO nanosheets has been successfully decorated with ZrO2 nanoparticles through covalent bonding with AEAPTMS.[16,89].

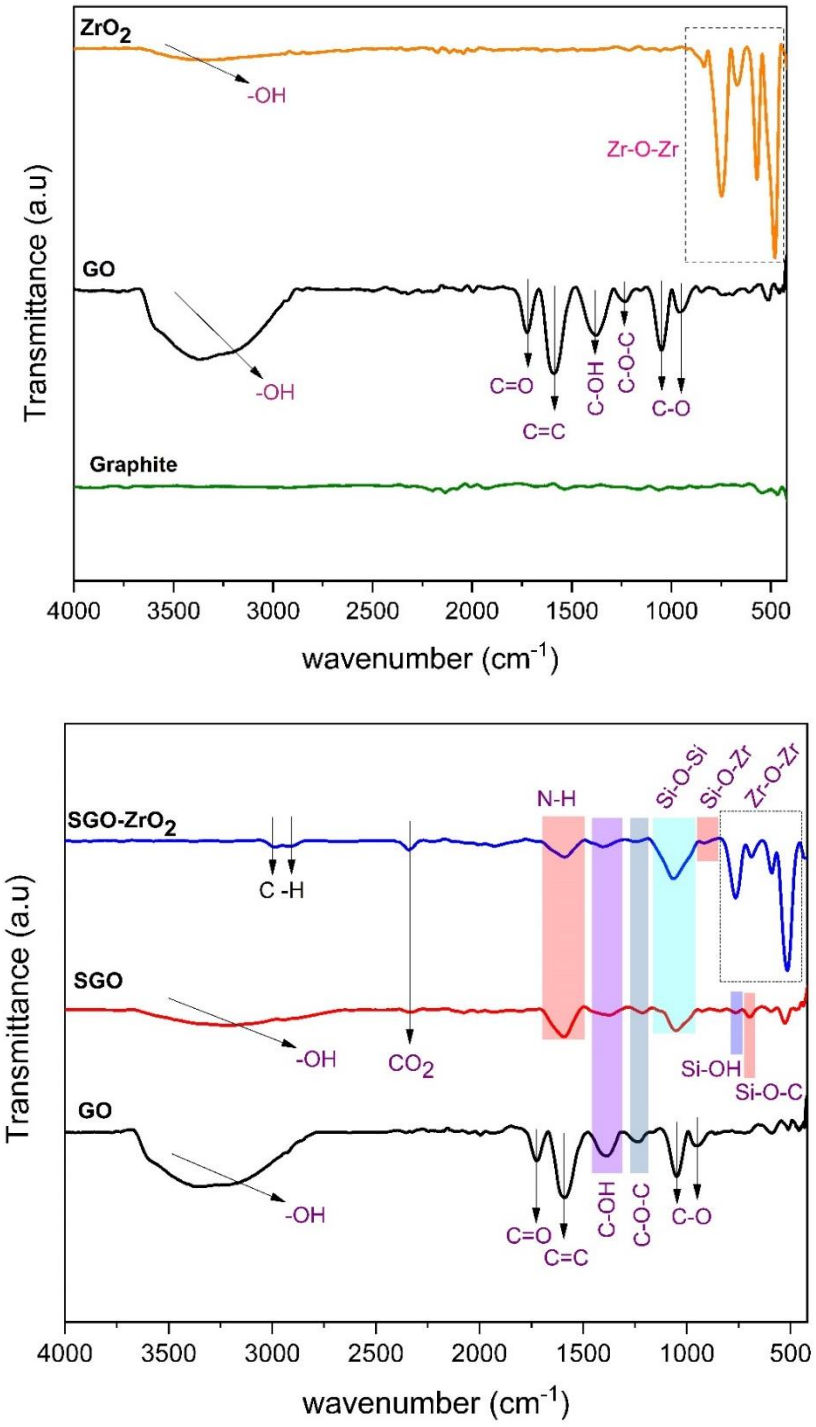

Figure V.1: FTIR spectra of graphite, ZrO_2, GO, SGO and SGO-ZrO_2.

V.1.2 X-ray diffraction (XRD)

The inset figure in Figure V.2 The inset figure in Figure 5 illustrates the pattern of pure graphite powder, emphasizing the distinctive diffraction peak at 2θ = 26.4° associated with the (002) crystalline planes, the interlayer spacing and crystallite size are subsequently measured to be 0.34 nm and 18 nm, respectively. These findings are consistent with the values reported in the literature [179,180].

The GO pattern demonstrates a major shift to a lower 2θ angle of 12.9° associated to the (001) crystalline plane of GO and exhibiting an interlayer spacing of 0.68 nm. The increase of the interlayer is attributed to the existence of oxygen-containing functional groups on the surfaces and edges of each plane, which supports the results obtained by FTIR [181].

Following the silanization process, the SGO pattern exhibited a further shift of the (001) peak to a lower 2θ angle of 9.34°, which corresponds to an interlayer distance of 0.95 nm. The results indicate that the grafting of silane molecules onto GO nanosheet surfaces has been accomplished successfully [5].

The diffraction pattern of the SGO-ZrO_2 nanohybrids indicates the occurrence of ZrO_2 monoclinic peaks at 2θ = 24.4°, 24.8°, 28.4°, 31.7°, 34.4°, 35.7°, 38.8°, 41°, 45.2°, 45.8°, 49.6°, 50.5°, 54.3°, 55.6°, 57.4° according to the JCPDS 37-1484, along with a shift of the (001) peak from 9.34° to 8.75° with an increase in the interlayer distance of 0.6 nm (Table V.1) [16,182,183].

Table V.1: Interlayer spacing and crystalline size values of graphite, GO, SGO and SGO-ZrO_2.

Samples	Graphite	GO	SGO	SGO-ZrO_2
Interlayer distance d (nm)	0.34	0.68	0.95	1.01
Crystallite particles size D (nm)	18	7.8	4.9	2.8
Number of layers n	54	12	6	4

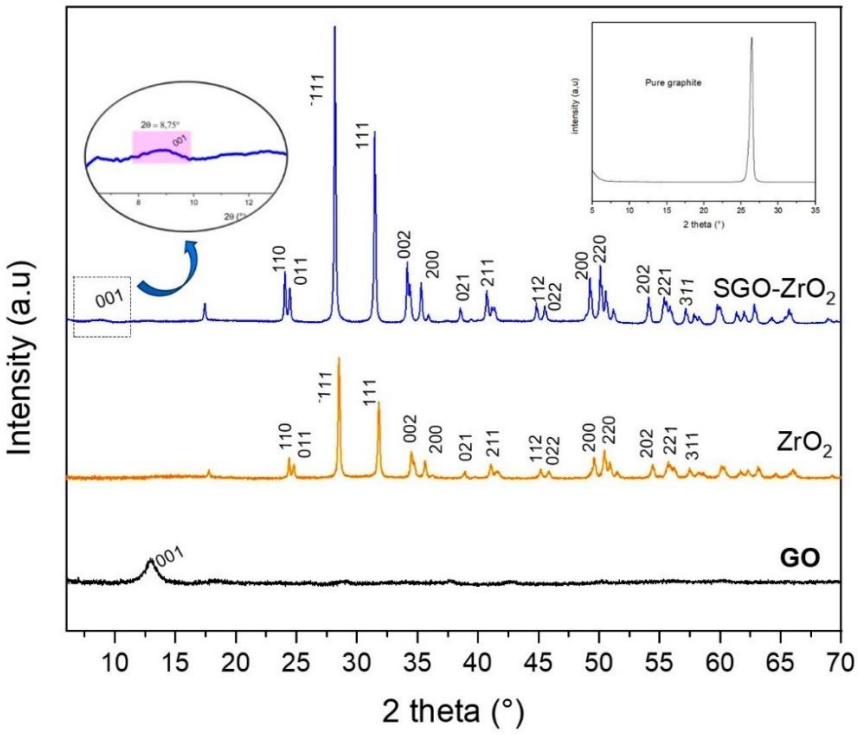

Figure V.2: XRD pattern of GO, ZrO_2, SGO and SGO-ZrO_2.

V.1.3 Raman spectroscopy

Figure V.3 illustrates the Raman spectrum of GO, SGO and SGO-ZrO_2, each spectrum exhibits two intense peaks which correspond to the G and D bands, these characteristics bands are frequently observed in graphite-based materials. The G band is relative to the sp^2 carbon vibrations of the aromatic cycle, providing evidence for the graphitic structure of the observed material. The D band refers to the presence of sp^3 carbon atoms as a result of disorders and structural defects [184,185].

Furthermore, I_D/I_G ratio increased for SGO and SGO-ZrO_2 nanohybrids compared to the GO ratio (Table V.2). This indicates the conversion of the sp^2 carbon hybrid to sp^3 carbon hybrid, resulting in a rise in the number of defects [79,186].The slight shift of G band towards higher wavenumbers confirms the covalent grafting of AEAPTMS on GO surface. Which often leads to the isolation of sp^2 carbon atoms [187,188].

Table V.2: Raman Characteristics for GO, SGO and SGO-ZrO_2.

Samples	G band (cm^{-1})	D band (cm^{-1})	I_D/I_G	L_a (nm)
GO	1591	1353	0.91	21
SGO	1594	1349	1.05	18.3
SGO-ZrO_2	1596	1349	0.98	19.6

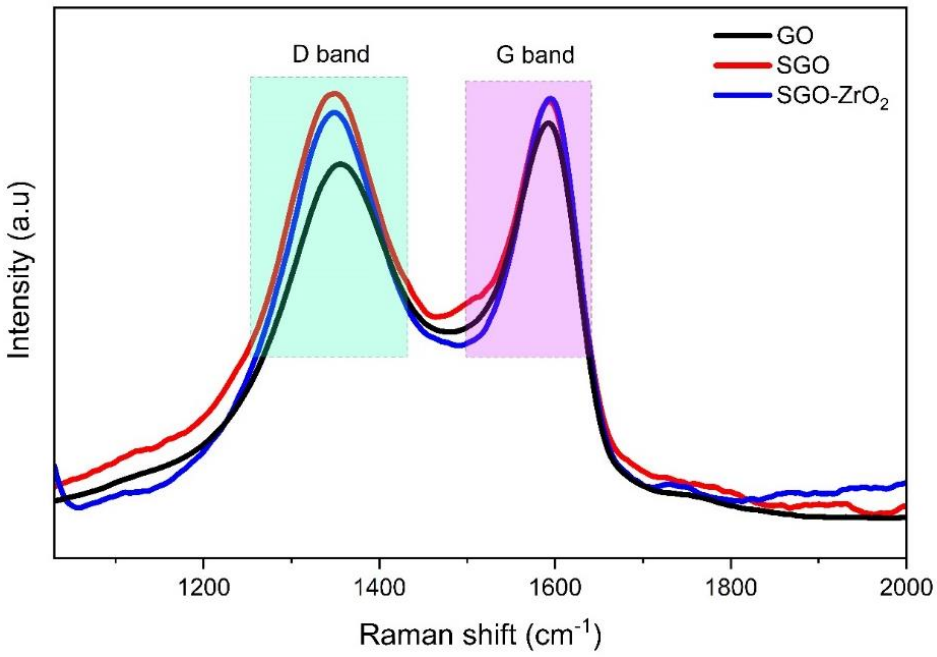

Figure V.3: Raman spectra of GO, SGO and SGO-ZrO_2.

V.1.4 X-Ray photoelectron spectroscopy (XPS)

Figure V. 4 presents the data acquired from the XPS survey scans of GO, SGO, and SGO-ZrO_2 samples. The XPS survey scan of GO displays distinct peaks corresponding to C1s and O1s. Furthermore, the detection of N1s and Si2p peaks in the SGO survey scan, confirms the successful grafting process of silane AEAPTMS on the surface of GO. In addition, to the existence of the peaks C1s, O1s, N1s and Si2p, SGO-ZrO_2 survey scan shows the occurrence of a Zr3d peak, indicating that the surface of GO has been modified with ZrO_2 nanoparticles. The fitted signals are shown in Figure V.5. The C1s peak of GO can be fitted to three components located at 284.1, 286.02, and 287.2 eV, attributed to the C-C, C-O, and C=O species, respectively. Which validate the effective oxidation of graphite relying on Hummer's modified method [189,190].

Analysis of the higher resolution C1s spectrum of SGO-ZrO_2, revealed the formation of a new peak at 285.8 eV, referring to the presence of a C-N bond. Besides, the intensity of the C-O

peak which represents carbons in functional groups such as hydroxyl and epoxy was decreased. Yang et al.[9] proposed that this decrease in intensity could be attributed to a reaction between the amine groups of silane molecules and the epoxy groups on the surface of graphene oxide [191]. The O1s spectrum was divided into Zr-O-Zr (529.33 eV), O-C=O (530.79 eV), Si-O-Si/Si-O-Zr (531.52 eV), C-OH/Si-O-C (532.36 eV) [178,192]. Additionally, deconvolution of the high resolution N1s spectrum of the nanohybrids reveals two peaks. The interaction between the epoxy groups of GO and the primary amines of AEAPTMS results in a peak at 399 eV, credited to secondary amine bonds. The second peak at 402.05 eV corresponds to protonated primary amines, demonstrating that certain AEAPTMS amines did not react and retained their original form as primary amines [193–195]. The Si2p spectrum represents the Si-O-C at 100.63 eV and Si-O-Si/Si-O-Zr at 101.45 eV [196].

Finally, the Zr3d spectrum is separated into two distinct components: Zr3d5/2 and Zr3d3/2. The components relate to Zr-O-Zr and Zr-O-Si interactions, exhibiting energy levels of 182.12 eV and 184.45 eV, respectively [14,197,198]. The obtained results correlate well with the FTIR data (Figure V.6).

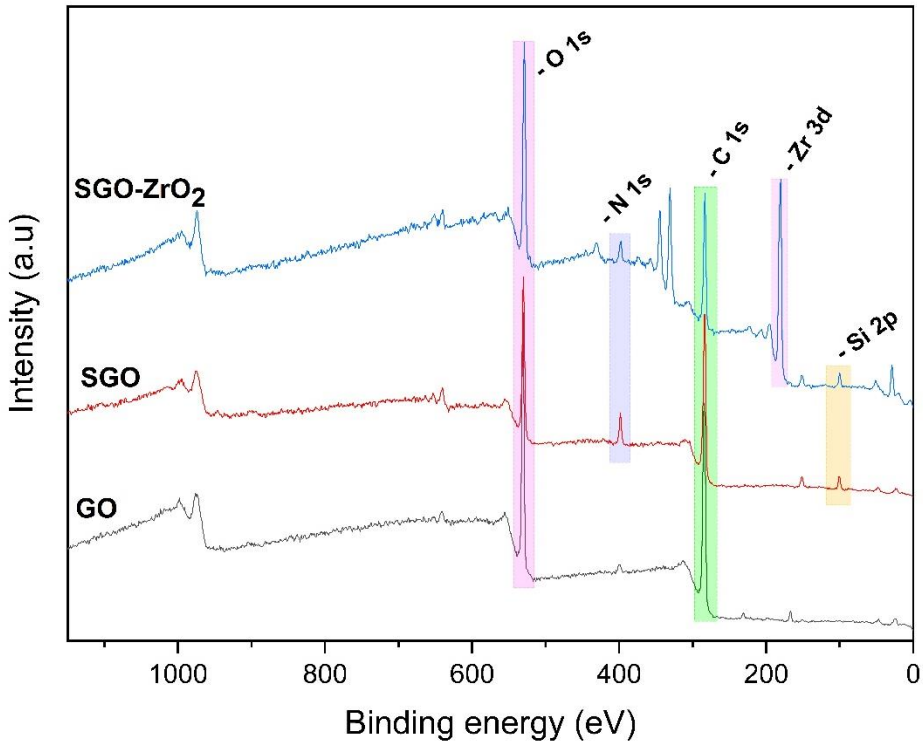

Figure V.4: XPS survey spectrum of GO, SGO, SGO-ZrO_2 nanohybrids.

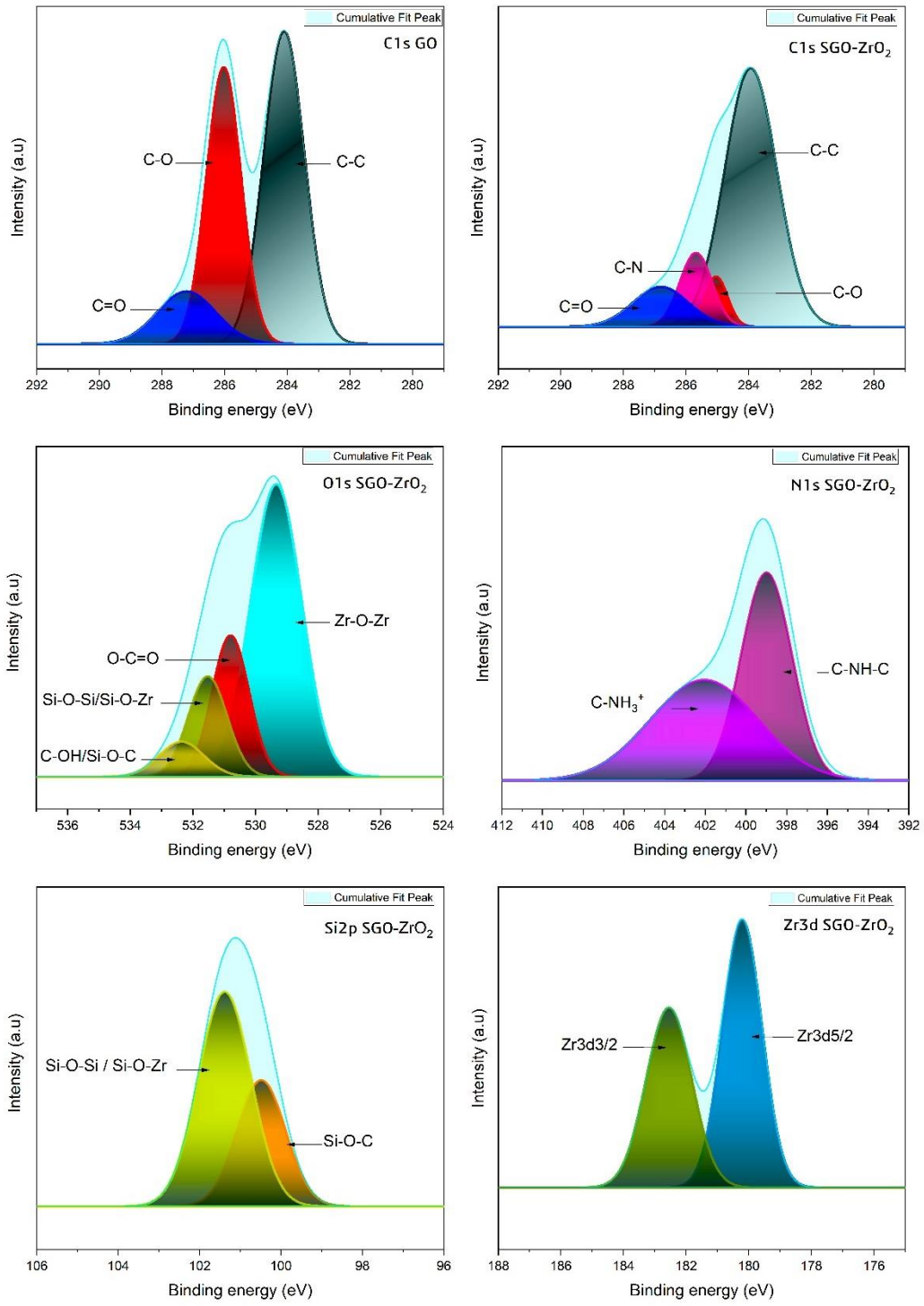

Figure V.5: XPS high resolution spectrum of SGO-ZrO_2 nanohybrids.

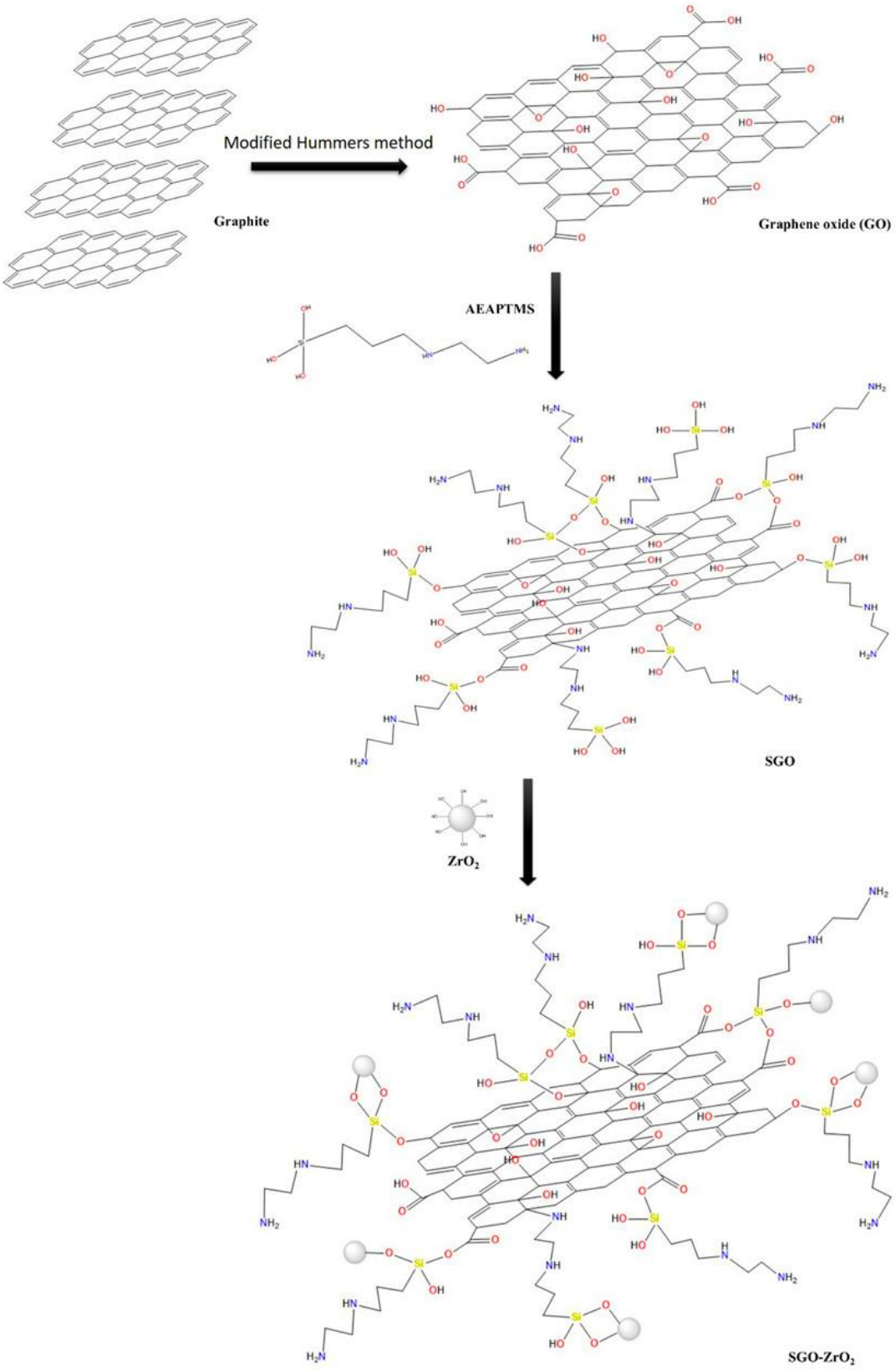

Figure V.6: Schematic illustration of the silanization of GO and its decoration with ZrO_2 nanoparticles.

V.1.5 Thermogravimetric Analysis (TGA)

TGA measurements were performed to assess the thermal resistance of the prepared materials and to monitor their mass reduction over different temperature intervals. Figure V.7 presents the thermograms of GO, SGO and SGO-ZrO_2 nanohybrids.

Thermogram of GO reveals three main stages of weight loss. The initial decrease, occurring between 20 °C and 100 °C (about 18%), is attributed to the evaporation of physically adsorbed water. The second stage, from 140 °C to 280 °C with nearly 30% mass loss, is related to the decomposition of oxygenated groups (hydroxyl, carboxyl, and epoxy) attached to the nanosheet edges and surfaces. A third stage, observed as a broad DTG peak starts from 490 °C, is associated with the gradual pyrolytic decomposition of the basal plane. At 800 °C, 20% of the material remained, showing that most of the GO had decomposed, confirming that GO is thermally unstable. [79,199].

However, thermogram of SGO shows a different behavior and an enhanced thermal stability across the whole temperature range. Its decomposition also proceeds in three steps. The first weight reduction, about 9%, occurs between 45 °C and 120 °C. The second step, taking place from 130 °C to 228 °C, with a weight loss of 12%. It can be noticed that the weight loss has decreased in the first and the second loss steps compared to GO which can be explained by the increased hydrophobicity of the modified sheets and the lower content of oxygen functionalities after reaction with silane. The third stage, extending from 250 °C to 570 °C, appears as a broad DTG peak attributed to the pyrolytic decomposition of the siloxane network formed during functionalization. At 800 °C, the remaining mass is about 58%, this could be attributed to the attachment of silane to the GO surface, resulting in an enhanced thermal stability of GO nanosheets [80,188].

Decorating the surface of the SGO with ZrO_2 nanoparticles further improves its thermal resistance compared to pristine GO. This is evidenced by a three-step weight loss, the first two stages occurring within the same temperature intervals as those of SGO but showing much smaller weight losses of about 4% and 6%, respectively. Notably, the residual weight loss is about 81% at 800 °C, highlighting the strong stabilizing effect of ZrO_2 on the silanized SGO nanosheets [90,200].

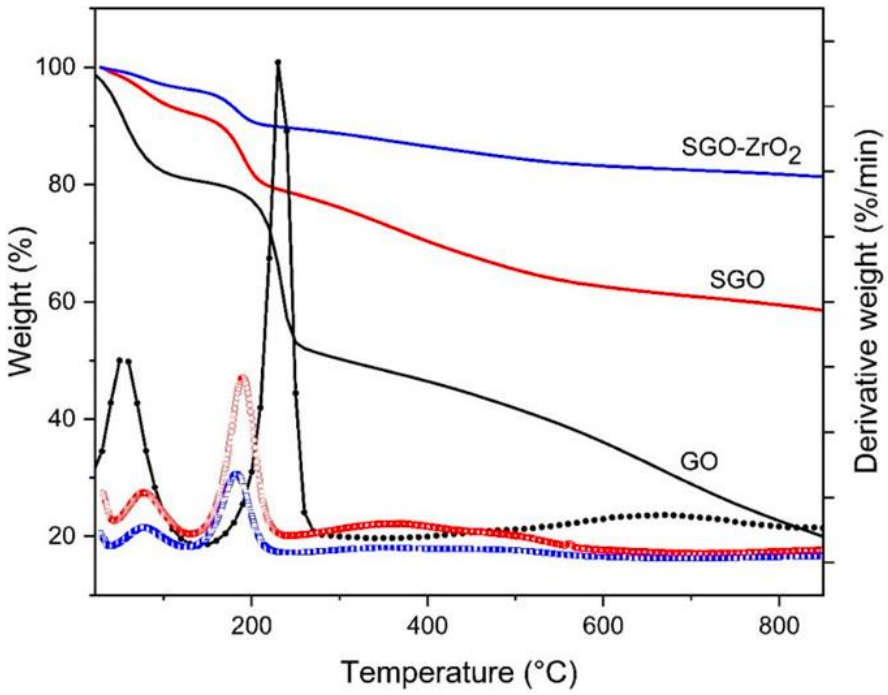

Figure V.7: TGA and DTG of GO, SGO and SGO-ZrO_2.

V.1.6 Zeta Potential measurements

Zeta potential measurements were employed to evaluate both the surface charge and the colloidal stability of graphene nanomaterial suspensions and their derivatives in aqueous solutions [201,202].

The zeta potential of GO nanosheets is approximately –42.2 mV, reflecting a highly negative charge. This strong negative potential indicates that GO remains well-dispersed in aqueous media, mainly due to the ionization of its carboxyl groups ($–COO^-$), which confer excellent suspension stability. In the case of SGO, the potential shifts to –27.8 mV. This reduction in negativity can be explained by the partial removal of oxygenated groups from the GO surface as well as the introduction of protonated amine groups ($–NH_3^+$) after silane modification [194]. However, the zeta potential values of SGO-ZrO_2 nanohybrids exhibit a notable shift to a positive zeta potential of about +5.8 mV. This reversal in surface charge can be attributed to the combined contribution of protonated amine groups ($–NH_3^+$) and zirconium cations (Zr^{4+}) present on the hybrid structure. Such values suggest that, unlike GO, both SGO and SGO–ZrO_2 display limited colloidal stability in aqueous media (Figure V.8) [203].

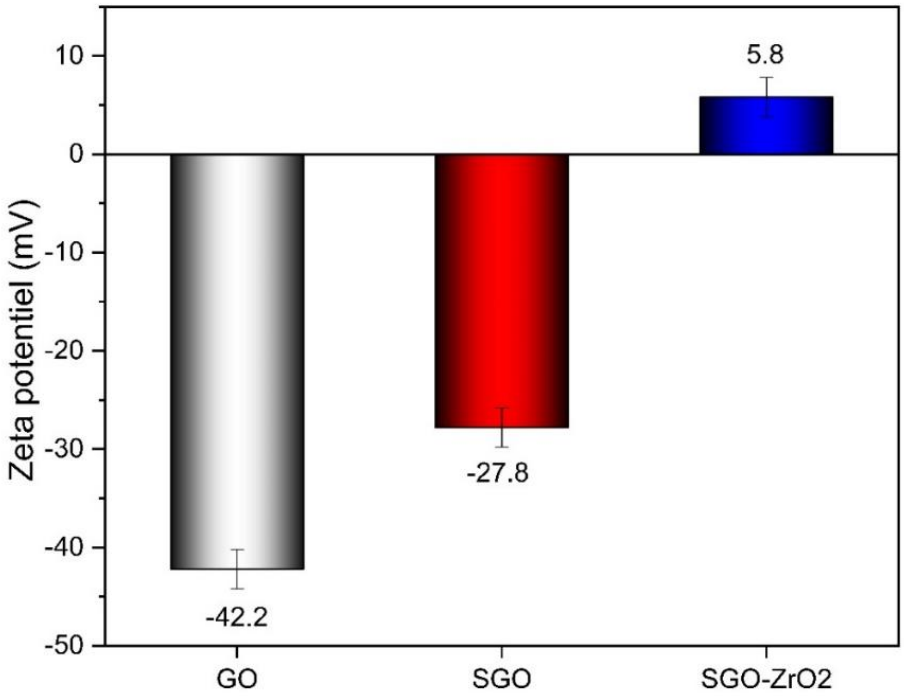

Figure V.8: Zeta potential measurements of GO, SGO and SGO-ZrO_2 nanohybrids.

V.1.7 Scanning electron microscope (SEM)

SEM analysis was employed to observe the morphological features of GO before and after modification with silane and ZrO_2.

As shown in Figures V.9a-b, the unmodified GO displays a layered structure and relatively smooth surface, accompanied by its characteristic wavy wrinkles [204]. The introduction of organosilane (AEAPTMS) onto the GO surface led to noticeable morphological modifications when compared with the pristine material given in Figures V.9c-d; the multilayered detachment provides clear evidence of successful GO silanization and aligns well with the findings obtained from XRD analysis. [10,79]. The images obtained from the SEM (Figure V.9e-f) of the generated nanohybrids SGO-ZrO_2 demonstrate that ZrO_2 nanoparticles are effectively grafted onto the GO layers, along with localized regions of nanoparticle agglomeration [14].

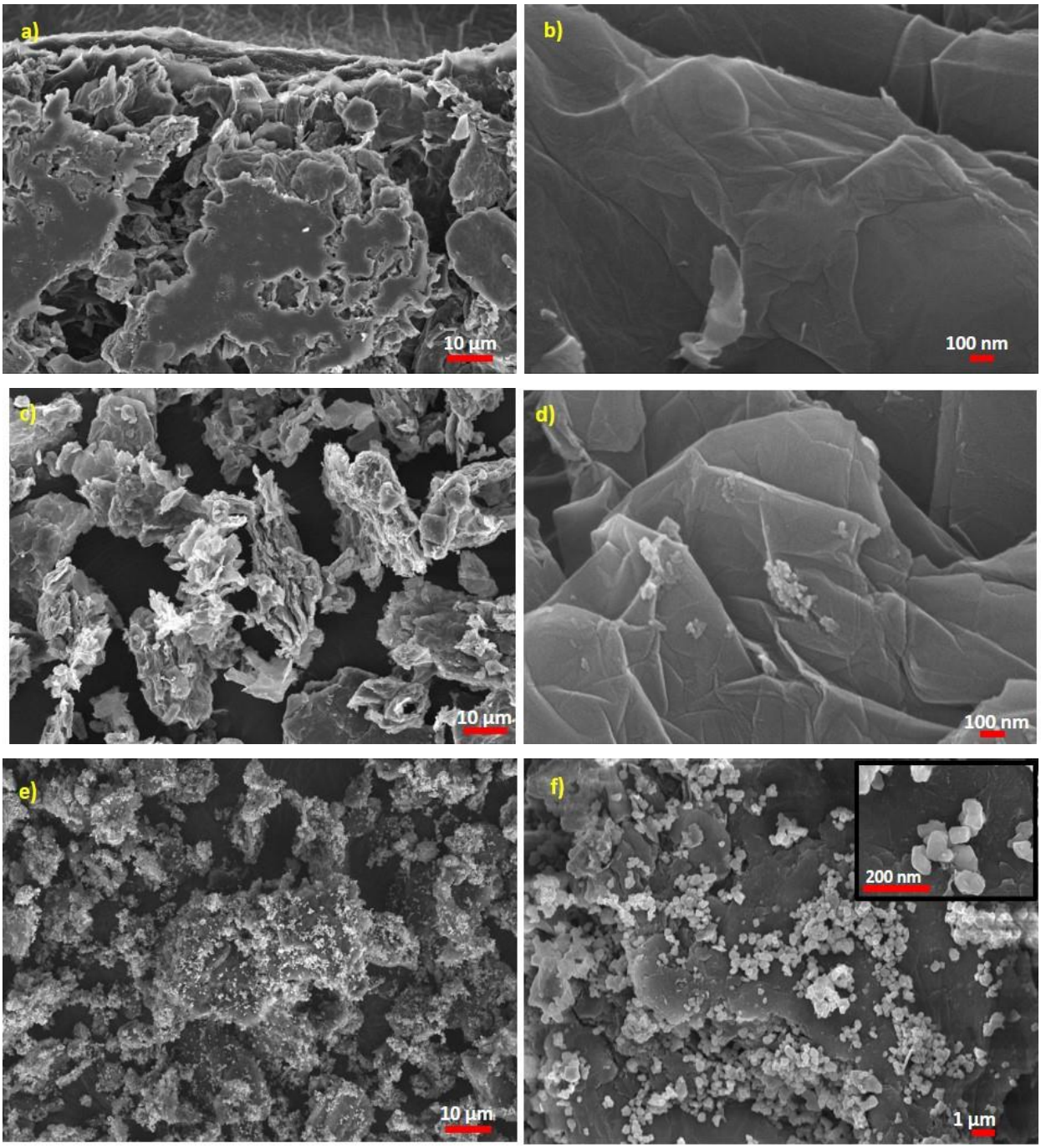

FigureV.9: SEM images of GO, SGO and SGO-ZrO_2 nanohybrids.

V.2 Results and Discussion of Nanofibers Characterization

V.2.1 Scanning electron microscope (SEM)

The SEM images of PAN and PAN-SGZ nanofibers with varying SGZ doping (0.25, 0.5, 1, and 2 wt%) are shown in Figure V.10. It is evident that neat PAN and PAN-SGZ nanofibers were successfully fabricated through the electrospinning process.

The SEM images revealed as well that pure PAN nanofibers exhibited a smooth surface, while the PAN-SGZ fibers displayed a rougher morphology. As can be seen in Figures V.10 (b, c and d) when the SGZ content was 0.25%, 0.5%, or 1%, the nanofillers appeared to be well-dispersed within the PAN matrix, resulting in uniform, bead-free nanofibers. However, at a doping of 2%, bead formation is observed in the nanofibers (Figure V.10 (e)).

The average diameter of the electrospun nanofibers was evaluated from SEM images using ImageJ software. The results indicate that the average diameter of neat PAN nanofibers was 220 nm. With the incorporation of SGZ nanohybrids, the fiber diameter gradually decreased to 203 nm, 173 nm, and 167 nm at SGZ concentrations of 0.25%, 0.5%, and 1%, respectively. Nevertheless, at a doping level of 2%, the diameter increased again to 218 nm.

In general, additives tend to increase fiber diameter due to the higher concentration of solid content in the solution. This increase can promote the formation of thicker fibers. At the same time, additives may also enhance the net charge density of the solution, promoting greater stretching and thus thinner fiber formation. The final fiber diameter depends on which of these opposing effects dominates [205,206].

In this study, the incorporation of SGZ led to a similar behavior. As the amount of SGZ increased, the fiber diameter decreased, suggesting that conductivity had a stronger influence than viscosity. Even though the solutions became more viscous with the incorporation of the nanofillers (241.76 cp for neat PAN and 248.10, 260, 288.37, 295.40 cp at a doping of 0.25, 0.5, 1, and 2 wt% respectively), the enhancement of the solution conductivity played a more dominant role, resulting in increased stretching of the electrospinning jet and the formation of thinner fibers [207]. Additionally, similar trend was reported by Abdel-Mottaleb et al.[114] who observed a decrease in fiber diameter when GO was incorporated into PAN matrix. Suggesting that the noticeable decrease in fiber diameter can be attributed to the increased electrical conductivity, and thermal conductivity, all of which play a crucial role in fiber formation. A more conductive solution enhances the stretching of the polymer jet during electrospinning, facilitating the production of fibers with small diameters [208,209].

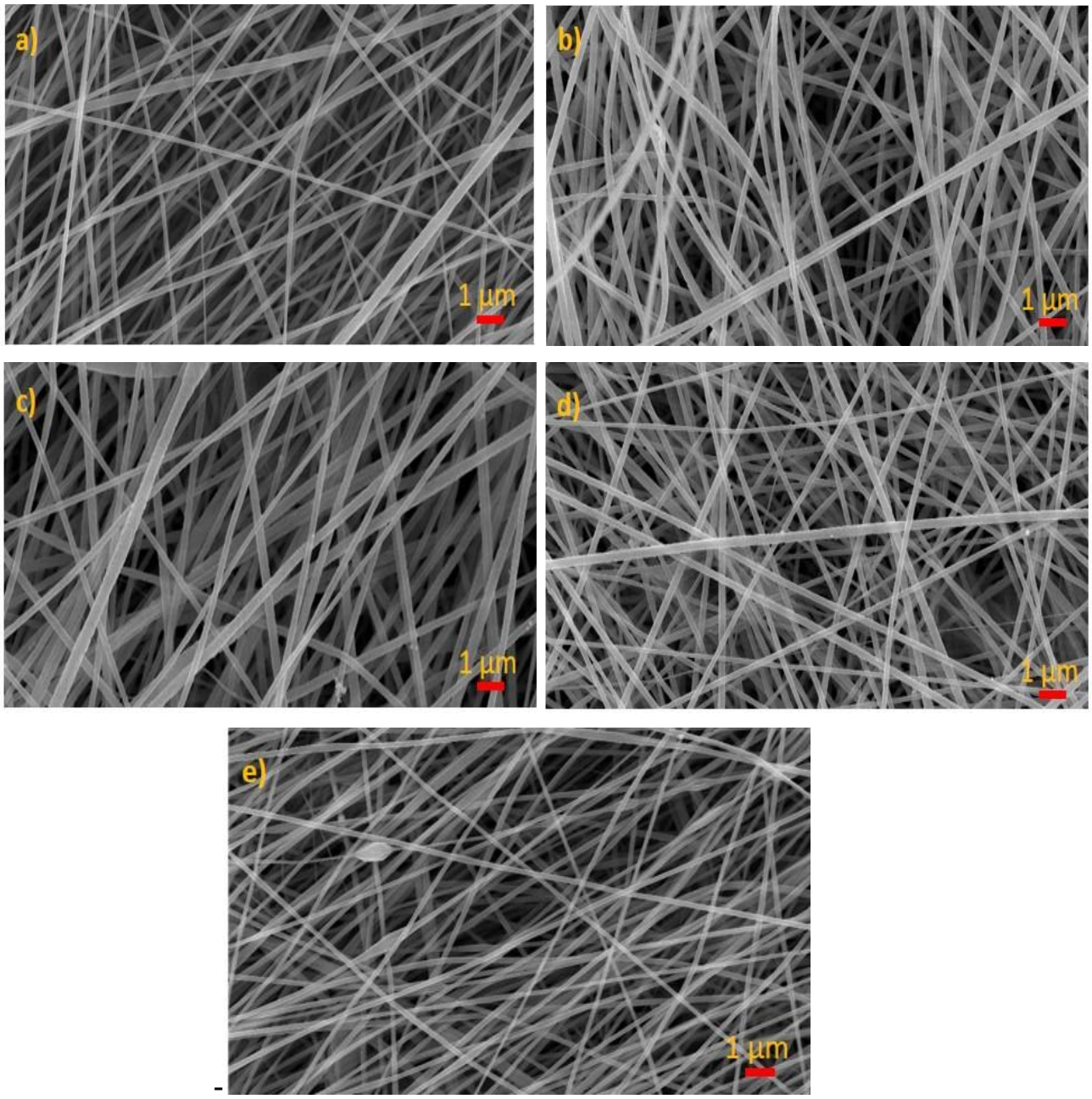

Figure V.10: SEM images of (a) neat PAN nanofibers, (b) PAN-0.25SGZ nanofibers, (c) PAN-0.5SGZ nanofibers, (d) PAN-1SGZ nanofibers, and (e) PAN-2SGZ nanofibers.

V.2.2 Fourier transform infrared (FTIR) spectroscopy

FTIR analyze was conducted to investigate the interactions between the nanofillers SGZ and the PAN matrix. The figure V.11 illustrates the acquired results; the spectrum of both neat PAN and PAN-SGZ nanofibers were notably analogous, displaying several characteristic peaks; at 2240 cm^{-1} assigned to the stretching vibration of nitrile groups (-C≡N), the peaks at 2929 cm^{-1}, 1447 cm^{-1}, 1366 cm^{-1} and 1240 cm^{-1} are associated with the bending vibration of aliphatic CH groups (CH and CH_2) respectively, all of these peaks represent the fundamental groups forming the backbone chain of the PAN [100,210].

Nevertheless, in the spectrum of PAN-SGZ nanofibers, the intensity of the -C≡N peak gradually decreased, while a new absorption peak appeared at 1541 cm^{-1}, attributed to the -NH stretching vibration resulting from the amination reaction between the nitrile groups of PAN and the amine groups of the silane molecules in the nanofillers. This finding confirms the successful incorporation of SGZ nanofillers into the nanofibers [211].

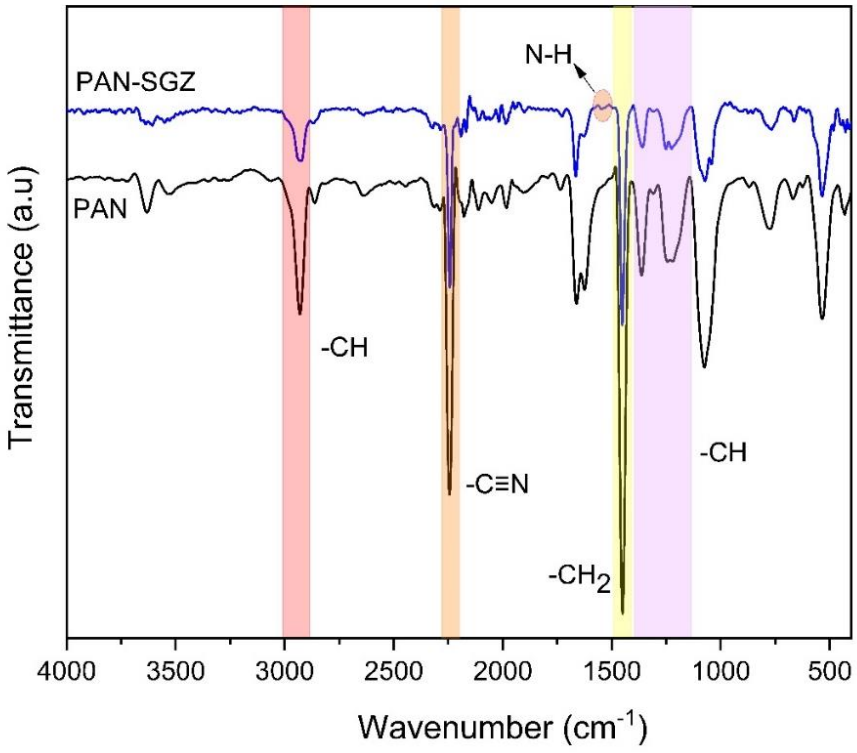

Figure V.11: FTIR spectrum of PAN and PAN-SGZ nanofibers.

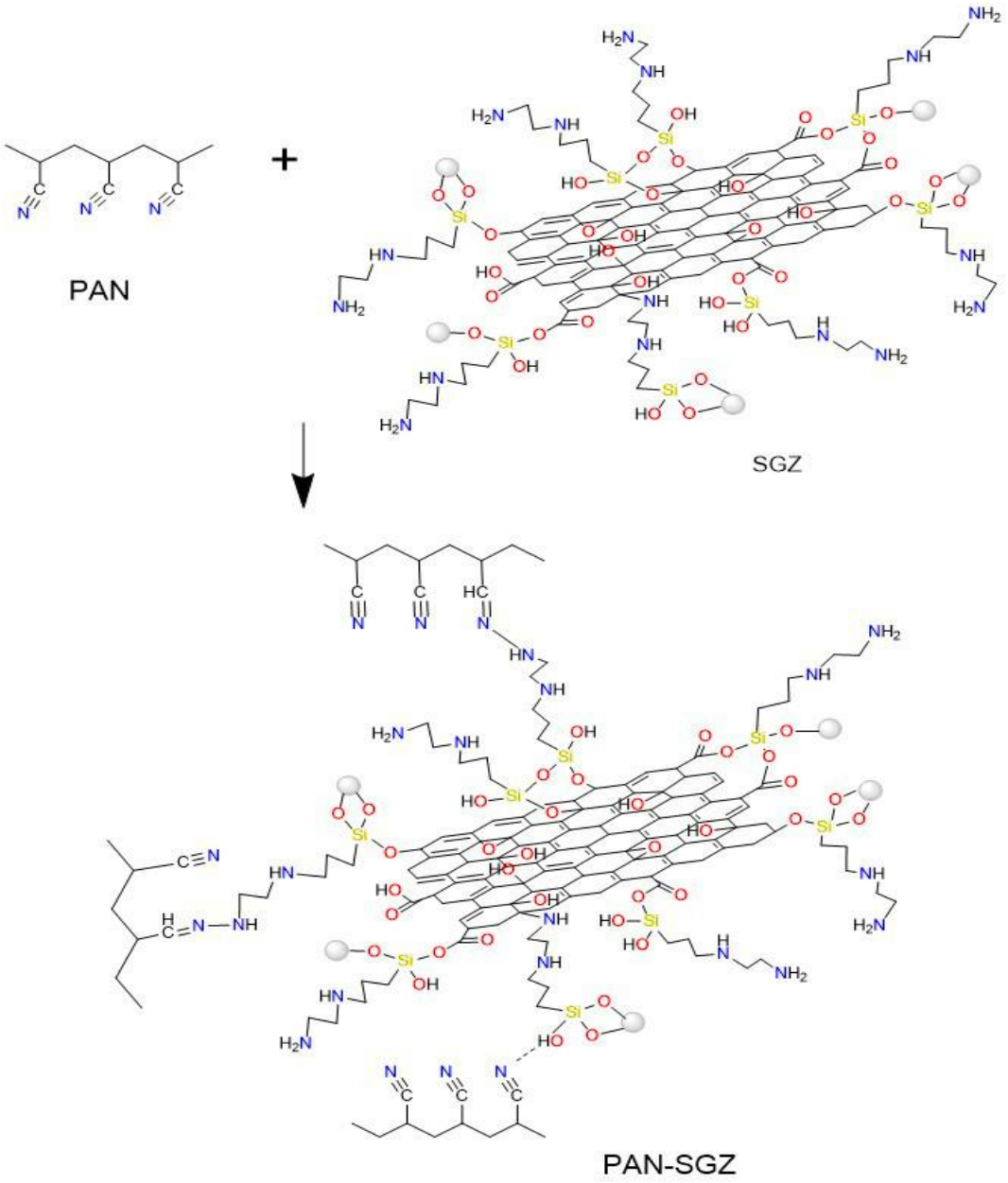

Figure V.12: Schematic illustration of the reaction between PAN and SGZ nanofillers.

V.2.3 X-ray diffraction (XRD)

Figure V.13 illustrates the XRD patterns of PAN and PAN-SGZ nanofibers. Each pattern displays a significant diffraction peak at 16.6° and a less intense peak at 28.5°, corresponding to the (100) and (110) crystallographic planes of PAN, respectively [212]. Furthermore, the XRD patterns of the PAN-SGZ nanofibers exhibit distinct peaks corresponding to ZrO_2 at doping levels of 0.5%, 1%, and 2%, confirming the successful incorporation of the nanofiller into the PAN matrix.

In addition, to evaluate the influence of SGZ nanofiller on PAN structure, the degree of crystallinity (X_c) was assessed using Hinrichsen's method [213]. Table V.3 presents the

summarized values of the degree of crystallinity. The results indicate that the degree of crystallinity exhibited a linear increase as the loading of SGZ nanofillers remained below 2%. This enhancement is primarily attributed to the increased conductivity of the electrospinning solutions induced by the conductive additives. Higher solution conductivity during electrospinning is known to promote greater stretching of the jet, thereby improving the alignment of molecular chains [214,215]. Furthermore, the additives may promote a more linear configuration of PAN chains, thus increasing their degree of orientation [209]. Interactions between PAN and SGZ nanofillers also appear to facilitate crystallization after the dissolution and electrospinning processes.

At 2% doping, a slight reduction in crystallinity is observed compared to the 0.25%, 0.5%, and 1% doping levels, although it still remains higher than that of pure PAN. This may be due to excessive interactions among the molecular chains, which restrict their mobility thus hindering the enhancement of crystallinity [216]. This observation is consistent with the findings of Zhang et al.[212] who reported a similar change in the degree of crystallinity in PAN nanofibers incorporated with GO nanosheets.

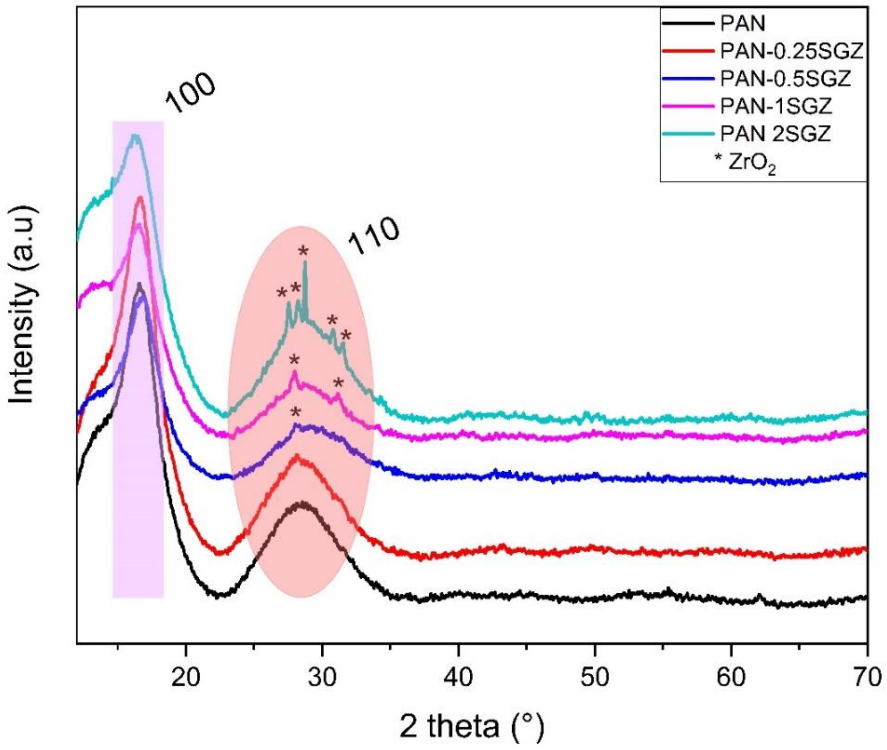

Figure V.13: XRD patterns of neat PAN nanofibers and PAN-SGZ with varying SGZ doping (0.25, 0.5, 1, and 2 %).

V.2.4 Differential Scanning Calorimetry (DSC)

The thermal behavior of pure PAN and PAN-SGZ nanofibers was analyzed by DSC. Thermograms are presented in the Figure V.14, and Table V.3 shows the relative parameters obtained from the DSC curves: the cyclization temperature (T_c) and the enthalpy (ΔH_c) associated with the exothermic peak. The heat of the exothermic peak indicates the total heat of the thermal reactions taking place during the collection of DSC thermograms.

It is well established that PAN undergoes an exothermic cyclization process when heated, initiated primarily by free-radical mechanisms. Through intra- or intermolecular radical transfer, the nitrile groups transform the linear PAN chains into a thermally stable, aromatic ladder structure [217,218].

In the present study, the DSC analysis of pure PAN nanofibers shows a sharp exothermic peak around 298.5 °C, results from a combination of three main reactions, mainly dehydrogenation, cyclization, and crosslinking reactions, which are known to be mainly exothermic in nature [219]. Among these three thermal reactions, the predominant one is known to be the cyclization reaction. The sharp peak of pure PAN indicates a rapid cyclization of nitrile groups into an extended conjugated structure under a nitrogen atmosphere, which may be attributed to the facile formation of free radicals on the nitrile groups and subsequent recombination between the radical groups intermolecularly or intramolecularly [220,221].

Upon incorporation of SGZ nanofillers into PAN matrix, the exothermic peak shifts to higher temperatures with increasing SGZ content, however, at 1% of SGZ the T_c deviated from the expected trend, possibly due to instrumental or procedural error. This needs further investigation. The shift of T_c to higher temperatures comparing to neat PAN may be attributed to the inhibiting effect of the nanofillers. As a result, it can be concluded from the above discussion that the recombination reactions between the radicals are hindered by the incorporation of the SGZ nanofillers [209]. Furthermore, the increase in cyclization temperature can also be attributed to the improved thermal stability provided by the SGZ nanofillers, which leads to cyclization reactions occurring at a higher temperature. The increased crystallinity observed in XRD further supports this behavior, as a more ordered structure may enhance thermal stability. Sharma et al.[125] have reported similar observations, suggesting that the shift of the exothermic peak to higher temperatures may be due to the stabilizing effect of ZrO_2 on PAN nanofibers.

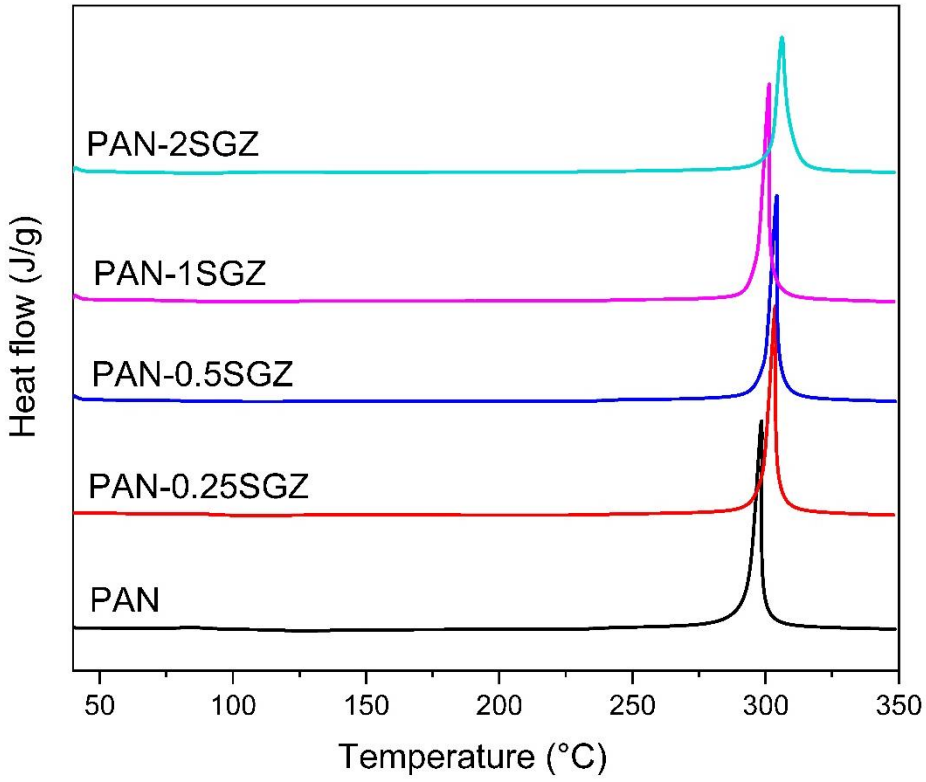

Figure V.14: DSC thermograms of neat PAN nanofibers and PAN-SGZ with varying SGZ doping (0.25, 0.5, 1, and 2 %).

Table V.3: The T_c and ΔH_c from DSC results and crystallinity values obtained from XRD.

Samples	DSC		XRD
	T_c (°C)	ΔH_c (J/g)	X_c (%)
PAN	298.5	390.8	35
PAN 0.25SGZ	302.5	367.23	40
PAN 0.5SGZ	303.67	367.10	47
PAN 1SGZ	304.24	351.53	51
PAN 2SGZ	306.16	332.38	44

V.2.5 Mechanical properties

The tensile properties of PAN and PAN-SGZ nanofibers were evaluated and compared. The stress-strain curves and tensile strength are shown in Figure V.15, while Table V.4 provides average values and statistical errors for tensile strength, elastic modulus, and elongation at break.

The results clearly demonstrate that the addition of SGZ nanofillers to the PAN matrix has a great influence on the mechanical properties leading to an increase in the tensile strength and Young's modulus. Specifically, at small load of 0.25 wt% SGZ, the tensile strength increased from 2.5 MPa to 3 MPa, and the Young's modulus enhanced as well from 113 MPa to 152.1 MPa. As the SGZ content increased, both tensile strength and Young's modulus presented further improvement, emphasizing the reinforcing impact of the nanofillers on the mechanical properties of the nanofibers (Figure V.16).

In comparison with pure PAN, the composite nanofibers exhibited higher tensile strength and modulus, it was found that the tensile strength and Young's modulus of composite nanofibers were enhanced when the amounts of SGZ were increased. This enhancement may be attributed to both better interactions between SGZ and the PAN matrix and an increase in the crystallinity of the nanofibers, as confirmed by XRD analysis. The uniformly dispersed SGZ nanofillers promoted a more ordered arrangement of the PAN molecular chains, which contributed to the observed improvements in mechanical strength and stiffness. However, at a higher SGZ loading of 2 wt%, the nanofibers appeared to have a little lower stress, which might be due to the aggregation of SGZ nanofillers [222].

These findings are consistent with the study conducted by Abdel-Mottaleb et al.[114] who fabricated PAN-GO nanofibers and observed a significant enhancement in their mechanical properties. Their tensile testing results demonstrated that incorporating GO as a filler effectively reinforced the PAN nanofibers. Precisely, at a GO content of 1 wt%, the nanofiber exhibited a 64.4% increase in tensile strength and a 71.4% improvement in Young's modulus.

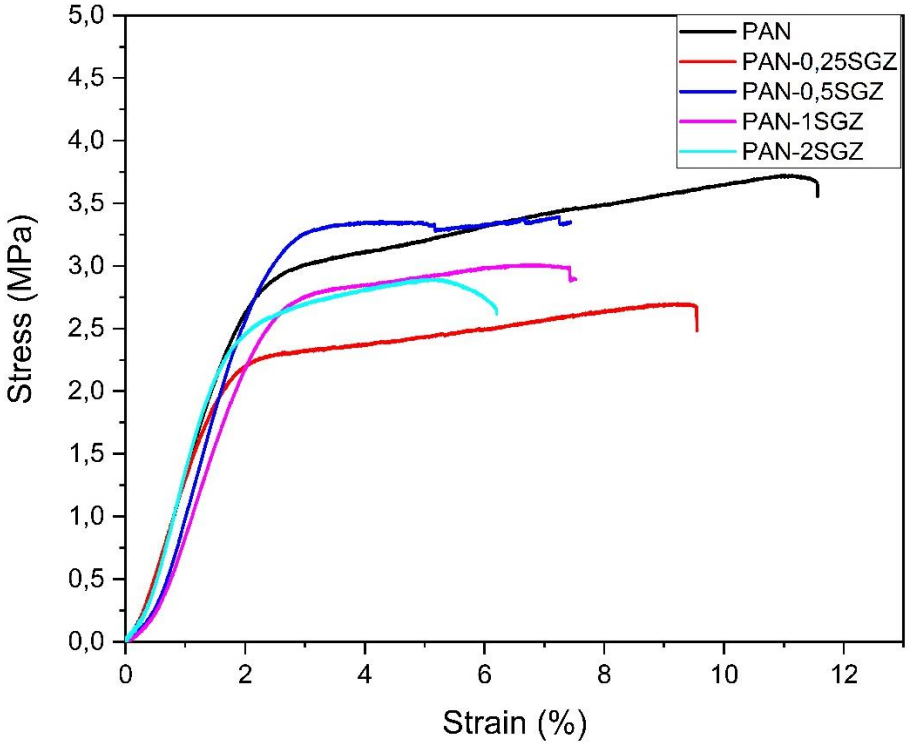

Figure V.15: Stress-strain curves of neat PAN and PAN-SGZ nanofibers with varying SGZ doping (0.25, 0.5, 1, and 2 %).

Table V.4: Tensile strength, Young's modulus, and elongation at break of PAN and PAN-SGZ nanofibers.

Samples	Young's modulus (MPa)	Tensile strength (MPa)	Elongation at break (%)
PAN	102 ± 4.01	2.4 ± 0.59	10.8 ± 2.7
PAN-0.25SGZ	151.9 ± 0.29	2.7 ± 0.03	8.2 ± 2.6
PAN-0.5SGZ	156.4 ± 4.09	3.6 ± 0.04	8.3 ± 0.1
PAN-1SGZ	163.8 ± 4	3.2 ± 0.3	6.93 ± 2.2
PAN-2SGZ	177.7 ± 4.5	2.98 ± 0.08	5.3 ± 1.02

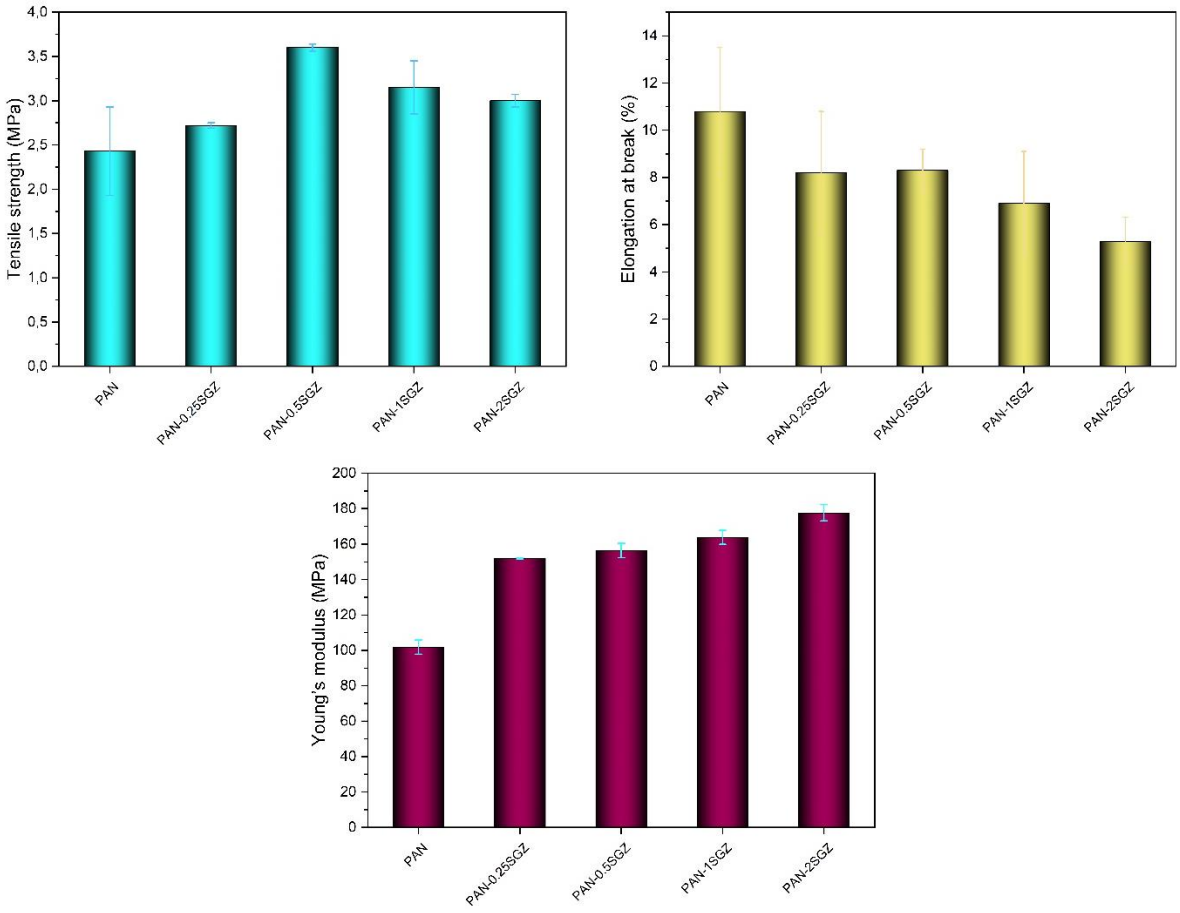

Figure V.16: Tensile strength (a), elongation at break (b), young's modulus of specimens (c).

V.2.6 Electro-mechanical analysis

Electrospun nanofibrous mats incorporating varying concentrations of PAN–SGZ (ranging from 0.25 to 2 wt.%) were fabricated and employed as tribopositive layers, while a neat PAN nanofibrous mat was used as the tribonegative layer in the TENG devices. Additionally, a reference TENG consisting of neat PAN-to-PAN nanofibrous mats was fabricated and characterized. Although using identical polymers as both tribo-layers is not ideal for achieving high output performance, this configuration allows for an isolated evaluation of the influence of SGZ nanofillers on the triboelectrification process.

The electrical output performance of the TENG devices is summarized in Figure V.17. The reference PAN–PAN TENG exhibited a peak-to-peak voltage of 0.6 V and a peak current of 0.67 µA. Incorporating SGZ nanofillers into the PAN matrix significantly enhanced the output signals. When PAN–SGZ was used as the tribopositive layer, the TENGs exhibited peak-to-peak voltages of 0.84 V and 0.94 V, and peak currents of 0.82 µA and 0.88 µA at loadings of

0.25% and 0.5%, respectively. Among all samples, the device based on 1% SGZ doped PAN nanofibers showed the highest performance, generating a peak-to-peak voltage of 1.02 V representing a 70% increase and a current of 1.05 µA, corresponding to a 57% enhancement. The power density of the TENG devices also improved with increasing SGZ content up to 1 wt.%: 431.25 µW/m², 518.75 µW/m², and 693.75 µW/m² were recorded for devices containing 0.25, 0.5, and 1 wt.% SGZ, respectively (Figure V.18). These findings indicate that SGZ nanofiller acts as an effective tribocharge modulator in PAN-based electrospun nanofibers, enhancing the overall triboelectric performance.

The improved output performance of the TENG devices incorporating SGZ nanofillers can be attributed to several synergistic effects on the surface and dielectric properties of the PAN–SGZ nanofibers. First, the high surface area of GO sheets enhances the charge mobility, while its amino functional groups improve electron-donating capability upon contact with the tribonegative layer. These groups also contribute to better dispersion of the SGZ nanofillers within the PAN matrix, promoting uniform charge distribution and efficient transfer during the contact–separation cycles. In addition, the presence of ZrO_2 nanoparticles increases the dielectric constant of the nanocomposite and introduces surface sites for charge trapping, which enhances charge retention during operation [223,224]. Moreover, the incorporation of SGZ leads to increased surface roughness in the nanofibrous mat as observed in SEM analysis, which improves the effective contact area during triboelectric interaction [165,225,226]. These combined factors enhanced surface charge density, improved dielectric properties, and increased surface roughness collectively contribute to more efficient charge generation and retention, thereby significantly improving the overall output performance of the TENG.

On the other hand, at a higher SGZ concentration of 2 wt%, the output performance of TENG decreased (Figures V.17 and V.18), with a peak-to-peak voltage of 0.52 V and a peak-to-peak current of 0.7 µA. The reduction could be attributed to excessive nanofiller loading which can lead to agglomeration, further compromising the dielectric properties. Additionally, the presence of beads disrupts fiber continuity and reduces the effective contact area between triboelectric surfaces, thereby negatively impacting charge generation [155,165].

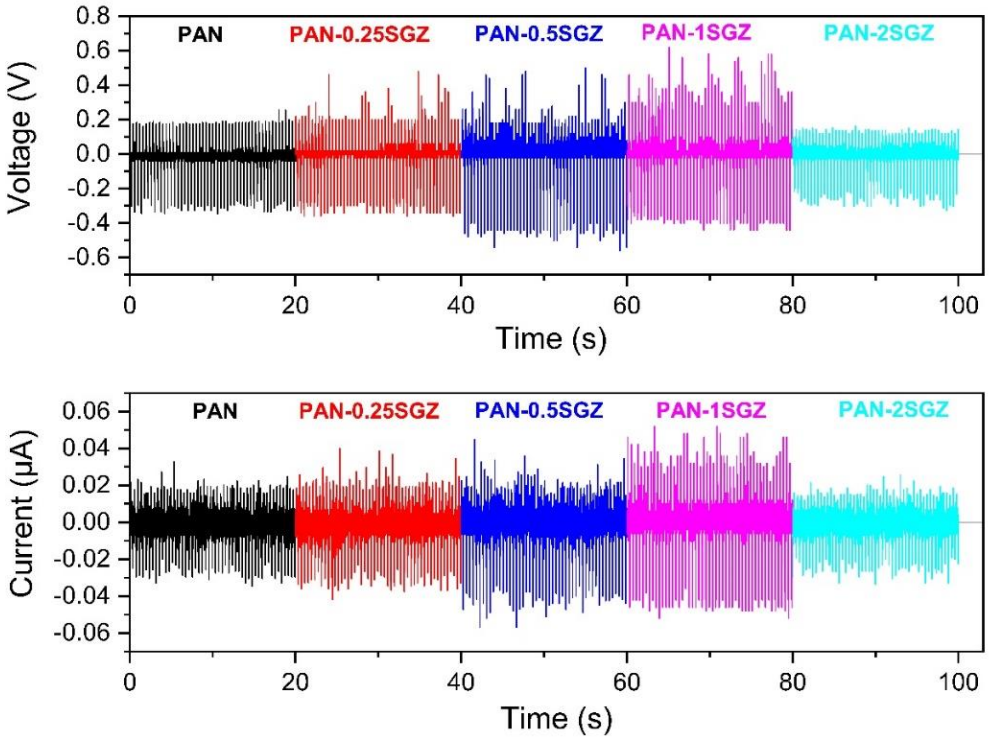

Figure V.17: Output voltage and output current graphs of the fabricated TENGs.

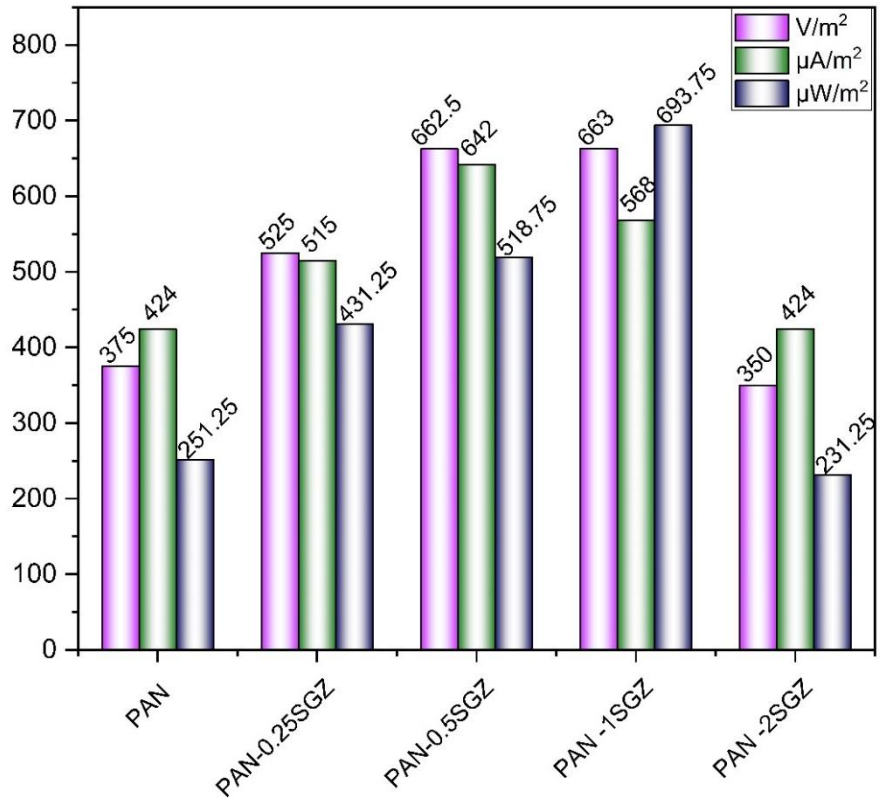

Figure V.18: Voltage density, current density and power density of the fabricated TENGs.

GENERAL CONCLUSION

GENERAL CONCLUSION

In this study, graphene oxide (GO) was synthetized using the modified Hummers method and subsequently functionalized its surface with amino silane N-(b-aminoethyl)-c-aminopropyltrimethoxysilane (AEAPTMS), resulting in silane-graphene oxide (SGO). The surface of SGO is then decorated with zirconium oxide (ZrO2) nanoparticles, generating SGO-ZrO_2 nanohybrids.

A comprehensive suite of characterization techniques confirmed the successful synthesis and provided insight into the structural, chemical, and morphological features of the nanohybrids. FTIR and XPS analyses confirmed the presence of amine functionalities and Zr–O bonds, validating both the silanization and nanoparticle attachment processes. XRD and Raman spectroscopy revealed the structural integrity and phase distribution of the GO and ZrO_2 components. TGA results affirmed that SGO-ZrO_2 nanohybrids exhibited a higher thermal stability than GO nanosheets which indicates the positive effect of ZrO_2 decoration. while zeta potential measurements indicated surface charge characteristics and colloidal stability. Additionally, SEM imaging confirmed the uniform distribution of ZrO_2 nanoparticles across the GO sheets.

Following the synthesis process of nanohybrids, the SGO-ZrO_2 nanohybrids were incorporated into electrospun polyacrylonitrile (PAN) nanofibers to fabricate nanocomposite mats for triboelectric nanogenerator (TENG) applications. By integrating these nanohybrids into PAN electrospun nanofibers, several key findings were confirmed through characterization: FTIR analysis indicated chemical interactions between SGO-ZrO_2 and PAN; XRD analysis confirmed the presence of the SGO-ZrO_2 into PAN matrix and showed a significant enhancement in the crystallinity of the PAN-SGO-ZrO_2 nanocomposite; DSC analysis demonstrated better thermal stability; mechanical testing revealed improvements in both tensile stress and elastic modulus of the PAN-SGO-ZrO_2 nanocomposite and SEM images showed a uniform distribution of the nanofibers.

The TENG devices fabricated from these nanofiber composites exhibited significantly improved output voltage and power density compared to neat PAN counterparts,

Overall, this work establishes a promising strategy for developing advanced TENG materials through chemical surface engineering and hybrid nanostructure design. The successful synthesis and integration of SGO-ZrO_2 into PAN nanofibers not only provide a platform for scalable and high-performance energy harvesters but also open avenues for further functionalization, device optimization, and application in rigid surface-mounted sensors, and energy harvesting from mechanical vibrations in industrial settings.

Bibliographic references

Bibliographic References

1. Maduraiveeran, G.; Jin, W. Carbon nanomaterials: Synthesis, properties and applications in electrochemical sensors and energy conversion systems. Materials Science and Engineering: B. Elsevier Ltd October 1, 2021. doi:10.1016/j.mseb.2021.115341.

2. Kumar Mahato, P.; Choudhuri, S.; Kumar, C.; Roy, S.; Patra, P. Evaluation of crystal size present in graphene oxide quantum dots using optical and Raman spectroscopy. In Materials Today: Proceedings; Elsevier Ltd, 2023; Vol. 80, pp 668–673. doi:10.1016/j.matpr.2022.11.066.

3. Shuai, C.; Yang, F.; Shuai, Y.; Peng, S.; Chen, S.; Deng, Y.; et al. Silicon dioxide nanoparticles decorated on graphene oxide nanosheets and their application in poly(L-lactic acid) scaffold. Journal of Advanced Research 2023, 48, 175–190. doi:10.1016/j.jare.2022.08.017.

4. Lee, C. Y.; Bae, J. H.; Kim, T. Y.; Chang, S. H.; Kim, S. Y. Using silane-functionalized graphene oxides for enhancing the interfacial bonding strength of carbon/epoxy composites. Composites Part A: Applied Science and Manufacturing 2015, 75, 11–17. doi:10.1016/j.compositesa.2015.04.013.

5. Sharif, N. A.; Ehsani, M.; Zaarei, D.; Kalaee, M. R.; Khajavi, R. Nanocomposite Coatings Based on Modified Graphene Oxide and Polydimethylsiloxane: Characterization and Thermal Properties. Russian Journal of Applied Chemistry 2020, 93(11), 1765–1773. doi:10.1134/S1070427220110191.

6. Chen, D.; Feng, H.; Li, J. Graphene oxide: Preparation, functionalization, and electrochemical applications. Chemical Reviews. November 14, 2012, 6027–6053. doi:10.1021/cr300115g.

7. Zhu, D.; Hu, N.; Schaefer, D. W. Water-based sol–gel coatings for military coating applications. In Handbook of Waterborne Coatings; Elsevier, 2020; 1–27. doi:10.1016/b978-0-12-814201-1.00001-9.

8. Vuppaladadium, S. S. R.; Agarwal, T.; Kulanthaivel, S.; Mohanty, B.; Barik, C. S.; Maiti, T. K.; et al. Silanization improves biocompatibility of graphene oxide. Materials Science and Engineering C 2020, 110. doi: 10.1016/j.msec.2020.110647.

9. Yang, H.; Li, F.; Shan, C.; Han, D.; Zhang, Q.; Niu, L.; et al. Covalent functionalization of chemically converted graphene sheets via silane and its reinforcement. Journal of Materials Chemistry 2009, 19(26), 4632–4638. doi:10.1039/b901421g.

10. Pourhashem, S.; Vaezi, M. R.; Rashidi, A.; Bagherzadeh, M. R. Distinctive roles of silane coupling agents on the corrosion inhibition performance of graphene oxide in epoxy coatings. Progress in Organic Coatings 2017, 111, 47–56. doi: 10.1016/j.porgcoat.2017.05.008.

11. Dun, Y.; Zuo, Y. Preparation and characterization of a GPTMS/graphene coating on AA-2024 alloy. Applied Surface Science 2017, 416, 492–502. doi: 10.1016/j.apsusc.2017.04.116.

12. Liu, J. ; Yu, Q. ; Yu, M. ; Li, S. ; Zhao, K. ; Xue, B. ; et al. Silane modification of titanium dioxide-decorated graphene oxide nanocomposite for enhancing anticorrosion performance of epoxy coatings on AA-2024. Journal of Alloys and Compounds 2018, 744, 728–739. doi: 10.1016/j.jallcom.2018.01.267.

13. Cho, B. H.; Ko, W. B. Preparation of graphene-Al_2O_3 nanocomposites by heat treatment and photocatalytic degradation of organic dyes. Journal of Nanoscience and Nanotechnology 2013, 13(11), 7625–7630. doi:10.1166/jnn.2013.7819.

14. Liu, S.; Zhu, Y.; Zheng, X.; Lai, X.; Jia, R.; Yuan, X. Graphene oxide modified by zirconium dioxide to enhance the corrosion resistance of Zinc/Aluminum coatings. Diamond and Related Materials 2020, 108. doi: 10.1016/j.diamond.2020.107868.

15. Teymourian, H.; Salimi, A.; Firoozi, S.; Korani, A.; Soltanian, S. One-pot hydrothermal synthesis of zirconium dioxide nanoparticles decorated reduced graphene oxide composite as high-performance electrochemical sensing and biosensing platform. Electrochimica Acta 2014, 143, 196–206. doi: 10.1016/j.electacta.2014.08.007.

16. Di, H.; Yu, Z.; Ma, Y.; Zhang, C.; Li, F.; Lv, L.; et al. Corrosion-resistant hybrid coatings based on graphene oxide–zirconia dioxide/epoxy system. Journal of the Taiwan Institute of Chemical Engineers 2016, 67, 511–520. doi: 10.1016/j.jtice.2016.08.008.

17. Toorchi, D.; Khosravi, H.; Tohidlou, E. Synergistic effect of nano-ZrO_2/graphene oxide hybrid system on the high-velocity impact behavior and interlaminar shear strength of basalt fiber/epoxy composite. Journal of Industrial Textiles 2021, 51(2), 277–296. doi:10.1177/1528083719879922.

18. Wang, Z. L.; Song, J. Piezoelectric Nanogenerators Based on Zinc Oxide Nanowire Arrays. Science 2006, 312(5771), 242–246. doi:10.1126/science.1124005.

19. Wang, S.; Lin, L.; Wang, Z. L. Nanoscale Triboelectric-Effect-Enabled Energy Conversion for Sustainably Powering Portable Electronics. Nano Letters 2012, 12(12), 6339–6346. doi:10.1021/nl303573d.

20. Babu, A.; Aazem, I.; Walden, R.; Bairagi, S.; Mulvihill, D. M.; Pillai, S. C. Electrospun nanofiber based TENGs for wearable electronics and self-powered sensing. Chemical Engineering Journal 2023, 452, 139060. doi:10.1016/j.cej.2022.139060.

21. Wei, Q.; Cao, Y.; Yang, X.; Jiao, G.; Qi, X.; Wen, G. Recent Developments in Electrospun Nanofiber-Based Triboelectric Nanogenerators: Materials, Structure, and Applications. Membranes 2024, 14(12), 271. doi:10.3390/membranes14120271.

22. Kausar, A. Polyacrylonitrile-based nanocomposite fibers: A review of current developments. Journal of Plastic Film & Sheeting 2019, 35(3), 295–316. doi:10.1177/8756087919828151.

23. Hatta, F. F.; Mohammad Haniff, M. A. S.; Mohamed, M. A. A review on applications of graphene in triboelectric nanogenerators. International Journal of Energy Research 2022, 46(2), 544–576. doi:10.1002/er.7245.

24. Huang, T.; Lu, M.; Yu, H.; Zhang, Q.; Wang, H.; Zhu, M. Enhanced Power Output of a Triboelectric Nanogenerator Composed of Electrospun Nanofiber Mats Doped with Graphene Oxide. Scientific Reports 2015, 5(1), 13942. doi:10.1038/srep13942.

25. Yar, A.; Karabiber, A.; Ozen, A.; Ozel, F.; Coskun, S. Flexible nanofiber based triboelectric nanogenerators with high power conversion. Renewable Energy 2020, 162, 1428–1437. doi:10.1016/j.renene.2020.08.030.

26. Saikh, Md. M.; Hoque, N. A.; Biswas, P.; Rahman, W.; Das, N.; Das, S.; et al. Self-Polarized ZrO_2 /Poly(vinylidene fluoride- co -hexafluoropropylene) Nanocomposite-Based Piezoelectric Nanogenerator and Single-Electrode Triboelectric Nanogenerator for Sustainable Energy Harvesting from Human Movements. physica status solidi (a) 2021, 218(9). doi:10.1002/pssa.202000695.

27. Zhang, L.; Wu, H.; Wei, M.; Zheng, Z.; Vu, D. D.; Bui, T. T. X.; et al. Preparation, characterization, and properties of graphene oxide/urushiol-formaldehyde polymer composite coating. Journal of Coatings Technology and Research 2018, 15(6), 1343–1356. doi:10.1007/s11998-018-0084-1.

28. Karthik, P. S.; Himaja, A. L.; Singh, S. P. Carbon-allotropes: Synthesis methods, applications and future perspectives. Carbon Letters. Korean Carbon Society October 1, 2014, pp 219–237. doi:10.5714/CL.2014.15.4.219.

29. Saoudi, L. Contrôle de La Chimie de Surface et Mise En Forme Du Nanodiamant Pour La Production de Carburants Solaires. Université Paris-Saclay, France, 2023. https://theses.hal.science/tel-04417192

30. Tavares, C. Etude et Réalisation de jonctions p/n en diamant. Université Joseph-Fourier-Grenoble I, France, 2006. https://theses.hal.science/tel-00201822v1.

31. Pierson, H. O. Handbook Of Carbon, Graphite, Diamond And Fullerenes Properties, Processing and Applications. 1993.

32. Gudarzi, M. M.; Aboutalebi, S. H.; Sharif, F. Graphene Oxide-Based Composite Materials. In Graphene Oxide: Fundamentals and Applications; wiley, 2016; 314–363. doi:10.1002/9781119069447.ch10.

33. Kroto, H. Space, Stars, C60 , and Soot. Science 1988, 242(4882), 1139–1145. doi:10.1126/science.242.4882.1139.

34. Iijima, S. Helical microtubules of graphitic carbon. Nature 1991, 354(6348), 56–58. doi:10.1038/354056a0.

35. Almadori, Y. Fonctionnalisation Non-Covalente de Nanotubes de Carbone Mono-Feuillets : Étude Du Confinement de Molécules Photo-Actives et Intercalation de Rubidium. Université Montpellier II, France, 2013. https://theses.hal.science/tel-00997533v1.

36. Novoselov, K. S.; Geim, A. K.; Morozov, S. V.; Jiang, D.; Zhang, Y.; Dubonos, S. V.; et al. Electric Field Effect in Atomically Thin Carbon Films. Science 2004, 306(5696), 666–669. doi:10.1126/science.1102896.

37. Zhao, Y.; Li, X.; Zhou, X.; Zhang, Y. Review on the graphene based optical fiber chemical and biological sensors. Sensors and Actuators B: Chemical 2016, 231, 324–340. doi:10.1016/j.snb.2016.03.026.

38. Bouibed, A. Etude de nouvelles stratégies de synthèse en vue de concevoir des matériaux hybrides : application au renforcement des polymères, Université Ferhat Abbas Setif 1, Algeria, 2022. http://dspace.univ-setif.dz:8888/jspui/handle/123456789/4047.

39. Chaabane, L. Graphene Oxide-Based Materials : From Water Depollution to the Catalysis of Oganic Reactions. Université de Lyon, France, 2020. https://theses.hal.science/tel-03905718v1.

40. Geim, A. K.; Novoselov, K. S. The Rise Of Graphene. Nature Materials 2007, 6(3), 183–191. doi:10.1038/nmat1849.

41. Scarselli, M.; Castrucci, P.; De Crescenzi, M. Electronic and optoelectronic nano-devices based on carbon nanotubes. Journal of Physics: Condensed Matter 2012, 24(31), 313202. doi:10.1088/0953-8984/24/31/313202.

42. Brodie, B. C. XIII. On The Atomic Weight Of Graphite. Philosophical Transactions of the Royal Society of London 1859, 149, 249–259. doi:10.1098/rstl.1859.0013.

43. Staudenmaier, L. Verfahren zur Darstellung der Graphits¨aure.Ber. Dtsch. Chem. Ges 1898, 31 (2) 1481–1487, https://doi.org/10.1002/cber.18980310237.

44. Hummers, W.S. Offeman R.E., Preparation of graphitic oxide, J. Am. Chem. Soc 1958, 80 (6) 1339, https://doi.org/10.1021/ja01539a017.

45. Vacchi, I. A. Controlled Chemical Functionalization of Graphene Oxide. Université de Strasbourg, France, 2017. https://theses.hal.science/tel-03934593.

46. Winkler, I.; Silva, A. G. da; Henriques, A. C.; Freitas, F. V. de; Gomes, M. V. M. Towards an immersive product development process: opportunities and challenges for the automotive industry. In Advanced and sustainable technologies for automotive industry innovation; Pimenta Cultural, 2023; pp 140–160. doi:10.31560/pimentacultural/2022.96153.8.

47. Yap, Y. W.; Mahmed, N.; Norizan, M. N.; Abd Rahim, S. Z.; Ahmad Salimi, M. N.; Abdul Razak, K.; et al. Recent Advances in Synthesis of Graphite from Agricultural Bio-Waste Material: A Review. Materials 2023, 16(9), 3601. doi:10.3390/ma16093601.

48. Marcano, D. C.; Kosynkin, D. V.; Berlin, J. M.; Sinitskii, A.; Sun, Z.; Slesarev, A.; et al. Improved synthesis of graphene oxide. ACS Nano 2010, 4(8), 4806–4814. doi:10.1021/nn1006368.

49. Brisebois, P. P.; Siaj, M. Harvesting graphene oxide-years 1859 to 2019: A review of its structure, synthesis, properties and exfoliation. Journal of Materials Chemistry C 2020, 8(5), 1517–1547. doi:10.1039/c9tc03251g.

50. Garcia, A. P. Etude de La Chimie de La Fonctionnalisation de l'oxyde de Graphène Pour Concevoir Des Matériaux à Base de l'oxyde de Graphène Pour Des Applications Antibactériennes. Université Paris, France, 2021. https://pastel.hal.science/tel-03655474v1.

51. Chergui, S. Fabrication et Biofonctionalisation d'une Mousse d'oxyde de Graphène Par Des Aptamères Pour Une Décontamination Sélective En Milieu Aqueux. Université du Québec, Canada, 2018. http://archipel.uqam.ca/id/eprint/11187.

52. Paredes, J. I.; Villar-Rodil, S.; Martínez-Alonso, A.; Tascón, J. M. D. Graphene oxide dispersions in organic solvents. Langmuir 2008, 24(19), 10560–10564. doi:10.1021/la801744a.

53. Park, W. K.; Yoon, Y.; Song, Y. H.; Choi, S. Y.; Kim, S.; Do, Y.; et al. High-efficiency exfoliation of large-area mono-layer graphene oxide with controlled dimension. Scientific Reports 2017, 7(1). doi:10.1038/s41598-017-16649-y.

54. Smith, A. T.; LaChance, A. M.; Zeng, S.; Liu, B.; Sun, L. Synthesis, properties, and applications of graphene oxide/reduced graphene oxide and their nanocomposites. Nano Materials Science 2019, 1(1), 31–47. doi:10.1016/j.nanoms.2019.02.004.

55. Dong, L.; Chen, Z.; Lin, S.; Wang, K.; Ma, C.; Lu, H. Reactivity-Controlled Preparation of Ultralarge Graphene Oxide by Chemical Expansion of Graphite. Chemistry of Materials 2017, 29(2), 564–572. doi:10.1021/acs.chemmater.6b03748.

56. Jiříčková, A.; Jankovský, O.; Sofer, Z.; Sedmidubský, D. Synthesis and Applications of Graphene Oxide. Materials 2022, 15(3), 920. doi:10.3390/ma15030920.

57. Hofmann, U.; Holst, R. Über die Säurenatur und die Methylierung von Graphitoxyd. Berichte der deutschen chemischen Gesellschaft (A and B Series) 1939, 72(4), 754–771. doi:10.1002/cber.19390720417.

58. Ruess, G.; Vogt, F. Höchstlamellarer Kohlenstoff aus Graphitoxyhydroxyd. Monatshefte für Chemie 1948, 78(3–4), 222–242. doi:10.1007/BF01141527.

59. Scholz, W.; Boehm, H. P. Untersuchungen am Graphitoxid. VI. Betrachtungen zur Struktur des Graphitoxids. Zeitschrift für anorganische und allgemeine Chemie 1969, 369(3–6), 327–340. doi:10.1002/zaac.19693690322.

60. Nakajima, T.; Mabuchi, A.; Hagiwara, R. A new structure model of graphite oxide. Carbon 1988, 26(3), 357–361. doi:10.1016/0008-6223(88)90227-8.

61. Lerf, A.; He, H.; Forster, M.; Klinowski, J. Structure of Graphite Oxide Revisited. The Journal of Physical Chemistry B 1998, 102(23), 4477–4482. doi:10.1021/jp9731821.

62. Tama´s Szabo´; Otto´ Berkesi; Pe´ter Forgo´; Katalin Josepovits; Yiannis Sanakis; Dimitris Petridis; et al. Evolution of Surface Functional Groups in a Series of Progressively Oxidized Graphite Oxides. Chem. Mater 2006, 18, 2740–2749. doi:10.1021/cm060258+.

63. Gao, W.; Alemany, L. B.; Ci, L.; Ajayan, P. M. New insights into the structure and reduction of graphite oxide. Nature Chemistry 2009, 1(5), 403–408. doi:10.1038/nchem.281.

64. ZEBIRI, A. Nanocomposites A Matrice Polymeres Et Renforts De Structure Lamellaire : Effet Des Interactions Generees A L'interface Par La Modification Et La Compatibilisation Sur Les Proprietes Des Materiaux. Université Ferhat Abbas Setif 1, Algeria, 2023. http://dspace.univ setif.dz:8888/jspui/handle/123456789/4171

65. Machado, B. F.; Serp, P. Graphene-based materials for catalysis. Catal. Sci. Technol. 2012, 2(1), 54–75. doi:10.1039/C1CY00361E.

66. Kim, J.; Cote, L. J.; Kim, F.; Yuan, W.; Shull, K. R.; Huang, J. Graphene Oxide Sheets at Interfaces. Journal of the American Chemical Society 2010, 132(23), 8180–8186. doi:10.1021/ja102777p.

67. Montes-Navajas, P.; Asenjo, N. G.; Santamaría, R.; Menéndez, R.; Corma, A.; García, H. Surface Area Measurement of Graphene Oxide in Aqueous Solutions. Langmuir 2013, 29(44), 13443–13448. doi:10.1021/la4029904.

68. Suk, J. W.; Piner, R. D.; An, J.; Ruoff, R. S. Mechanical Properties of Monolayer Graphene Oxide. ACS Nano 2010, 4(11), 6557–6564. doi:10.1021/nn101781v.

69. Bouchareb, S.; Doufnoune, R.; Riahi, F.; Cherif-Silini, H.; Belbahri, L. Non-covalent functionalization of graphene oxide using self-assembly of silver-triphenylphosphine for bactericidal formulations. Materials Chemistry and Physics 2020, 243. doi:10.1016/j.matchemphys.2019.122598.

70. Zhao, B.; Liu, P. W.; Liu, D. Y.; Kolibaba, T. J.; Zhang, C. Y.; Liu, Y. T.; et al. Functionalized Graphene Oxide Based on Hydrogen-Bonding Interaction in Water: Preparation and Flame-Retardation on Epoxy Resin. Macromolecular Materials and Engineering 2019, 304(8). doi:10.1002/mame.201900164.

71. Lv, M.; Yan, L.; Liu, C.; Su, C.; Zhou, Q.; Zhang, X.; et al. Non-covalent functionalized graphene oxide (GO) adsorbent with an organic gelator for co-adsorption of dye, endocrine-disruptor, pharmaceutical and metal ion. Chemical Engineering Journal 2018, 349, 791–799. doi:10.1016/j.cej.2018.04.153.

72. Yu, D.; Yang, Y.; Durstock, M.; Baek, J.-B.; Dai, L. Soluble P3HT-Grafted Graphene for Efficient Bilayer−Heterojunction Photovoltaic Devices. ACS Nano 2010, 4(10), 5633–5640. doi:10.1021/nn101671t.

73. Gong, X.; Liu, G.; Li, Y.; Yu, D. Y. W.; Teoh, W. Y. Functionalized-graphene composites: Fabrication and applications in sustainable energy and environment. Chemistry of Materials. American Chemical Society November 22, 2016, 8082–8118. doi:10.1021/acs.chemmater.6b01447.

74. Stankovich, S.; Piner, R. D.; Nguyen, S. B. T.; Ruoff, R. S. Synthesis and exfoliation of isocyanate-treated graphene oxide nanoplatelets. Carbon 2006, 44(15), 3342–3347. doi:10.1016/j.carbon.2006.06.004.

75. Wang, S.; Chia, P.; Chua, L.; Zhao, L.; Png, R.; Sivaramakrishnan, S.; et al. Band-like Transport in Surface-Functionalized Highly Solution-Processable Graphene Nanosheets. Advanced Materials 2008, 20(18), 3440–3446. doi:10.1002/adma.200800279.

76. Yang, H.; Li, F.; Shan, C.; Han, D.; Zhang, Q.; Niu, L.; et al. Covalent functionalization of chemically converted graphene sheets via silane and its reinforcement. Journal of Materials Chemistry 2009, 19(26), 4632–4638. doi:10.1039/b901421g.

77. López, S.; Bergueiro, J.; Fidalgo, J. Silane. In Encyclopedia of Toxicology; Elsevier, 2014; pp 261–263. doi:10.1016/B978-0-12-386454-3.01180-5.

78. Mezhuev, Ya. O. Silane. In Encyclopedia of Toxicology; Elsevier, 2024; 513–516. doi:10.1016/B978-0-12-824315-2.00935-0.

79. Lotfi, M.; Azizi, A.; Yari, H.; Ganjaee Sari, M. Aminosilane-co-Graphene Oxide/Epoxy nanocomposite coating: An approach towards toughness and viscoelastic properties enhancement. Progress in Organic Coatings 2021, 151. doi:10.1016/j.porgcoat.2020.106050.

80. Lotfi, M.; Yari, H.; Sari, M. G.; Azizi, A. Fabrication of a highly hard yet tough epoxy nanocomposite coating by incorporating graphene oxide nanosheets dually modified with amino silane coupling agent and hyperbranched polyester-amide. Progress in Organic Coatings 2022, 162. doi:10.1016/j.porgcoat.2021.106570.

81. Yamada, A.; Sasabe, H.; Osada, Y.; Shiroda, Y. Concepts of Hybrid Materials, Hybrid Materials –Concept and Case Studies. ASM International 1989.

82. Makishima, A. Possibility of Hybrids Materials. CERAMICS JAPAN 2004. 39, 90–91.

83. Gómez-Romero, P.; Sanchez, C. Hybrid Materials, Functional Applications. An Introduction. In Functional Hybrid Materials; Wiley, 2003, 1–14. doi:10.1002/3527602372.ch1.

84. Niizeki, N. What are Hybrid Materials. Sensor Tech 1986, 6(2), 42–44.

85. Makoto, N. Definitions and Categories of Hybrid Materials. Advances in technology of materials and materials processing journal, 2009, 11(1), 1–8. doi: 10.2240/azojomo0288.

86. Wang, Z-L. Characterization of Nanophase Materials, Ed.; Wiley, 1999. doi:10.1002/3527600094.

87. Niederberger, M.; Pinna, N. Metal Oxide Nanoparticles in Organic Solvents; Springer London: London, 2009. doi:10.1007/978-1-84882-671-7.

88. Sepúlveda, P.; Espinoza, L. C.; Garcia-Garcia, A. Applications of graphene oxide (GO) and its hybrid with nanoparticles for water decontamination. In Advanced Materials for Sustainable Environmental Remediation: Terrestrial and Aquatic Environments; Elsevier, 2022; 513–532. doi:10.1016/B978-0-323-90485-8.00004-7.

89. Sahoo, J. K.; Paikra, S. K.; Baliarsingh, A.; Panda, D.; Rath, S.; Mishra, M.; et al. Surface functionalization of graphene oxide using amino silane magnetic nanocomposite for Chromium (VI) removal and bacterial treatment. Nano Express 2020, 1(1). doi:10.1088/2632-959X/ab9e3f.

90. Das, R. S.; Warkhade, S. K.; Kumar, A.; Wankhade, A. V. Graphene oxide-based zirconium oxide nanocomposite for enhanced visible light-driven photocatalytic activity. Research on Chemical Intermediates 2019, 45(4), 1689–1705. doi:10.1007/s11164-018-3699-z.

91. Rao, R. A. K.; Singh, S.; Singh, B. R.; Khan, W.; Naqvi, A. H. Synthesis and characterization of surface modified graphene-zirconium oxide nanocomposite and its possible use for the removal of chlorophenol from aqueous solution. Journal of Environmental Chemical Engineering 2014, 2(1), 199–210. doi:10.1016/j.jece.2013.12.011.

92. Smirnov, A.; Pinargote, N. W. S.; Peretyagin, N.; Pristinskiy, Y.; Peretyagin, P.; Bartolomé, J. F. Zirconia reduced graphene oxide nano-hybrid structure fabricated by the hydrothermal reaction method. Materials 2020, 13(3). doi:10.3390/ma13030687.

93. Formhals Anton. PROCESS AND APPARATUS FOR PREPARING ARTIFICIAL THREADS 1934 . FQRMHALS 1,975,504. US1975504A

94. Li, D.; Xia, Y. Electrospinning of Nanofibers: Reinventing the Wheel. Advanced Materials 2004, 16(14), 1151–1170. doi:10.1002/adma.200400719.

95. Baumgarten, P. K. Electrostatic spinning of acrylic microfibers. Journal of Colloid and Interface Science 1971, 36(1), 71–79. doi:10.1016/0021-9797(71)90241-4.

96. Al-Abduljabbar, A.; Farooq, I. Electrospun Polymer Nanofibers: Processing, Properties, and Applications. Polymers 2022, 15(1), 65. doi:10.3390/polym15010065.

97. Zhang, Y. Z.; Venugopal, J.; Huang, Z.-M.; Lim, C. T.; Ramakrishna, S. Crosslinking of the electrospun gelatin nanofibers. Polymer 2006, 47(8), 2911–2917. doi:10.1016/j.polymer.2006.02.046.

98. Ramalingam, M.; Ramakrishna, S. Introduction to nanofiber composites. In Nanofiber Composites for Biomedical Applications; Elsevier, 2017; 3–29. doi:10.1016/B978-0-08-100173-8.00001-6.

99. Doshi, J.; Reneker, D. H. Electrospinning process and applications of electrospun fibers. Journal of Electrostatics 1995, 35(2–3), 151–160. doi:10.1016/0304-3886(95)00041-8.

100. Altin, Y.; Celik Bedeloglu, A. Polyacrylonitrile Nanofiber Optimization as Precursor of Carbon Nanofibers for Supercapacitors. Journal of Innovative Science and Engineering 2020, 2020(2), 69–83. doi:10.38088/jise.

101. Gholipour Kanani, A.; Bahrami, S. H. Effect of Changing Solvents on Poly(-Caprolactone) Nanofibrous Webs Morphology. Journal of Nanomaterials 2011, 2011, 1–10. doi:10.1155/2011/724153.

102. Fong, H.; Chun, I.; Reneker, D. H. Beaded nanofibers formed during electrospinning. Polymer 1999, 40(16), 4585–4592. doi:10.1016/S0032-3861(99)00068-3.

103. Haider, A.; Haider, S.; Kang, I.-K. A comprehensive review summarizing the effect of electrospinning parameters and potential applications of nanofibers in biomedical and biotechnology. Arabian Journal of Chemistry 2018, 11(8), 1165–1188. doi:10.1016/j.arabjc.2015.11.015.

104. Laudenslager MJ; Sigmund WM. electrospinning. In Encyclopedia of Nanotechnology; Springer 2012, 769–775. https://doi.org/10.1007/978-90-481-9751-4_357.

105. Megelski, S.; Stephens, J. S.; Chase, D. B.; Rabolt, J. F. Micro- and Nanostructured Surface Morphology on Electrospun Polymer Fibers. Macromolecules 2002, 35(22), 8456–8466. doi:10.1021/ma020444a.

106. Theron, S. A.; Zussman, E.; Yarin, A. L. Experimental investigation of the governing parameters in the electrospinning of polymer solutions. Polymer 2004, 45(6), 2017–2030. doi:10.1016/j.polymer.2004.01.024.

107. Matabola, K. P.; Moutloali, R. M. The influence of electrospinning parameters on the morphology and diameter of poly(vinyledene fluoride) nanofibers- effect of sodium chloride. Journal of Materials Science 2013, 48(16), 5475–5482. doi:10.1007/s10853-013-7341-6.

108. Jiang, S.; Chen, Y.; Duan, G.; Mei, C.; Greiner, A.; Agarwal, S. Electrospun nanofiber reinforced composites: A review. Polymer Chemistry. Royal Society of Chemistry May 28, 2018, pp 2685–2720. doi:10.1039/c8py00378e.

109. Tao, D.; Su, P.; Chen, A.; Gu, D.; Eginligil, M.; Huang, W. Electro-spun nanofibers-based triboelectric nanogenerators in wearable electronics: status and perspectives. Flexible Electronics 2025, 9(1), 4. doi:10.1038/s41528-024-00357-5.

110. Adegbola, T. A.; Agboola, O.; Fayomi, O. S. I. Review of polyacrylonitrile blends and application in manufacturing technology: recycling and environmental impact. Results in Engineering 2020, 7, 100144. doi:10.1016/j.rineng.2020.100144.

111. Rose, A.; Guru Prasad, K.; Sakthivel, T.; Gunasekaran, V.; Maiyalagan, T.; Vijayakumar, T. Electrochemical analysis of Graphene Oxide/Polyaniline/Polyvinyl alcohol composite nanofibers for supercapacitor applications. Applied Surface Science 2018, 449, 551–557. doi:10.1016/j.apsusc.2018.02.224.

112. Uddin, Md. E.; Layek, R. K.; Kim, N. H.; Hui, D.; Lee, J. H. Preparation and properties of reduced graphene oxide/polyacrylonitrile nanocomposites using polyvinyl phenol. Composites Part B: Engineering 2015, 80, 238–245. doi:10.1016/j.compositesb.2015.06.009.

113. Kaur, N.; Kumar, V.; Dhakate, S. R. Synthesis and characterization of multiwalled CNT–PAN based composite carbon nanofibers via electrospinning. SpringerPlus 2016, 5(1), 483. doi:10.1186/s40064-016-2051-6.

114. Abdel-Mottaleb, M. M.; Mohamed, A.; Karim, S. A.; Osman, T. A.; Khattab, A. Preparation, characterization, and mechanical properties of polyacrylonitrile (PAN)/graphene oxide (GO) nanofibers. Mechanics of Advanced Materials and Structures 2020, 27(4), 346–351. doi:10.1080/15376494.2018.1473535.

115. Zhang, J.; Xue, Q.; Pan, X.; Jin, Y.; Lu, W.; Ding, D.; et al. Graphene oxide/polyacrylonitrile fiber hierarchical-structured membrane for ultra-fast microfiltration of oil-water emulsion. Chemical Engineering Journal 2017, 307, 643–649. doi:10.1016/j.cej.2016.08.124.

116. Wang, Q.; Du, Y.; Feng, Q.; Huang, F.; Lu, K.; Liu, J.; et al. Nanostructures and surface nanomechanical properties of polyacrylonitrile/graphene oxide composite nanofibers by electrospinning. Journal of Applied Polymer Science 2013, 128(2), 1152–1157. doi:10.1002/app.38273.

117. Ma, Y.-X.; Yang, H.-J.; Shi, X.-F.; Li, X.-H.; Meng, W.-L. Recovery of Ag(I) from aqueous solution by hyperbranched polyethyleneimine grafted polyacrylonitrile/graphene oxide

electrospun nanocomposite fiber membrane for catalytic reduction of toxic P-nitrophenol. Diamond and Related Materials 2022, 127, 109161. doi:10.1016/j.diamond.2022.109161.

118. Li, X.-H.; Yang, H.-J.; Ma, Y.-X.; Li, T.-Z.; Meng, W.-L.; Zhong, X.-M. A novel PAN/GO electrospun nanocomposite fibrous membranes with rich amino groups for highly efficient adsorption of Au(III). Diamond and Related Materials 2023, 137, 110175. doi:10.1016/j.diamond.2023.110175.

119. Cai, Y.; Wei, Q.; Huang, F. Processing of composite functional nanofibers. In Functional Nanofibers and their Applications; Elsevier, 2012, 38–54. doi:10.1533/9780857095640.1.38.

120. Rujitanaroj, P.; Pimpha, N.; Supaphol, P. Preparation, characterization, and antibacterial properties of electrospun polyacrylonitrile fibrous membranes containing silver nanoparticles. Journal of Applied Polymer Science 2010, 116(4), 1967–1976. doi:10.1002/app.31498.

121. Luoh, R.; Hahn, H. T. Electrospun nanocomposite fiber mats as gas sensors. Composites Science and Technology 2006, 66(14), 2436–2441. doi:10.1016/j.compscitech.2006.03.012.

122. Özcan, M. Green synthesis of ZnO nanoparticles decorating electrospun PAN nanofibers for enhanced radiation shielding. Physica B: Condensed Matter 2024, 674, 415584. doi:10.1016/j.physb.2023.415584.

123. Mpukuta, O.; Dincer, K.; Özaytekin, İ. Effect of Dynamic Viscosity on Nanofiber Diameters and Electrical Conductivity of Polyacrylonitrile Nanofibers Doped Nano-Cu Particles. International Journal of Innovative Engineering Applications 2020, 4(1), 1–8. doi:10.46460/ijiea.707142.

124. Wang, X.; Pan, S.; Zhang, M.; Qi, J.; Sun, X.; Gu, C.; et al. Modified hydrous zirconium oxide/PAN nanofibers for efficient defluoridation from groundwater. Science of The Total Environment 2019, 685, 401–409. doi:10.1016/j.scitotenv.2019.05.380.

125. Sharma, R.; Tiwari, S.; Singh, N.; Tiwari, S. K.; Dhakate, S. R. Highly stable functionalized PAN/Zr nanofibrous mats for removal of ultralow concentrations of Hg (II). Functional Composites and Structures 2023, 5(3), 035008. doi:10.1088/2631-6331/acf849.

126. Abdel-Mottaleb, M. M.; Khalil, A.; Karim, ShroukA.; Osman, T. A.; A.Khattab. High performance of PAN/GO-ZnO composite nanofibers for photocatalytic degradation under visible irradiation. Journal of the Mechanical Behavior of Biomedical Materials 2019, 96, 118–124. doi:10.1016/j.jmbbm.2019.04.040.

127. Sigwadi, R.; Mokrani, T.; Msomi, P. F. Nafion reinforced with polyacrylonitrile nanofibers/zirconium-graphene oxide composite membrane for direct methanol fuel cell application. Journal of Polymer Research 2022, 29(1), 18. doi:10.1007/s10965-021-02854-x.

128. Sahoo, S. K.; Panigrahi, G. K.; Sahoo, J. K.; Pradhan, A. K.; Purohit, A. K.; Dhal, J. P. Electrospun magnetic polyacrylonitrile-GO hybrid nanofibers for removing Cr(VI) from water. Journal of Molecular Liquids 2021, 326, 115364. doi:10.1016/j.molliq.2021.115364.

129. Wang, L.; Ali, J.; Zhang, C.; Mailhot, G.; Pan, G. Simultaneously enhanced photocatalytic and antibacterial activities of TiO2/Ag composite nanofibers for wastewater purification.

Journal of Environmental Chemical Engineering 2020, 8(1), 102104. doi:10.1016/j.jece.2017.12.057.

130. Hartati, S.; Zulfi, A.; Maulida, P. Y. D.; Yudhowijoyo, A.; Dioktyanto, M.; Saputro, K. E.; et al. Synthesis of Electrospun PAN/TiO 2 /Ag Nanofibers Membrane As Potential Air Filtration Media with Photocatalytic Activity. ACS Omega 2022, 7(12), 10516–10525. doi:10.1021/acsomega.2c00015.

131. Karbownik, I.; Fiedot, M.; Rac, O.; Suchorska-Woźniak, P.; Rybicki, T.; Teterycz, H. Effect of doping polyacrylonitrile fibers on their structural and mechanical properties. Polymer 2015, 75, 97–108. doi:10.1016/j.polymer.2015.08.015.

132. Sripadmanabhan Indira, S.; Aravind Vaithilingam, C.; Oruganti, K. S. P.; Mohd, F.; Rahman, S. Nanogenerators as a Sustainable Power Source: State of Art, Applications, and Challenges. Nanomaterials 2019, 9(5), 773. doi:10.3390/nano9050773.

133. Wang, Z. L. Triboelectric Nanogenerators as New Energy Technology for Self-Powered Systems and as Active Mechanical and Chemical Sensors. ACS Nano 2013, 7(11), 9533–9557. doi:10.1021/nn404614z.

134. Davies, D. K. Charge generation on dielectric surfaces. Journal of Physics D: Applied Physics 1969, 2(11), 307. doi:10.1088/0022-3727/2/11/307.

135. Niu, S.; Wang, Z. L. Theoretical systems of triboelectric nanogenerators. Nano Energy 2015, 14, 161–192. doi:10.1016/j.nanoen.2014.11.034.

136. Wang, Z. L.; Chen, J.; Lin, L. Progress in triboelectric nanogenerators as a new energy technology and self-powered sensors. Energy & Environmental Science 2015, 8(8), 2250–2282. doi:10.1039/C5EE01532D.

137. Zi, Y.; Niu, S.; Wang, J.; Wen, Z.; Tang, W.; Wang, Z. L. Standards and figure-of-merits for quantifying the performance of triboelectric nanogenerators. Nature Communications 2015, 6(1), 8376. doi:10.1038/ncomms9376.

138. Vivekananthan, V.; Chandrasekhar, A.; Rao Alluri, N.; Purusothaman, Y.; Khandelwal, G.; Kim, S.-J. Triboelectric Nanogenerators: Design, Fabrication, Energy Harvesting, and Portable-Wearable Applications. In Nanogenerators; IntechOpen, 2020. doi:10.5772/intechopen.90951.

139. Xu, J.; Zou, Y.; Nashalian, A.; Chen, J. Leverage Surface Chemistry for High-Performance Triboelectric Nanogenerators. Frontiers in Chemistry 2020, 8. doi:10.3389/fchem.2020.577327.

140. Wang, Z. L. Triboelectric nanogenerators as new energy technology and self-powered sensors – Principles, problems and perspectives. Faraday Discuss 2014, 176, 447–458. doi:10.1039/C4FD00159A.

141. Wang, Z. L.; Wang, A. C. On the origin of contact-electrification. Materials Today 2019, 30, 34–51. doi:10.1016/j.mattod.2019.05.016.

142. Yan, D.; Ye, J.; Zhou, Y.; Lei, X.; Deng, B.; Xu, W. Research Progress of Fabrics with Different Geometric Structures for Triboelectric Nanogenerators in Flexible and Wearable

Electronics. Advanced Fiber Materials 2023, 5(6), 1852–1878. doi:10.1007/s42765-023-00334-z.

143. Kim, W.-G.; Kim, D.-W.; Tcho, I.-W.; Kim, J.-K.; Kim, M.-S.; Choi, Y.-K. Triboelectric Nanogenerator: Structure, Mechanism, and Applications. ACS Nano 2021, 15(1), 258–287. doi:10.1021/acsnano.0c09803.

144. Lin, S.; Xu, L.; Chi Wang, A.; Wang, Z. L. Quantifying electron-transfer in liquid-solid contact electrification and the formation of electric double-layer. Nature Communications 2020, 11(1), 399. doi:10.1038/s41467-019-14278-9.

145. Xu, C.; Zhang, B.; Wang, A. C.; Zou, H.; Liu, G.; Ding, W.; et al. Contact-Electrification between Two Identical Materials: Curvature Effect. ACS Nano 2019, acsnano.8b08533. doi:10.1021/acsnano.8b08533.

146. Baytekin, H. T.; Patashinski, A. Z.; Branicki, M.; Baytekin, B.; Soh, S.; Grzybowski, B. A. The Mosaic of Surface Charge in Contact Electrification. Science 2011, 333(6040), 308–312. doi:10.1126/science.1201512.

147. Lone, S. A.; Lim, K. C.; Kaswan, K.; Chatterjee, S.; Fan, K.-P.; Choi, D.; et al. Recent advancements for improving the performance of triboelectric nanogenerator devices. Nano Energy 2022, 99, 107318. doi:10.1016/j.nanoen.2022.107318.

148. Dharmasena, R. D. I. G.; Silva, S. R. P. Towards optimized triboelectric nanogenerators. Nano Energy 2019, 62, 530–549. doi:10.1016/j.nanoen.2019.05.057.

149. Kim, H.; Kim, J.; Jun, K.; Kim, J.; Seung, W.; Kwon, O. H.; et al. Silk Nanofiber-Networked Bio-Triboelectric Generator: Silk Bio-TEG. Advanced Energy Materials 2016, 6(8). doi:10.1002/aenm.201502329.

150. Sun, N.; Wang, G.-G.; Zhao, H.-X.; Cai, Y.-W.; Li, J.-Z.; Li, G.-Z.; et al. Waterproof, breathable and washable triboelectric nanogenerator based on electrospun nanofiber films for wearable electronics. Nano Energy 2021, 90, 106639. doi:10.1016/j.nanoen.2021.106639.

151. Li, X.; Yang, Q.; Ren, D.; Li, Q.; Yang, H.; Zhang, X.; et al. A review of material design for high performance triboelectric nanogenerators: performance improvement based on charge generation and charge loss. Nanoscale Advances 2024, 6(18), 4522–4544. doi:10.1039/D4NA00340C.

152. Chen, J.; Guo, H.; He, X.; Liu, G.; Xi, Y.; Shi, H.; et al. Enhancing Performance of Triboelectric Nanogenerator by Filling High Dielectric Nanoparticles into Sponge PDMS Film. ACS Applied Materials & Interfaces 2016, 8(1), 736–744. doi:10.1021/acsami.5b09907.

153. Jian, G.; Meng, Q.; Jiao, Y.; Meng, F.; Cao, Y.; Wu, M. Enhanced performances of triboelectric nanogenerators by filling hierarchical flower-like TiO 2 particles into polymethyl methacrylate film. Nanoscale 2020, 12(26), 14160–14170. doi:10.1039/D0NR02925D.

154. Lee, S. H.; Ko, Y. H.; Yu, J. S. Facile fabrication and characterization of arch-shaped triboelectric nanogenerator with a graphite top electrode. physica status solidi (a) 2015, 212(2), 401–405. doi:10.1002/pssa.201431480.

155. Parandeh, S.; Kharaziha, M.; Karimzadeh, F.; Hosseinabadi, F. Triboelectric nanogenerators based on graphene oxide coated nanocomposite fibers for biomedical applications. Nanotechnology 2020, 31(38), 385402. doi:10.1088/1361-6528/ab9972.

156. Jannesari, M.; Asadian, E.; Ejehi, F.; English, N. J.; Mohammadpour, R.; Sasanpour, P. Boosting on-demand antibacterial activity using electrical stimulations from polypyrrole-graphene oxide triboelectric nanogenerator. Nano Energy 2023, 112, 108463. doi:10.1016/j.nanoen.2023.108463.

157. Harnchana, V.; Ngoc, H. Van; He, W.; Rasheed, A.; Park, H.; Amornkitbamrung, V.; et al. Enhanced Power Output of a Triboelectric Nanogenerator using Poly(dimethylsiloxane) Modified with Graphene Oxide and Sodium Dodecyl Sulfate. ACS Applied Materials & Interfaces 2018, 10(30), 25263–25272. doi:10.1021/acsami.8b02495.

158. Chen, S.; Jiang, J.; Xu, F.; Gong, S. Crepe cellulose paper and nitrocellulose membrane-based triboelectric nanogenerators for energy harvesting and self-powered human-machine interaction. Nano Energy 2019, 61, 69–77. doi:10.1016/j.nanoen.2019.04.043.

159. Zheng, Q.; Fang, L.; Guo, H.; Yang, K.; Cai, Z.; Meador, M. A. B.; et al. Highly Porous Polymer Aerogel Film-Based Triboelectric Nanogenerators. Advanced Functional Materials 2018, 28(13). doi:10.1002/adfm.201706365.

160. Shin, S.-H.; Kwon, Y. H.; Kim, Y.-H.; Jung, J.-Y.; Lee, M. H.; Nah, J. Triboelectric Charging Sequence Induced by Surface Functionalization as a Method To Fabricate High Performance Triboelectric Generators. ACS Nano 2015, 9(4), 4621–4627. doi:10.1021/acsnano.5b01340.

161. Shin, S.-H.; Bae, Y. E.; Moon, H. K.; Kim, J.; Choi, S.-H.; Kim, Y.; et al. Formation of Triboelectric Series via Atomic-Level Surface Functionalization for Triboelectric Energy Harvesting. ACS Nano 2017, 11(6), 6131–6138. doi:10.1021/acsnano.7b02156.

162. Kınas, Z.; Karabiber, A.; Yar, A.; Ozen, A.; Ozel, F.; Ersöz, M.; et al. High-performance triboelectric nanogenerator based on carbon nanomaterials functionalized polyacrylonitrile nanofibers. Energy 2022, 239, 122369. doi:10.1016/j.energy.2021.122369.

163. Zhuo, L.; Goay, A. C. Y.; Sangkarat, P.; Xu, F.; He, Y.; Gao, Z.; et al. Enhanced Triboelectric Outputs from PAN/MoS_2 Nanofiber-Based Nanogenerators for Powering Backscatter Communications in Sustainable 6G Networks. Advanced Energy and Sustainability Research 2025, 6(3). doi:10.1002/aesr.202400301.

164. Ye, Q.; Wu, Y.; Qi, Y.; Shi, L.; Huang, S.; Zhang, L.; et al. Effects of liquid metal particles on performance of triboelectric nanogenerator with electrospun polyacrylonitrile fiber films. Nano Energy 2019, 61, 381–388. doi:10.1016/j.nanoen.2019.04.075.

165. Tabassian, R.; Rajabi-Abhari, A.; Mahato, M.; Yoo, H.; Yoon, H. Y.; Park, J. Y.; et al. Metal-organic framework-based nanofibrous film for two different modes of triboelectric nanogenerators. SmartMat 2024, 5(5). doi:10.1002/smm2.1270.

166. Varghese, H.; Priya K, V.; Hareesh, U. N. S.; Chandran, A. Nanofibrous PAN-PDMS Films-Based High-Performance Triboelectric Artificial Whisker for Self-Powered Obstacle Detection. Macromolecular Rapid Communications 2024, 45(2). doi:10.1002/marc.202300462.

167. Yang, Y.; Yang, Y.; Huang, J.; Li, S.; Meng, Z.; Cai, W.; et al. Electrospun Nanocomposite Fibrous Membranes for Sustainable Face Mask Based on Triboelectric Nanogenerator with High Air Filtration Efficiency. Advanced Fiber Materials 2023, 5(4), 1505–1518. doi:10.1007/s42765-023-00299-z.

168. Park, J.; Jo, S.; Kim, Y.; Zaman, S.; Kim, D. Electrospun Nanofiber Covered Polystyrene Micro-Nano Hybrid Structures for Triboelectric Nanogenerator and Supercapacitor. Micromachines 2022, 13(3), 380. doi:10.3390/mi13030380.

169. Pandey, P.; Thapa, K.; Ojha, G. P.; Seo, M.-K.; Shin, K. H.; Kim, S.-W.; et al. Metal-organic frameworks-based triboelectric nanogenerator powered visible light communication system for wireless human-machine interactions. Chemical Engineering Journal 2023, 452, 139209. doi:10.1016/j.cej.2022.139209.

170. Xie, B.; Guo, Y.; Chen, Y.; Zhang, H.; Xiao, J.; Hou, M.; et al. Advances in Graphene-Based Electrode for Triboelectric Nanogenerator. Nano-Micro Letters 2025, 17(1), 17. doi:10.1007/s40820-024-01530-1.

171. Sharma, R.; Chadha, N.; Saini, P. Determination of Defect Density, Crystallite Size and Number of Graphene Layers in Graphene Analogues Using X-Ray Diffraction and Raman Spectroscopy; 2017; Vol. 55.

172. Caņado, L. G.; Takai, K.; Enoki, T.; Endo, M.; Kim, Y. A.; Mizusaki, H.; et al. General equation for the determination of the crystallite size la of nanographite by Raman spectroscopy. Applied Physics Letters 2006, 88(16). doi:10.1063/1.2196057.

173. Lee, B.-J. Characteristics of Exfoliated Graphite Prepared by Intercalation of Gaseous SO 3 into Graphite. Bulletin of the Korean Chemical Society 2002, 23(12), 1801–1805. doi:10.5012/bkcs.2002.23.12.1801.

174. Ţucureanu, V.; Matei, A.; Avram, A. M. FTIR Spectroscopy for Carbon Family Study. Critical Reviews in Analytical Chemistry. Taylor and Francis Ltd. November 1, 2016, pp 502–520. doi:10.1080/10408347.2016.1157013.

175. Doufnoune, R.; Baouz, T.; Bouchareb, S. Influence of functionalized reduced graphene oxide and compatibilizer on mechanical, thermal and morphological properties of polypropylene/polybutene-1 (PP/PB-1) blends. Journal of Adhesion Science and Technology 2019, 33(16), 1729–1757. doi:10.1080/01694243.2019.1611367.

176. Altin, Y.; Yilmaz, H.; Unsal, O. F.; Bedeloglu, A. C. Graphene oxide modified carbon fiber reinforced epoxy composites. Journal of Polymer Engineering 2020, 40(5), 415–420. doi:10.1515/polyeng-2019-0247.

177. Madhi, A.; Shirkavand Hadavand, B.; Amoozadeh, A. UV-curable urethane acrylate zirconium oxide nanocomposites: Synthesis, study on viscoelastic properties and thermal

behavior. Journal of Composite Materials 2018, 52(21), 2973–2982. doi:10.1177/0021998318756173.

178. Haeri, S. Z.; Ramezanzadeh, B.; Asghari, M. A novel fabrication of a high performance SiO2-graphene oxide (GO) nanohybrids: Characterization of thermal properties of epoxy nanocomposites filled with SiO2-GO nanohybrids. Journal of Colloid and Interface Science 2017, 493, 111–122. doi:10.1016/j.jcis.2017.01.016.

179. Iskandar, F.; Hikmah, U.; Stavila, E.; Aimon, A. H. Microwave-assisted reduction method under nitrogen atmosphere for synthesis and electrical conductivity improvement of reduced graphene oxide (rGO). RSC Advances 2017, 7(83), 52391–52397. doi:10.1039/c7ra10013b.

180. Xing, B.; Zhang, C.; Cao, Y.; Huang, G.; Liu, Q.; Zhang, C.; et al. Preparation of synthetic graphite from bituminous coal as anode materials for high performance lithium-ion batteries. Fuel Processing Technology 2018, 172, 162–171. doi:10.1016/j.fuproc.2017.12.018.

181. Manjushree, S. G.; Adarakatti, P. S.; Udayakumar, V.; Almalki, A. S. A. Hexagonal cerium oxide decorated on β-Ni(OH)2 nanosheets stabilized by reduced graphene oxide for effective sensing of H2O2. Carbon Letters 2022, 32(2), 591–604. doi:10.1007/s42823-021-00296-5.

182. Rani, S.; Aggarwal, M.; Kumar, M.; Sharma, S.; Kumar, D. Removal of methylene blue and rhodamine B from water by zirconium oxide/graphene. Water Science 2016, 30(1), 51–60. doi:10.1016/j.wsj.2016.04.001.

183. Verma, S.; Rani, S.; Kumar, S. Tetragonal zirconia quantum dots in silica matrix prepared by a modified sol–gel protocol. Applied Physics A: Materials Science and Processing 2018, 124(5). doi:10.1007/s00339-018-1806-z.

184. Ferrari, A. C. Raman spectroscopy of graphene and graphite: Disorder, electron-phonon coupling, doping and nonadiabatic effects. Solid State Communications 2007, 143(1–2), 47–57. doi:10.1016/j.ssc.2007.03.052.

185. Petnikota, S.; Maseed, H.; Srikanth, V. V. S. S.; Reddy, M. V.; Adams, S.; Srinivasan, M.; et al. Experimental Elucidation of a Graphenothermal Reduction Mechanism of Fe2O3: An Enhanced Anodic Behavior of an Exfoliated Reduced Graphene Oxide/Fe3O4 Composite in Li-Ion Batteries. Journal of Physical Chemistry C 2017, 121(7), 3778–3789. doi:10.1021/acs.jpcc.6b12435.

186. Altin, Y.; Unsal, O. F.; Bedeloglu, A. C. Fabrication and characterization of polyaniline functionalized graphene nanosheets (GNSs)/polydimethylsiloxane (PDMS) nanocomposite films. Polymers and Polymer Composites 2021, 29, S741–S752. doi:10.1177/09673911211023941.

187. Ossonon, B. D.; Bélanger, D. Synthesis and characterization of sulfophenyl-functionalized reduced graphene oxide sheets. RSC Advances 2017, 7(44), 27224–27234. doi:10.1039/c6ra28311j.

188. Aujara, K. M.; Chieng, B. W.; Ibrahim, N. A.; Zainuddin, N.; Ratnam, C. T. Gamma-irradiation induced functionalization of graphene oxide with organosilanes. International Journal of Molecular Sciences 2019, 20(8). doi:10.3390/ijms20081910.

189. Kim, S.-G.; Park, O.-K.; Lee, J. H.; Ku, B.-C. Layer-by-layer assembled graphene oxide films and barrier properties of thermally reduced graphene oxide membranes. Carbon letters 2013, 14(4), 247–250. doi:10.5714/cl.2013.14.4.247.

190. Tas, M.; Altin, Y.; Bedeloglu, A. Graphene and graphene oxide-coated polyamide monofilament yarns for fiber-shaped flexible electrodes. The Journal of The Textile Institute 2019, 110(1), 67–73. doi:10.1080/00405000.2018.1460039.

191. Cui, J.; Shan, W.; Xu, J.; Qiu, H.; Li, J.; Yang, J. Effect of silane-bridging on the dispersion of polyetheramine-functionalized graphene oxide in waterborne epoxy composites. Composites Science and Technology 2020, 200. doi:10.1016/j.compscitech.2020.108438.

192. Du, X. Q.; Liu, Y. W.; Chen, Y. Enhancing the corrosion resistance of aluminum by superhydrophobic silane/graphene oxide coating. Applied Physics A: Materials Science and Processing 2021, 127(8). doi:10.1007/s00339-021-04730-3.

193. Serodre, T.; Oliveira, N. A. P.; Miquita, D. R.; Ferreira, M. P.; Santos, A. P.; Resende, V. G.; et al. Surface silanization of graphene oxide under mild reaction conditions. Journal of the Brazilian Chemical Society 2019, 30(11), 2488–2499. doi:10.21577/0103-5053.20190167.

194. Sherif, G.; Chukov, D. I.; Tcherdyntsev, V. V.; Stepashkin, A. A.; Zadorozhnyy, M. Y.; Shulga, Y. M.; et al. Surface Treatment Effect on the Mechanical and Thermal Behavior of the Glass Fabric Reinforced Polysulfone. Polymers 2024, 16(6). doi:10.3390/polym16060864.

195. Graf, N.; Yegen, E.; Gross, T.; Lippitz, A.; Weigel, W.; Krakert, S.; et al. XPS and NEXAFS studies of aliphatic and aromatic amine species on functionalized surfaces. Surface Science 2009, 603(18), 2849–2860. doi:10.1016/j.susc.2009.07.029.

196. Li, W.; Xue, F.; Li, Q. Modification of bismaleimide resin by using γ-aminopropyl triethoxysilane functionalised graphene oxide. Plastics, Rubber and Composites 2018, 47(5), 187–191. doi:10.1080/14658011.2018.1459354.

197. Bumajdad, A.; Nazeer, A. A.; Al Sagheer, F.; Nahar, S.; Zaki, M. I. Controlled Synthesis of ZrO_2 Nanoparticles with Tailored Size, Morphology and Crystal Phases via Organic/Inorganic Hybrid Films. Scientific Reports 2018, 8(1). doi:10.1038/s41598-018-22088-0.

198. Jeeva, N.; Thirunavukkarasu, K.; Xavier, J. R. Multilayer Functional Polyurethane Nanocomposite Coating Containing Graphene Oxide and Silanized Zirconium Nitride for the Protection of Aluminum Alloy Structures in Aerospace Industries. doi:10.1007/s11665-02.

199. Bouibed, A.; Doufnoune, R. Synthesis and characterization of hybrid materials based on graphene oxide and silica nanoparticles and their effect on the corrosion protection properties of epoxy resin coatings. Journal of Adhesion Science and Technology 2019, 33(8), 834–860. doi:10.1080/01694243.2019.1571660.

200. Mudila, H.; Rana, S.; Zaidi, M. G. H. Electrochemical performance of zirconia/graphene oxide nanocomposites cathode designed for high power density supercapacitor. Journal of Analytical Science and Technology 2016, 7(1). doi:10.1186/s40543-016-0084-7.

201. Xu, Z.; Zhang, J.; Shan, M.; Li, Y.; Li, B.; Niu, J.; et al. Organosilane-functionalized graphene oxide for enhanced antifouling and mechanical properties of polyvinylidene fluoride ultrafiltration membranes. Journal of Membrane Science 2014, 458, 1–13. doi:10.1016/j.memsci.2014.01.050.

202. Male, K. B.; Lam, E.; Montes, J.; Luong, J. H. T. Noninvasive cell-based impedance spectroscopy for real-time probing inhibitory effects of graphene derivatives. ACS Applied Materials and Interfaces 2012, 4(7), 3643–3649. doi:10.1021/am301060z.

203. Luo, X.; Wang, C.; Wang, L.; Deng, F.; Luo, S.; Tu, X.; et al. Nanocomposites of graphene oxide-hydrated zirconium oxide for simultaneous removal of As(III) and As(V) from water. Chemical Engineering Journal 2013, 220, 98–106. doi:10.1016/j.cej.2013.01.017.

204. Lee, J. H.; Kim, S. H. Fabrication of silane-grafted graphene oxide and its effect on the structural, thermal, mechanical, and hysteretic behavior of polyurethane. Scientific Reports 2020, 10(1). doi:10.1038/s41598-020-76153-8.

205. Heikkila, P.; Harlin, A. Electrospinning of polyacrylonitrile (PAN) solution: Effect of conductive additive and filler on the process. Express Polymer Letters 2009, 3(7), 437–445. doi:10.3144/expresspolymlett.2009.53.

206. Qin, X.; Yang, E.; Li, N.; Wang, S. Effect of different salts on electrospinning of polyacrylonitrile (PAN) polymer solution. Journal of Applied Polymer Science 2007, 103(6), 3865–3870. doi:10.1002/app.25498.

207. Lina, W.; Huiqing, L.; Wentao, L.; Dingding, Z. The effect of nano-zirconia on the morphology and mechanical properties of PVDF/PAN membrane as separators in super capacitors. International Journal of Nanomanufacturing 2019, 15(1/2), 216. doi:10.1504/IJNM.2019.097258.

208. Li, Z.; Wang, C. Effects of Working Parameters on Electrospinning; 2013, 15–28. doi:10.1007/978-3-642-36427-3_2.

209. Kizildag, N.; Ucar, N. Investigation of the properties of PAN/f-MWCNTs/AgNPs composite nanofibers. Journal of Industrial Textiles 2017, 47(2), 149–172. doi:10.1177/1528083716632807.

210. Li, J.; Su, S.; Zhou, L.; Kundrát, V.; Abbot, A. M.; Mushtaq, F.; et al. Carbon nanowalls grown by microwave plasma enhanced chemical vapor deposition during the carbonization of polyacrylonitrile fibers. Journal of Applied Physics 2013, 113(2). doi:10.1063/1.4774218.

211. Liu, R.; Zhou, C.; Wang, Y.; Wang, H.; Li, N. In-situ grown SiO2 on amino-silane modified polyacrylonitrile nanofibrous membranes and its waterproof-breathable and light-shielding properties. Applied Surface Science 2024, 642. doi:10.1016/j.apsusc.2023.158536.

212. Zhang, Y. ; Zhu, B.; Cai, X.; Yuan, X.; Zhao, S.; Yu, J.; et al. Rapid In Situ Polymerization of Polyacrylonitrile/Graphene Oxide Nanocomposites as Precursors for High-Strength Carbon Nanofibers. ACS Applied Materials & Interfaces 2021, 13(14), 16846–16858. doi:10.1021/acsami.1c02643.

213. Hinrichsen, G. Structural changes of drawn polyacrylonitrile during annealing. Journal of Polymer Science Part C: Polymer Symposia 1972, 38(1), 303–314. doi:10.1002/polc.5070380123.

214. Andrady, A. L. Science and Technology of Polymer Nanofibers; Wiley, 2008. doi:10.1002/9780470229842.

215. Samimi-Sohrforozani, E.; Azimi, S.; Abolhasani, A.; Malekian, S.; Arbab, S.; Zendehdel, M.; et al. Development of Porous Polyacrylonitrile Composite Fibers: New Precursor Fibers with High Thermal Stability. Electronic Materials 2021, 2(4), 454–465. doi:10.3390/electronicmat2040031.

216. Shoubak, W. M.; Hassan, A.; Mahrous, S.; Hassen, A. Controlling the physical properties of polyacrylonitrile by strontium hexaferrite nanoparticles. Polymer Bulletin 2024, 81(1), 697–718. doi:10.1007/s00289-023-04736-2.

217. Park, O.-K.; Lee, S.; Joh, H.-I.; Kim, J. K.; Kang, P.-H.; Lee, J. H.; et al. Effect of functional groups of carbon nanotubes on the cyclization mechanism of polyacrylonitrile (PAN). Polymer 2012, 53(11), 2168–2174. doi:10.1016/j.polymer.2012.03.031.

218. Kizildag, N.; Ucar, N.; Karacan, I.; Onen, A.; Demirsoy, N. The effect of the dissolution process and the polyaniline content on the properties of polyacrylonitrile–polyaniline composite nanoweb. Journal of Industrial Textiles 2016, 45(6), 1548–1570. doi:10.1177/1528083714564636.

219. Rahaman, M. S. A.; Ismail, A. F.; Mustafa, A. A review of heat treatment on polyacrylonitrile fiber. Polymer Degradation and Stability 2007, 92(8), 1421–1432. doi:10.1016/j.polymdegradstab.2007.03.023.

220. Brandrup, J.; Kirby, J. R.; Peebles, L. H. On the Chromophore of Polyacrylonitrile. III. The Mechanism of Ketone Formation in Polyacrylonitrile. Macromolecules 1968, 1(1), 59–63. doi:10.1021/ma60001a011.

221. Ji, L.; Medford, A. J.; Zhang, X. Electrospun polyacrylonitrile/zinc chloride composite nanofibers and their response to hydrogen sulfide. Polymer 2009, 50(2), 605–612. doi:10.1016/j.polymer.2008.11.016.

222. Wang, K.; Gu, M.; Wang, J.; Qin, C.; Dai, L. Functionalized carbon nanotube/polyacrylonitrile composite nanofibers: fabrication and properties. Polymers for Advanced Technologies 2012, 23(2), 262–271. doi:10.1002/pat.1866.

223. Tang, Y.; Xu, B.; Gao, Y.; Li, Z.; Tan, D.; Li, M.; et al. Ultrastrong-polar polyacrylonitrile organic-inorganic architected nanogenerators with synergistic triboelectric behavior for efficient biomechanical energy harvesting and self-powered sensing. Nano Energy 2022, 103, 107833. doi:10.1016/j.nanoen.2022.107833.

224. Pillai, A. A.; John, J.; Mathew, R. M.; Jose, J.; Zacharia, E. S.; Abraham, R.; et al. Enhanced output performance of graphene oxide based triboelectric nanogenerators via plasmon coupling. Materials Science and Engineering: B 2023, 296, 116637. doi:10.1016/j.mseb.2023.116637.

225. Rani, G. M.; Ghoreishian, S. M.; Ranjith, K. S.; Park, S. H.; Lee, M.; Umapathi, R.; et al. High Roughness Induced Pearl Necklace-Like ZIF-67@PAN Fiber-Based Triboelectric Nanogenerators for Mechanical Energy Harvesting. Advanced Materials Technologies 2023, 8(19). doi:10.1002/admt.202300685.

226. Mohana Rani, G.; Ranjith, K. S.; Ghoreishian, S. M.; Vilian, A. T. E.; Roh, C.; Umapathi, R.; et al. Fabrication of MoS2 Petals-Decorated PAN Fibers-Based Triboelectric Nanogenerator for Energy Harvesting and Smart Study Room Touch Sensor Applications. Advanced Fiber Materials 2024, 6(6), 1825–1838. doi:10.1007/s42765-024-00453-1.

Abstract

In this study, graphene oxide (GO) was synthesized using the modified Hummers method and functionalized with amino silane (AEAPTMS), resulting in silane-graphene oxide (SGO). The surface of SGO was then decorated with zirconium oxide (ZrO_2) nanoparticles, forming SGO-ZrO_2 nanohybrids. All the synthetized materials were subjected to various characterization techniques, including Fourier transform infrared (FTIR) spectroscopy, X-ray diffraction (XRD), Raman spectroscopy, X-ray photoelectron spectroscopy (XPS), Thermogravimetric analysis (TGA), Zeta potential measurement and Scanning electron microscope (SEM). The results confirmed the successful synthesis of the nanohybrids.

These nanohybrids were incorporated into polyacrylonitrile (PAN) to fabricate composite nanofibers for triboelectric nanogenerator (TENG) applications. Characterization of the PAN-SGO-ZrO_2 nanofibers revealed chemical interactions between the components, enhanced crystallinity and improvements in mechanical properties. TENG devices fabricated with these nanofibers exhibited significantly improved output voltage and power density compared to neat PAN-based devices. This work highlights the potential of combining surface functionalization with electrospun nanofibers for the development of high-performance energy harvesting materials, offering a pathway for scalable, efficient energy harvesting solutions and expanding their application in diverse energy harvesting systems.

Keywords : Graphene oxide, Zirconium oxide, Nanohybrids, Polyacrylonitrile nanofibers, TENGs.

Résumé

Dans cette étude, l'oxyde de graphène (GO) a été synthétisé en utilisant la méthode de Hummers modifiée et fonctionnalisé avec du silane aminé (AEAPTMS), résultant en oxyde de graphène silane (SGO). La surface du SGO a ensuite été décorée avec des nanoparticules d'oxyde de zirconium (ZrO_2), formant des nanohybrides SGO-ZrO_2. Tous les matériaux synthétisés ont été soumis à diverses techniques de caractérisation, y compris la spectroscopie infrarouge à transformée de Fourier (FTIR), la diffraction des rayons X (XRD), la spectroscopie Raman, la spectroscopie de photoélectrons X (XPS), l'analyse thermogravimétrique (TGA), la mesure du potentiel Zeta et la microscopie électronique à balayage (SEM). Les résultats ont confirmé la synthèse réussie des nanohybrides.

Ces nanohybrides ont été incorporés dans le polyacrylonitrile (PAN) pour fabriquer des composites nanofibres destinés aux applications de générateurs triboélectriques (TENG). La caractérisation des nanofibres PAN-SGO-ZrO_2 a révélé des interactions chimiques entre les composants, une cristallinité élevée et des améliorations des propriétés mécaniques. Les dispositifs TENG fabriqués avec ces nanofibres ont montré un voltage et une densité de puissance considérablement améliorées par rapport aux dispositifs à base de PAN pur. Ce travail met en évidence le potentiel de la combinaison de la fonctionnalisation de surface avec des nanofibres électrofilées pour le développement des matériaux de collecte d'énergie haute performance, offrant une voie vers des solutions de collecte d'énergie efficaces et élargissant leur application dans divers systèmes de collecte d'énergie.

Mots-clés : Oxyde de graphène, Oxyde de zirconium, Nanohybrides, Nanofibres de polyacrylonitrile, TENGs.

ملخص:

في هذه الدراسة، تم تحضير أكسيد الجرافين (GO) باستخدام طريقة همرز المعدّلة، وتم تعديله بالأمينو-سيلان (AEAPTMS) للحصول على أكسيد الجرافين السيلاني .(SGO) بعد ذلك، تم تثبيت جسيمات نانوية من أكسيد الزركونيوم (ZrO_2) على سطح SGO، مما أدى إلى تكوين هجين نانوي من .

SGO- ZrO_2خضعت جميع المواد المحضّرة لعدة تقنيات توصيف، بما في ذلك مطيافية الأشعة تحت الحمراء بتحويل فورييه(FTIR) ، حيود الأشعة السينية (XRD)، مطيافية رامان، مطيافية الإلكترون السيني(XPS) ، التحليل الحراري الوزني(TGA) ، قياس الجهد الكهربي السطحي(Zeta potential) ، والمجهر الإلكتروني الماسح (SEM). أكدت النتائج نجاح تخليق الهجين النانوي .

تم دمج هذه المواد في مصفوفة من بولي أكريلونيتريل (PAN) لإنتاج ألياف نانوية مركبة مخصصة لتطبيقات مولدات النانو الكهروستاتيكية (TENG) . أظهر توصيف الألياف النانوية PAN-SGO-ZrO_2تفاعلات كيميائية بين المكونات، وزيادة في التبلور، وتحسنًا في الخصائص الميكانيكية .كما أظهرت أجهزة TENGالمصنوعة من هذه الألياف النانوية تحسنًا ملحوظًا في جهد الخرج وكثافة الطاقة مقارنةً بالأجهزة المعتمدة على PAN النقي. تسلط هذه الدراسة الضوء على جدوى دمج التعديلات السطحية مع الألياف النانوية المنسوجة كهربائيًا لتطوير مواد فعّالة لحصاد الطاقة، مما يوفر طريقًا واعدًا نحو حلول قابلة للتوسيع في أنظمة حصاد الطاقة.

الكلمات المفتاحية: أكسيد الجرافين، أكسيد الزركونيوم، هجين نانوي، الألياف النانوية من بولي أكريلونيتريل، مولدات الطاقة الكهروستاتيكي